공학박사학위논문

가변운행조건 산업용 모터의 고장 진단을 위한 상전류 물리지식착안 딥러닝 연구

Physics-guided Deep Learning Study for Fault Diagnostics of Industrial Motors Under Variable Operating Conditions Using Stator Current Signals

2022 년 2 월

서울대학교 대학원

기계항공공학부

박 찬 희

가변운행조건 산업용 모터의 고장진단을 위한 상전류 물리지식착안 딥러닝 연구

Physics-guided Deep Learning Study for Fault Diagnostics of Industrial Motors Under Variable Operating Conditions Using Stator Current Signals

지도교수 윤병동

이 논문을 공학박사 학위논문으로 제출함

2021 년 10 월

서울대학교 대학원

기계항공공학부

박찬희

박찬희의 공학박사 학위논문을 인준함

2021 년 12 월

위원장 : 김윤영 (인)

부위원장 : 윤병동 (인)

위원 : 안성훈 (인)

위원 : 김도년 (인)

위원 : 오현석 (인)

Abstract

Physics-guided Deep Learning Study for Fault Diagnostics of Industrial Motors Under Variable Operating Conditions Using Stator Current Signals

Chan Hee Park
Department of Mechanical and Aerospace Engineering
The Graduate School
Seoul National University

Industrial motors are widely used in numerous equipment such as industrial robots, electric vehicles, pumps, air handling units. Although they are produced with high reliability to cover huge usage, the failure of industrial motors because of unexpected stresses can cause harmful accidents and economic losses. Therefore, many studies for motor fault diagnosis have been conducted and used to analyze stator current signals due to its convenience on implementation. Recently, motor fault diagnosis needs to be robust to variable operating conditions as the motion of practical settings has become complicated. However, the conventional fault diagnosis methods have challenges: 1) significant amount of parameter settings, 2) limited fault identification,

3) inconsistent severity estimation. To address these challenges, three research thrusts are proposed in this dissertation.

The first research thrust proposes a fault detection method with enhancing fault-sensitivity by reducing the effects of variable speed and load torque conditions in stator current signals. The proposed method does not require significant amount of diagnostic knowledge and difficult expert knowledge such as motor- or fault-related information. Also, the proposed method was available at a low sampling rate with low time cost, because the entire process is calculated in the time-domain. The second research thrust proposes a health image constructed by fault-related component pairs extracted from instantaneous amplitude and phase of a stator current signal. The instantaneous amplitude and phase of a stator current signal reveal the drive-related and the fault-related component, respectively. The proposed method extracts the current residual pairs by subtracting the drive-related component from the instantaneous amplitude and phase, then, the current residual pairs are scaled and spread into a two-dimensional matrix. The proposed method is a pioneering work that considers the image feature which reflects the fault-induced amplitude and phase modulations in stator current signals simultaneously. Thereby, it has a merit of qualitative fault diagnosis by investigating a degree or shape of spreading in the proposed health image. Moreover, the quantitative fault classification method under variable operating conditions is available with the convolutional neural network which learns the proposed health image as the input. The third research thrust proposes a deep learning-based fault severity estimation method using stator current signals. Using a hierarchical deep learning architecture, the proposed method is constructed to assign a fault diagnosis task to a parent module and severity estimation tasks to child modules, then propagate the latent features in the parent module to the child modules. It leads the severity estimation modules to focus on abstracting the specific properties of a particular fault; thereby, the performance of severity estimation could be improved compared to conventional methods and the other deep learning-based methods.

The three research thrusts can be integrated into a fault diagnosis framework of industrial motors under variable operating conditions using stator current signals, and they are related to each other. The first and second research thrusts are based on the physical behaviors of stator currents in a faulty state. The amplitude modulation in the fault detection method, which the product of the first research thrust focuses on, is connected to the envelope residual of the health image, which is the product of the second research thrust. Also, the severity estimation under variable operating conditions is available by providing the health image of the second research thrust as the input of the deep learning model which was proposed in the third research thrust. Furthermore, the outline of this dissertation can be a physics-guided deep learning study, because the features which were based on the physical behaviors of the stator current signals and the deep learning-based fault diagnosis are associated with each other.

Keywords: Fault diagnosis
Industrial motor
Stator current signal
Variable operating condition

Signal processing

Deep learning

Prognostics and health management

Student Number: 2016-20688

Table of Contents

List of Tables

List of Figures

Nomenclatures

T_{e}	electromagnetic torque
$T_{\mathrm{L}}(t)$	load torque
T_{L0}	constant load torque
$T_{\mathrm{f}}(t)$	fault-induced load torque oscillation
p	number of motor poles
ϕ	flux linkage
$L_d,\ L_q$	inductances of the d- and q-axis
i_d, i_q	stator currents of the d- and q-axis
k	torque constant
$\lambda,\ n$	positive integers
J	inertia of the rotating system
B	friction coefficient
B	airgap flux density
$a(t)$	Acceleration
$\omega_r(t)$	rotating speed
$\omega_{\mathrm{r0}}(t)$	instantaneous average rotor speed
$\omega_{\mathrm{e}}(t)$	power supply speed
$\omega_{\mathrm{re}}(t)$	excitation current speed of the permanent magnet rotor
$\omega_{\mathrm{f}}(t)$,	fault-related frequency
φ_{f}	fault-related phase
μ_0	permeability of air
μ	average of the signal
f_{c}	fault characteristic frequency
f_s	fundamental frequency

f_r	rotating frequency
g	nominal airgap length
φ_s	angle of the minimum airgap position due to the static eccentricity
φ_c	oscillation-related phase
θ	circumference angle
θ_s	rotor angular position in the stator reference frame
θ'	rotor angular position in the rotor reference frame
$\theta_\mathrm{r}(t)$	mechanical rotor angular position
α	modulation index
$\beta_1,\ \beta_2$	coefficients
η	initial phase
ζ	arbitrary odd number
δ_s	normalized degree of static eccentricity
δ_d	normalized degree of dynamic eccentricity
E_R	envelope residual
P_R	phase residual
τ, υ	time variable
F	magnetomotive force
$F_1(t)$	major amplitude of magnetomotive force
$F_\mathrm{s}(\theta_\mathrm{s}, t)$	the stator magnetomotive force
$F_\mathrm{r}(\theta', t)$	the rotor magnetomotive force
$\mathrm{V}(t)$	power supply voltage
R_s	stator resistance
$\Phi(t)$,	flux of a motor
Φ_s	amplitudes of the airgap flux caused by the stator magnetomotive force
Φ_r	amplitudes of the airgap flux caused by the rotor magnetomotive force

$x(t)$	stator current signal
$x_a(t)$	analytic signal of the stator current signal
$\hat{x}(t)$	π/2 phase-shifted of stator current signal (Hilbert transform)
$x_m(t)$	amplitude of the analytic signal of stator current signal
$ENV(t)$	upper signal of $x_m(t)$
D	drive-related components of $ENV(t)$
G	gradient of $ENV(t)$
CR	current residual
$\psi(t)$	instantaneous phase
I	instantaneous amplitude
M	Data length
$\hat{\mathbf{t}}$	latent features
$\mathbf{x}$	input data
C_k	k-th fault mode
S_{C_k}	severity of C_k
$\mathbf{W}$	weight matrices
n_b	number of rotor bars
s	slip

Chapter 1

Introduction

1.1 Motivation

Industrial motors are widely used in numerous industrial applications, such as providing driving power to pumps, air conditioning units, electric vehicles and performing a variety of motions with precision control in robots, CNC machines [1]. Despite the high reliability of industrial motors, they are subjected to unexpected stresses such as in-use damage and environmental conditions; hence, they exhibit one of the highest downtime rates machines [2]. To address this problem, many research efforts have been made to develop fault diagnosis methods to infer their health state by analyzing the data from current, vibration, sound, voltage, temperature and so on [3]. Among several signals that have been used for fault diagnosis, the stator current signal is the most generally analyzed signal due to its ease of implementation [4]. Therefore, many fault diagnosis methods based on motor current signature analysis have been employed to high-risk industrial motors and prevented harmful accidents and economic losses.

However, previous fault diagnosis methods have been mainly developed under constant speed conditions [5], [6]; hence, the practical employment of the methods has become difficult in modern industrial applications because many of them work in variable speed and load torque conditions [7]. To this end, it is necessary to develop the fault diagnosis method which is applicable to transient current signals. Despite many of relevant previous studies, there are still several challenges for motor fault diagnostics under variable operating conditions using stator current signal. First, the significant amount of parameter settings are required. Several previous techniques could be conducted only if the motor design parameter is known or the fault-sensitive range is properly decided. Second, fault identification of the previous methods could be limited. For example, the analogy on the conventional features between eccentricity and several mechanical faults have been revealed [8]–[10]. Third, fault severity estimation of the previous methods has shown inconsistency. The studies on severity estimation is crucial in that it can be extended to fault prediction by estimating the growth of fault severity [11]. Most previous studies have analyzed the trend of the feature according to fault severity, however, the behavior of feature has been inconsistent with the fault severity .

Thus, this doctoral dissertation aims at developing a fault diagnosis framework for industrial motors under variable operating conditions, through the deep learning study combined with the physical information of stator current signals. Considering the physical information of the stator current signals, the drive-related component is suppressed and the fault-related component is highlighted with minimal parameters; hence a physics-informed feature can properly indicate a fault under variable operating conditions. Also, the physics-informed feature is combined to the deep learning-based fault diagnosis. Recently deep learning-based fault diagnosis has shown outstanding performance. Although only a few studies have been conducted using stator current signals, the deep learning approach can be a suitable solution to overcome the limited fault identification and inconsistency on severity estimation. Because deep learning-based fault diagnosis has merit in autonomous feature extraction by capturing the underlying relationship between the input data and the health state and has a form of classification and regression.

1.2 Research Scope and Overview

This doctoral dissertation aims at three essential studies for fault diagnosis of industrial motors under variable operating conditions: (1) Research Thrust 1 - fault detection with minimal parameter settings; (2) Research Thrust 2 - fault diagnosis with physics-informed health image feature under variable operating conditions; and (3) Research Thrust 3 - fault severity estimation with a feature-inherited hierarchical deep learning architecture.

Research Thrust 1: Fault detection with minimal parameter settings

Research thrust 1 proposes a drive-tolerant current residual variance (DTCRV), for fault detection of industrial motors under variable speed and load torque conditions. This new approach requires no domain knowledge and is applicable under varying speed and load torque conditions. In the proposed method, first, the envelope of the current signal is calculated to extract its modulation. Second, the drive-related signal, which greatly varies based on speed and load torque conditions, is extracted from the enveloped current signal. Third, the drive-tolerant current residual (DTCR) is calculated; the DTCR is defined as the subtraction of the drive-related signal from the enveloped current signal. Finally, the new health feature is calculated as the variance of the DTCR. To demonstrate the proposed method, the representative case study is presented that examines surface mounted permanent magnet synchronous motors (PMSMs) which were operated under several operating conditions (i.e., different speed profiles and load torque levels)

Research Thrust 2: Fault diagnosis with physics-informed health image feature under variable operating conditions

Research thrust 2 proposes an instantaneous current residual map (ICRM) for fault diagnosis of industrial motors. Inspired by the idea that phase and amplitude modulations in a motor stator current signal provide a direct indication of a faulty state of a PMSM, the overall procedure for constructing ICRM includes two key steps: 1) to calculate the phase and envelop residuals and 2) to spread the scaled current residual pairs into a 2D matrix. A type of faults can be figured out by analyzing a degree or shape of spreading of the scaled current residual pairs in ICRM. Since the current residuals highlight fault-induced irregularities, ICRM is robust to variable operating conditions in practical settings. To demonstrate the effectiveness of ICRM, the experimental validation was conducted with PMSM, operated under variable-speed and different load torque conditions.

Research Thrust 3: Fault severity estimation with a feature-inherited hierarchical deep learning architecture

Research thrust 3 proposes a new deep learning method, specifically, feature inherited hierarchical convolutional neural network (FI-HCNN) for motor fault severity estimation. FI-HCNN consists of a fault diagnosis part and a severity estimation part, arranged hierarchically. The proposed FI-HCNN has the special inherited structure between the hierarchy; the severity estimation part utilizes the latent features to exploit the fault-related representations in the fault diagnosis task. FI-HCNN can improve the accuracy of the fault severity estimation because the level-specific abstraction is supported by the latent features. The proposed method is confirmed its performance with two experimental studies.

1.3 Dissertation Layout

This doctoral dissertation is organized as follows. Chapter 2 reviews the literature regarding motor fault diagnostics. Chapter 3 describes the data used for validation of each proposed research thrust. Chapter 4 proposes a drive-tolerant current residual variance (DTCRV) for fault detection (Research Thrust 1). Chapter 5 presents an instantaneous current residual map (ICRM) for fault diagnosis (Research Thrust 2). Chapter 6 proposes a feature-inherited hierarchical convolutional neural network

(FI-HCNN) for fault severity estimation (Research Thrust 3). Then, Chapter 7 summarizes the dissertation with its contributions and suggested future research.

Chapter 2

Literature Review

This chapter intends to provide previous studies about fault diagnosis methods for motors using the current signal. First, the fault diagnosis methods for the motors under stationary condition are reviewed. Then, the challenges for the previous methods to be applied in nonstationary conditions are presented. Next, fault diagnosis methods for the motors under non-stationary conditions are reviewed. Also, the fault diagnosis methods for motors based on deep learning are investigated. Finally, the limitations of the previous studies are discussed, and I explain how each research thrust is presented in the following sections.

2.1 Fault Diagnostics of a Motor Under Stationary Conditions

There are lots of previous studies to diagnose motor faults under stationary conditions using stator current signals; they can be largely categorized into physics-based and signal based methods. Physics-based motor fault diagnosis can be explained by sub-categorizing into three approaches; 1) spectral analysis, 2) modeling, and 3) Park's vector approaches. Firstly, spectral analysis-based approach investigates the behavior of the spectral features that identify the particular fault using motor-specific parameters [12]–[15]. Further, the stator current spectrum was analyzed to estimate the severity of unbalance, eccentricity, and bearing faults [11]. Secondly, modeling-based approach has been widely used for detecting inter-turn short fault. Many fault indices have been developed with the basis of the electrical model of the faulty winding [16], [17]. In case of the mechanical faults (e.g. eccentricity, gearbox fault, bearing faults, misalignment and unbalance), the torque equation with the mechanical fault is coupled to the electromagnetic torque which is the output torque produced by the interaction between the magnetic field and the stator current in a motor. For eccentricity, which indicates the non-uniform airgap, the stator current model is revealed to have amplitude modulation from the permeance that is inversely related to the airgap length. Furthermore, the amplitude modulation also occurs in the case of several mechanical faults (e.g. misalignment, unbalance, bearing faults, and gearbox faults) because they induce the non-uniform airgap. In addition, the effect of the gearbox fault on the stator current signal of induction motor [18], [19] and permanent magnet synchronous motor [20] were modeled; and derived the fault signatures. Also, the stator current models for detecting bearing damage [21] and unbalance [22] have been derived for fault detection. These studies have derived that the phase modulation is revealed in the stator current by the load torque with mechanical faulty terms. Thirdly, Park's vector approach has been widely applied to motor fault diagnosis. Park's vector was originally developed for the ease on motor control by transforming the three-phase stator current into two axis orthogonal vectors (i.e. d-axis, q-axis). When the vector of the two axes is drawn on the plane, the state of the motor can be observable by investigating the irregularity of the orbit. The aforementioned physics-based methods can be applied to generic motor systems; however, real-world applications are limited because specific motor expertise – which is not easily known – is necessary. Moreover, some fault features, which target different fault modes, have been shown to overlap. For example, the similarity in spectral features has been revealed between eccentricity and the other mechanical faults such as bearing inner race fault [10] and a broken rotor bar [8], [9]. These overlaps make it difficult for the physics-based fault diagnosis method to work properly.

On the other hand, the signal-based method can offer the improved performance for fault diagnosis using only little prior knowledge like metrics for feature extraction, but without motor parameters. Many studies have made an effort to extract fault-sensitive features using signal processing techniques such as wavelet decomposition [23], discrete wavelet transform [24], and empirical mode decomposition [25]. Several machine learning techniques have been applied to extract the fault-sensitive features, for example, principle component analysis (PCA) [26]–[28], genetic algorithm [29], and support vector machine (SVM) [30]. These methods do not require motor- or fault-specific expertise; however, they do require significant level of diagnostic knowledge to devise features which are labor-intensive.

Despite continuous development of fault diagnostics using stator current signal under stationary condition, the practical application is difficult in modern industrial systems where variable operating conditions (i.e., various speed profiles and load torques) are prevalent. The signal deformation that results from these variable drive-related conditions makes it difficult to identify the fault-related fluctuations because the drive-related current signals are dominant in the variable operating condition. Figure representatively describes the difference of the result when the spectral analysis based, and Park's vector approach are applied to the stator current signal under constant speed and variable speed conditions respectively.

2.2 Fault Diagnosis of a Motor Under Variable Operating Conditions

This section consists of the review of fault diagnosis methods for motors to handle variable operating conditions. As mentioned in 2.1., there are several limitations to apply the conventional methods to variable operating conditions. To address this limitations, the fault diagnosis methods have been developed by examining transient current signals. In this section, 1) time-frequency analysis-based, 2) signal-based, and 3) image-based approaches are reviewed.

2.2.1 Time-frequency Analysis (TFA)-based Approach

Time-frequency analysis (TFA) represents signals in the time-frequency domain; therefore, the spectral properties of signals can be shown in time-series. Most previous research using TFA has investigated the trend of coefficients according to the particular fault frequency[31]–[34]. In [35]–[38], the energy around fault characteristic frequency was computed in Wigner-Ville distribution (WD), and its behavior on speed and load variations were investigated. Similarly, the harmonic order tracking method was developed to identify rotor faults using Garbor transformed current signals [39], and the gear fault frequency was tracked in the space vector modulus of the current using the improved polynomial chirplet transform (PCT) [40]. Figure 2-1 shows the time-frequency domain of stator current signal using pseudo-WD that often replaces WD to compensate for interference terms in practical applications [41]. For example, the energy of the modulated coefficients from those of principal can be investigated according to the fault characteristic frequency. The TFA-based approaches require several motor-specific information and the speed profile to compute the time-varying characteristic features.

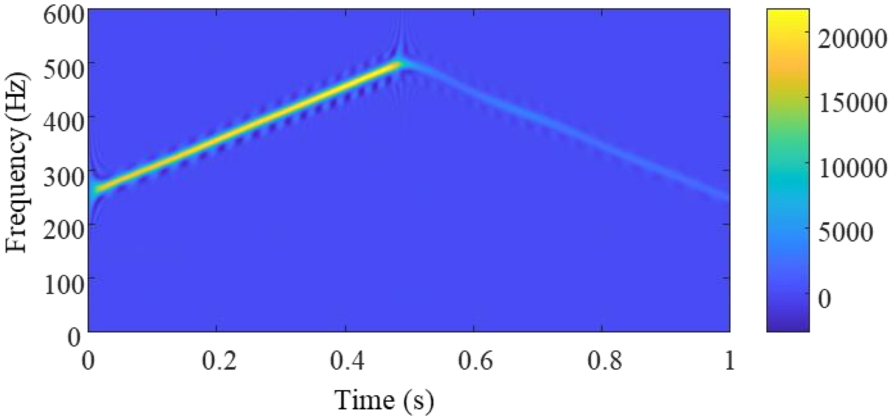

Figure 2-1 Example of time-frequency analysis-based approach using pseudo-Wigner Ville distribution

2.2.2 Signal-based Approach

The signal-based approach can be one of the ways to avoid the challenge of TFA-based method; it catches up the fault-sensitive signature by decomposing the signals into subdivided components. The discrete wavelet transform (DWT), which decomposes a signal using high- and low-pass filters with particular mother wavelets, was applied to detect a motor fault by finding abnormally fluctuating wavelet coefficients [42], [43]. Figure 2-2 shows the procedure of signal decomposition using DWT with schematic. If $d3$ in Figure is confirmed to be fault-sensitive, the fault feature is designed using the $d3$ such as the energy. In [23], the linear combination of statistical features, defined by the detail signals in DWT, was used to observe the dynamic eccentricity of PMSMs. In [44], DWT decomposed the current signal of which the fundamental component was removed by the adaptive filter to detect faults under variable driving conditions. In [24], [45], the energy of the detail signals in DWT that revealed the fault patterns was investigated to detect rotor faults and mixed eccentricity. Also, the intrinsic mode function (IMF) calculated by empirical mode decomposition (EMD) was investigated to extract the information related to faults in the current signals. Several fault indicators were developed to detect faults under non-stationary condition, such as the degree of fluctuations of IMFs [25], [46], the energy of IMFs [47], and the instantaneous amplitude of IMFs computed by the Hilbert-Huang transform (HHT) [48], [49]. The signal-based approaches does not require expertise about motor and fault types, however, demand considerable level of diagnostic knowledge such as the selection of the particular bandwidth or decomposition level that is sensitive to the fault.

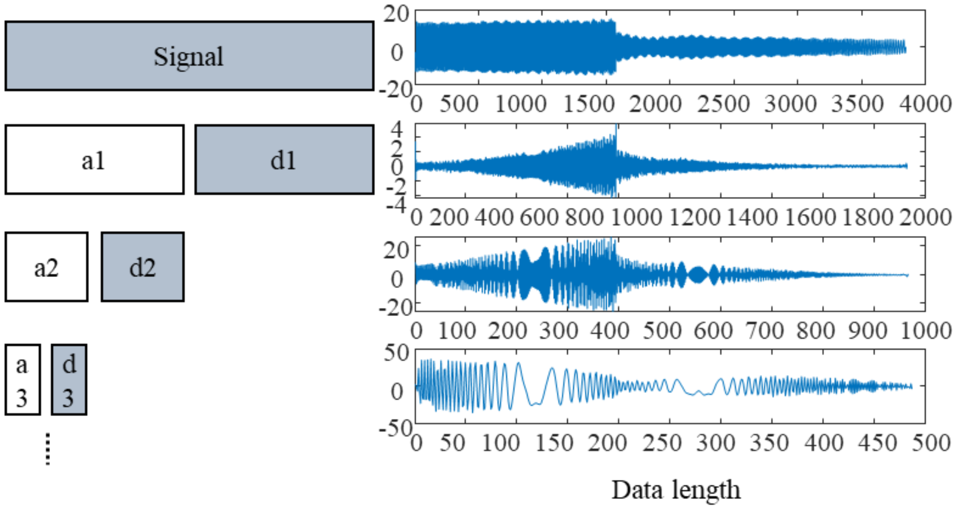

Figure 2-2 Example of signal-based approach using discrete wavelet transform

2.2.3 Image-based Approach

Recently, deep learning based fault diagnosis has shown outstanding performance, where it captures the underlying relationship between the input data and the health state [50], [51]. Especially, a convolutional neural network (CNN) has become the leading model for learning image-data; its advantages of local connectivity and parameter sharing [40] can bring the remarkable performance on good classification results in image-data. To make the best use of CNN for fault diagnosis, numerous studies have sought to convert sensory signals, which are a type of time-series data, to a two-dimensional (2D) input image [53]–[57]. For this purpose, several signal-to-image encoding methods have been introduced, such as Gramian angular field (GAF) [58], [59], Markov transition field (MTF) [60], [61]. Figure 2-3 shows the 2D

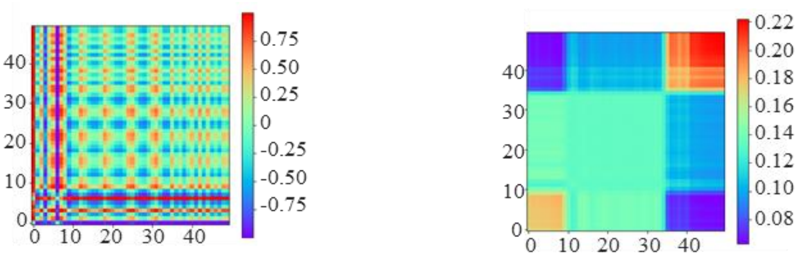

(a) (b)

Figure 2-3 Example of image-based approach using time series signal to image encoding: (a) Gramian angular field (GAF), (b) Markov transition field (MTF)

images that are generated with GAF, MTF respectively. Through these images, the characteristics of the time-series signal, including the interactions between nearby data and the data ordering, can be considered to capture the signature that is spread over time. In [62]–[64], signals were simply stacked to construct a 2D input image based on the time ordering. In [64], each point of signals was allocated to a certain pixel in a 2D input image. Most signal-to-image encoding methods have mainly extracted time-domain features; however, some fault signatures of rotating machines can be more easily recognizable in the frequency-domain, such as harmonic components and peak frequency.

Alternatively, time-frequency representation (TFR) can be used to generate a 2D input image that contains spectral information with time. The attempts to use the 2-dimensional time-frequency coefficients as image feature for fault detection have been conducted in medical applications for human disease detection at the beginning. The electroencephalogram (EEG) signals were analyzed by converting it into TFR image using WD, Gaussian kernel distribution, and modified-B distribution. Then, the texture-based features were extracted from the TFR image with Haralick and local binary pattern. In this regard, the feature extraction is analogous to those of prior studies explained in Section 2.2.1, where fault-related patterns were investigated in the TFR. While the health feature is intensively captured based on considerable efforts with domain knowledge on statistics and signal processing, the deep learning architecture can replace the feature extraction by formulating the relationship between the input data and the given health state. Therefore, a spectrogram using short time Fourier transform (STFT) [65] and a scalogram using wavelet transform (WT) [66]–[68] have been used as 2D input images to a CNN model for fault diagnosis. However, TFR is still at risk of losing fault-related information because signals can be localized in different regions of TFR due to the dependency on parameter settings (e.g. window size, overlap length, and basis function) based on prior knowledge. Further, the resolution of TFR cannot be guaranteed because of Heisenberg's uncertainty principle, thereby affecting the accuracy of fault diagnosis. In addition, a variation in motor stator current signals that is caused by different operating conditions could predominate over that by faults ; but it is difficult for TFR to distinguish them [69], [70].

Advanced conversion methods that consider characteristics of rotating machines, such as omni-directional regeneration (ODR) [71] and symmetrized dot pattern (SDP) [72], have also been employed in conjunction with CNN-based fault diagnosis. Owing to the ability of the ODR technique to produce virtual vibration signals from any arbitrary direction, it can easily detect direction-oriented faults of rotor systems. By depicting changes in the amplitude and frequency of a vibration signal in a polar coordinate system, SDP images can reveal different vibration states.

However, it is worth pointing out that these conversion methods mainly concern image representation of vibration signals; there have been only a few attempts to put the physical meaning of motor stator current signals acquired from PMSMs to a 2D input image for CNN-based fault diagnosis. The revelation of physical meaning of the faults in the deep-learning based fault diagnosis is a still big challenge to be explored.

2.3 Stator Current Model for Fault Diagnosis

To offer the physical foundation of the procedures in the following proposed methods, this section explains the motor stator current model in the perspective of operating conditions and fault-induced components respectively.

2.3.1 The Relation of the Stator Current Signal and Driving Conditions

Through the electromagnetic torque T_e, which is the torque produced in a motor, it is possible to associate the stator current signal with the driving conditions. In the case of a permanent magnet synchronous motor, T_e can be expressed by a function of inductance and stator currents as [73]:

$$T_\mathrm{e} = \frac{3p}{2}[\phi i_q + (L_d - L_q) i_d i_q] \tag{2.1}$$

where p is the number of poles; ϕ is the flux linkage generated by the permanent-magnet poles of the rotor; and L_d, L_q are the stator currents and inductances of the d- and q-axis, respectively. i_d and i_q are the values converted from the three-phase stator currents using *dq*-transform for pursuing convenience in control. In the case of field-oriented control systems, which are generally used for servo-systems, i_q is interpreted to be proportional to T_e, because the flux of the *d*-axis is controlled to be continuously aligned with i_d [74]. Considering the surface-mounted PMSM, which has the same L_d and L_q value, T_e and the electromechanical torque equation can be expressed as:

$$T_\mathrm{e}(t) = ki_q(t) = J\frac{d}{dt}\omega_r(t) + B\omega_r(t) + T_\mathrm{L}(t) \tag{2.2}$$

where *k* is the torque constant, *J* is the inertia of the rotating system, *B* is the friction coefficient, $\omega_r(t)$ is the rotating speed, and $T_\mathrm{L}(t)$ is the load torque. From (2.2), the driving conditions (i.e., load component, velocity, and acceleration) are confirmed to affect not only $T_\mathrm{e}(t)$, but also $i_q(t)$, which is the converted value of the stator current signals.

2.3.2 Fault Signatures in a Stator Current Signal

Many studies have derived a stator current model considering many types of faults; the derivation can be summarized in two approaches that which physical term is changed due to the fault.

2.3.2.1. Fault Model Derived from Airgap

As mentioned in Section 2.1, the non-uniform airgap affects the permeance, which is inversely related to the airgap length as [41]:

$$\Lambda(t,\theta) = \frac{\mu_0}{g}(1+\delta_s\cos(\theta-\varphi_s)+\delta_d\cos(\omega_r t-\theta)) \tag{2.3}$$

where, μ_0 is the permeability of air, g is the nominal airgap length, φ_s is the angle of the minimum airgap position due to the static eccentricity, and θ is the circumference angle. δ_s and δ_d are the normalized degree of static and dynamic eccentricity [75], [76]. Considering the fundamental harmonic term, the magnetomotive force (MMF) can be approximated as:

$$\mathrm{F}(t,\theta) = F_1(t)\cos(\omega_e t - p\theta) \tag{2.4}$$

where, $F_1(t)$ denotes the major amplitude of MMF, and ω_e is the electric rotating speed. Then, the airgap flux density B is defined as the product of MMF and the permeance as:

$$\begin{aligned} \mathrm{B}(t,\theta) &= \mathrm{F}(t,\theta)\cdot\Lambda(t,\theta) \\ &= K_B(t)[B_c + B_m\cos(\omega_r t-\theta)]\cos(\omega_e t - p\theta) \end{aligned} \tag{2.5}$$

$$\mathrm{V}(t) = R\mathrm{I}(t) + \frac{d}{dt}\Phi(t) \tag{2.6}$$

where, $K_B(t)$ is $F_1(t)\mu_0/g$, B_c is $1+\delta_s\cos(\theta-\varphi_s)$, B_m is δ_d, R_s is stator resistance, and $\mathrm{V}(t)$ is power supply voltage. As B is the derivative of the flux $\Phi(t)$, the stator voltage equation (as in (2.6)) implies that the major component of the stator current can be expressed as:

$$\begin{aligned} \mathrm{I}(t) &= K_I(t)[I_c + I_m\cos(\omega_r t-\varphi_m)]\cos(\omega t-\nu) \\ &= I_1(t)\cos(\omega t-\nu) + \alpha I_1(t)\cos((\omega\pm\omega_r)t-\varphi) \end{aligned} \tag{2.7}$$

where, $K_I(t)$, I_c, and I_m are the corresponding terms of $K_B(t)$, B_c, and B_m, respectively. $I_1(t)$, φ, φ_m and ν are the coefficients and phases of the stator current's major components, including the terms related to the static and dynamic eccentricity, and

α is the modulation index. Based on (2.7), the faults can be confirmed by investigating the amplitude modulation in the stator current signals. Also, the electrical faults represented by stator turn shorts affect the stator current by showing odd multiples of the supply frequency's third harmonics [77]–[79], or amplitude modulation of the rotating frequency [80], [81]. Therefore, the amplitude modulation of the stator current can be observed in both the mechanical and electrical fault states of a rotating system.

2.3.2.2. Fault Model Derived from Torque Oscillation

The load torque oscillation can also cause the modulation of a stator current signal [22]. When the load torque is described as:

$$\mathrm{T_L}(t) = T_{\mathrm{L0}} + T_{\mathrm{f}} \cos(\omega_{\mathrm{c}} t) \tag{2.8}$$

Where T_{L0} is the constant load torque and T_{f} is the amplitude of the additional oscillation component varying at the characteristic frequency f_{c} ($\omega_c = 2\pi f_c$). Assumed that the effect of friction coefficient is very small and substitute (2.8) to (2.2), the mechanical rotating speed $\omega_r(t)$ can be expressed as:

$$\omega_r(t) = \frac{1}{J}\int_0^t T_{\mathrm{e}}(\tau) - T_{\mathrm{L}}(\tau)\, d\tau = \frac{T_{\mathrm{f}}}{J\omega_{\mathrm{c}}} \cos(\omega_{\mathrm{c}} t + \varphi_{\mathrm{c}}) + \omega_{r0} \tag{2.9}$$

where ω_{r0} is the average constant component of speed; φ_c are the oscillation-related phase. Then, the mechanical rotor position can be derived as:

$$\theta_{\mathrm{r}}(t)=\frac{T_{\mathrm{f}}}{J}\sin(\omega_{\mathrm{c}}t+\varphi_{\mathrm{c}})+\omega_{r0}t \tag{2.10}$$

According to the reference frame, the rotor angular positions have the relationship as:

$$\theta_{\mathrm{s}}=\theta'+\theta_r(t) \tag{2.11}$$

where θ_{s} is the rotor angular position in the stator reference frame and θ' is the rotor angular position in the rotor reference frame. Considering the total MMF can be expressed with a combination of the stator MMF $F_{\mathrm{s}}(\theta_{\mathrm{s}}, t)$ and the rotor MMF $F_{\mathrm{r}}(\theta', t)$ as:

$$F(\theta,t)=F_{\mathrm{s}}(\theta_{\mathrm{s}},t)+F_{\mathrm{r}}(\theta',t) \tag{2.12}$$

Substitute (2.11) to (2.12), it can be rewritten as:

$$F(\theta,t)=F_s\sin(p\theta_s-\omega t)+F_r\cos(p\theta_s-p\theta_r-\omega t) \tag{2.13}$$

Using the relationship of $\omega=p\omega_{r0}t$ and (2.10), the rotor MMF can be rewritten as:

$$F_r(\theta,t)=F_r\cos(p\theta_s-\omega t-\frac{pT_c}{J\omega_c^2}\sin(\omega_c t+\varphi_{\mathrm{c}})) \tag{2.14}$$

Based on (2.5) and the airgap permeance is supposed constant for simplicity, the airgap flux density can be described as:

$$\mathrm{B}(t,\theta)=B_s\sin(p\theta_s-\omega t)+B_r\sin(p\theta_s-\omega t-\frac{pT_c}{J\omega_c^2}\sin(\omega_c t+\varphi_{\mathrm{c}})) \tag{2.15}$$

Similar to the derivation of (2.7) and based on (2.6), the stator current signal can be estimated to have the time-derivative terms of the flux which is the integral of the airgap flux density with θ_s. As a consequence, the stator current signal can be described as:

$$\mathrm{I}(t) = I_s \sin(\omega_s t + \varphi_s) + I_r \sin(\omega_s t + \frac{pT_c}{J\omega_c^2} \sin(\omega_c t + \varphi_c)) \tag{2.16}$$

Based on (2.16), the torque oscillations can leads the phase modulation of stator current signals; therefore, mechanical faults in a rotating system can be confirmed by investigating the phase modulation in the stator current signals.

2.4 Summary and Discussion

Fault detection by reducing effects of variable speed and load torque conditions with minimal parameter settings

There are several fault diagnosis methods for variable-speed conditions as mentioned in Section 2.2; however, significant amount of parameter setting is required. For physics-based method, the fault, and motor specific information is necessary to calculate the feature. For signal-based method, diagnostic knowledge to process the stator current signal is necessary. Therefore, in this dissertation, a novel method to detect motor faults under variable speed and load torque conditions with minimal parameter setting is proposed. The proposed method requires neither fault-, motor-specific information nor diagnostic knowledge. By subtracting the drive-related signal from the enveloped stator current signal in the time-domain, the time-cost also decreases.

Fault diagnosis with physics-informed health image feature under various operating conditions

As mentioned in Section 2.3, the amplitude and phase modulation of the stator current signal was confirmed to have fault-related components; however, to the best of the authors' knowledge, there is no health feature that considers fault-induced phase as well as amplitude modulations in a motor stator current signal measured from a PMSM under variable operating conditions. To fill this research gap, in this dissertation I newly proposes a physics-informed health image that can be used as the 2D input to a CNN model for accurate fault diagnosis.

Fault severity estimation with a deep learning-based method that the latent features are propagated

Severity estimation is essential for fault prediction; however, there exist only a relatively small number of studies that using stator current signals. For example, Ince et al. [82], [83] used a 1-D CNN architecture to detect a motor bearing cage fault. In [84], SincNet was adopted to classify multiple faults, including broken rotor bars and bearing faults. Therefore, in this dissertation, a new DL-based severity estimation method is proposed. Considering a hierarchical network for fault diagnosis, the severity estimation is fine level which followed by fault diagnosis; it intends to enhance the performance of severity estimation through a novel connecting architecture; the latent features in the fault diagnosis module are used as inputs to the corresponding severity estimation modules. Moreover, the proposed method considers the continuity of fault severity with regression.

Chapter 3

Data Description

This chapter describes the dataset which were used to validate the proposed method. First, the experiment setup to measure the stator current signals is described. Then, the dataset which are acquired from the testbed are presented specifically.

Figure 3-1 shows the overall configuration of the testbed; the target motor is highlighted, which is surface-mounted PMSM embedded in 4th axis of a cooperative robot. The target motor was position-controlled using an incremental encoder, of which the resolution was 4000 pulses per revolution. A hysteresis brake (Magtrol, BHB-3BA) was connected to the motor shaft via couplings; a torque meter (Unipulse, UTM-II) was installed between two couplings to measure torque and speed. The three-phase stator current signals were measured by current probes (Tektroniks, A622), which were mounted between the servo drive and the motor. All signals were collected with a sampling rate of 12,800 Sa/s using an NI-system (C-RIO9066).

Two fault modes were emulated to investigate the proposed methods. First, for the electrical fault, a stator inter-turn short was injected by coiling the uncovered windings in the production state. Figure 3-2 shows a faulty stator in which a portion of the windings were chemically uncovered. Two motors with different fault levels, where the degrees of uncovered windings were different, were used in the experiment. Table 3-1 describes the measured impedance (resistance, inductance) of the two stator inter-turn short motors and normal motors; the uncovered windings were coiled up only in the a-phase.

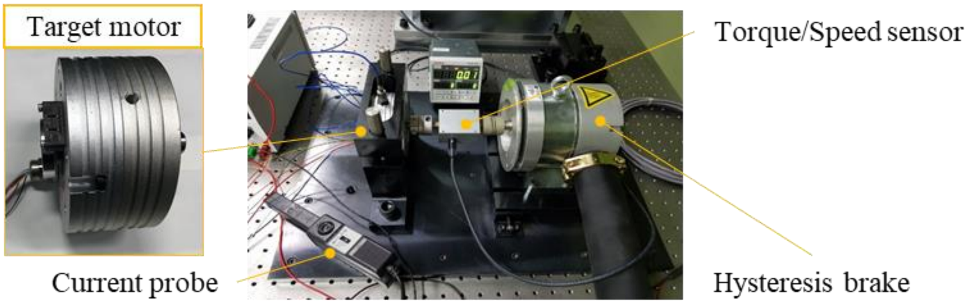

Figure 3-1 Overall setup of the testbed

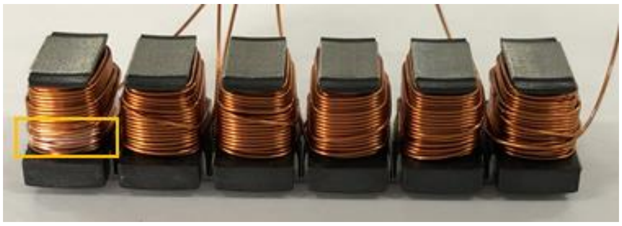

Figure 3-2 Inter-turn short windings

Table 3-1 The impedance of the stator inter-turn short motors used in experiment

Phase			Nor		SIS1		SIS2	
Resistance (Ω)		a	0.37		0.36		0.35	
		b	0.37		0.37		0.38	
		c	0.37		0.37		0.38	
Inductance (mH)			L	Q	L	Q	L	Q
	250 Hz	a	0.33	1.42	0.31	1.30	0.26	1.09
		b	0.33	1.39	0.34	1.42	0.32	1.36
		c	0.32	1.35	0.32	1.37	0.31	1.31
	500 Hz	a	0.33	2.81	0.31	2.36	0.25	1.61
		b	0.33	2.74	0.34	2.79	0.32	2.67
		c	0.32	2.64	0.32	2.68	0.31	2.58

To investigate a mechanical fault, misalignment was emulated by rearranging the vertical height of the motor with reference to [74], [85]–[87], as shown in Figure 3-3. Two fault levels (2mm and 4mm) were used in the experiment. For the variable operating conditions, two speed profiles (named trapezoidal and triangle) with five load torque levels (0 %, 30 %, 50 %, 70%, 100 % of the rated load torque) were examined as shown in Figure 3-4. All the operating conditions that were used in the experiment were summarized in Table 3-2.

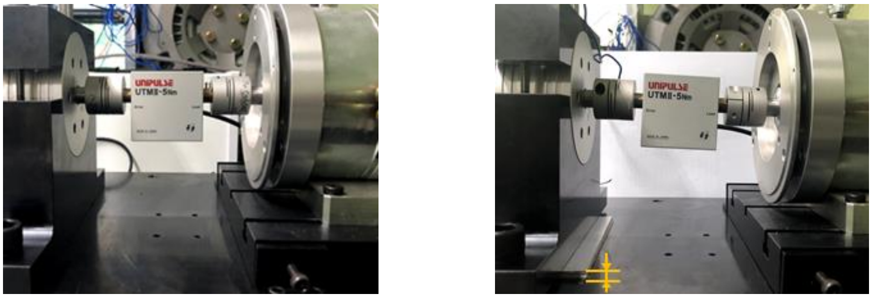

(a) (b)

Figure 3-3 The misalignment set up: (a) Normal and (b) Misalignment

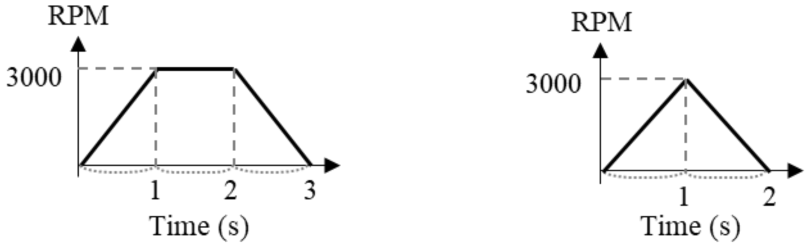

(a) (b)

Figure 3-4 The speed profiles of operating conditions used in experiment: (a) Trapezoidal and (b) Triangle

Table 3-2 The experimental conditions

State	Abbreviation	Fault level	Speed profile	Load torque (%)				
Normal	NOR	0	Trapezoidal Triangle	0	30	50	70	100
Stator inter-turn short	SIS1	1	Trapezoidal Triangle	0	30	50	70	100
	SIS2	2	Trapezoidal Triangle	0	30	50	70	100
Misalignment	MSGN1	1	Trapezoidal Triangle	0	30	50	70	100
	MSGN2	2	Trapezoidal Triangle	0	30	50	70	100

Sections of this chapter have been published or submitted as the following journal articles:

1) **C. H. Park,** J. Lee, H. Kim, C. Suh, M. Youn, Y. Shin, S. H. Ahn, and B. D. Youn, "Drive-Tolerant Current Residual Variance (DTCRV) for Fault Detection of a Permanent Magnet Synchronous Motor Under Operational Speed and Load Torque Conditions." IEEE Access, vol. 9, pp. 49055-49068, 2021

Chapter 4

Fault Detection Under Variable Operating Conditions with Minimal Parameter Settings: Drive-tolerant Current Residual Variance (DTCRV)

The proposed drive-tolerant current residual variance (DTCRV) method is explained in detail in this section. As described in the introduction, the proposed DTCRV method was developed with the aim to detect motor faults under variable operating conditions using only the stator current signal. In this chapter, the conventional fault detection methods under time-varying conditions using stator current signals are reviewed first. Next, the proposed DTCRV method is explained. Then, the proposed method is demonstrated with experiment data.

4.1 Review of Fault Detection Methods Using Stator Current Under Variable Operating Conditions

Although the conventional methods are described in the introduction, this section focuses on the TFA-based approach and signal-based approach for fault diagnosis of electrical and mechanical faults under variable operating conditions in order to compare them with the proposed method.

First, in the TFA-based approach, it has common property in that the modulation of the fault-related frequency is in the current signal. The modulation of the third harmonic of the supply frequency is associated with an electrical fault; the modulations of the torque-fluctuated harmonics are associated with mechanical faults. Lots of researchers have adopted the approach of monitoring the third harmonics for detecting a stator inter-turn short [78], [88]–[90]. For mechanical faults, the characteristic frequencies are associated with the load torque oscillation, and appear as the sidebands of the fundamental frequency f_s [21], [22], [41], [91]. Table 4-1 summarizes the fault characteristic fault frequency f_c in the current spectrum, where f_r is the rotating frequency, and $n = 1,2,3, \ldots$ Although f_c can detect each fault in stationary conditions, f_c cannot be applied to non-stationary conditions directly, due to the time-varying f_r and f_s. Therefore, several studies have conducted time-frequency analysis to track the magnitude of the fault characteristic frequency in the time-frequency domain [92]–[95]. In particular, WD has been widely used to calculate the features in the time-frequency domain [92], [93], and pseudo-WVD (PWD) often replaces WD to compensate for interference terms in practical application [41], [96]. For example, the energy of $3f_s$ is extracted for investigating stator inter-turn short; the energy around $f_s \pm f_r/2$ which are calculated using PWD can investigate the mechanical faults. These TFA-based approaches require several motor-specific information and the speed profile to

Table 4-1 Fault characteristic features in the current spectrum

Fault mode	Fault characteristic frequencies in the current spectrum f_c
Stator inter-turn short	$f_c = 3f_s$
Mechanical faults caused by load torque oscillation (e.g., unbalance, misalignment, eccentricity)	$f_c = f_s \pm nf_r$

compute the time-varying characteristic frequencies.

Further, signal-based approaches (e.g., discrete wavelet transform (DWT), [23], [24], [42], [44], [45], empirical mode decomposition (EMD) [25], [46], [47], Hilbert Hwang transformation (HHT) [48], [49]) have been adopted to readily extract the fault-related components. When DWT was used, the energy of the specific detail signals could be calculated for the health feature [24], [45]. The specific detail signals were selected based on an observation of the fault-pattern. When EMD [25], [46], [47] or HHT [48], [49] was used, the IMFs that reveal the fault-related components were investigated after decomposing the drive-related components in the preceding IMFs. However, the observation of the appropriate decomposed signals containing fault information is difficult for the signal decomposition based approach. In addition, most of the aforementioned studies were validated under only variable-speed profiles. Therefore, the application of these conventional methods for real driving conditions – in which the speed varies under several load torque conditions – is uncertain.

To sum up the aforementioned approaches, they are limited to situations where the fault-related information is pre-assigned, such as fault characteristic frequency over time and the decomposition level that the fault patterns reveal. However, the proposed method does not require any information about the fault or the driving conditions;

instead, it adaptively decreases the effect of speed and load torque conditions based on the physical relations between the torque and current of a motor.

4.2 Proposed DTCRV Method

This section presents the proposed DTCRV method to detect faults under operational speed and load torque conditions. Figure 4-1 offers a flowchart of the proposed method. The details of each step are described in Sections 4.2.1 and 4.2.2, focusing on the principle of the proposed method. In Section 4.2.3, the contribution and advantages of the proposed method are explained with the comparison of the conventional methods.

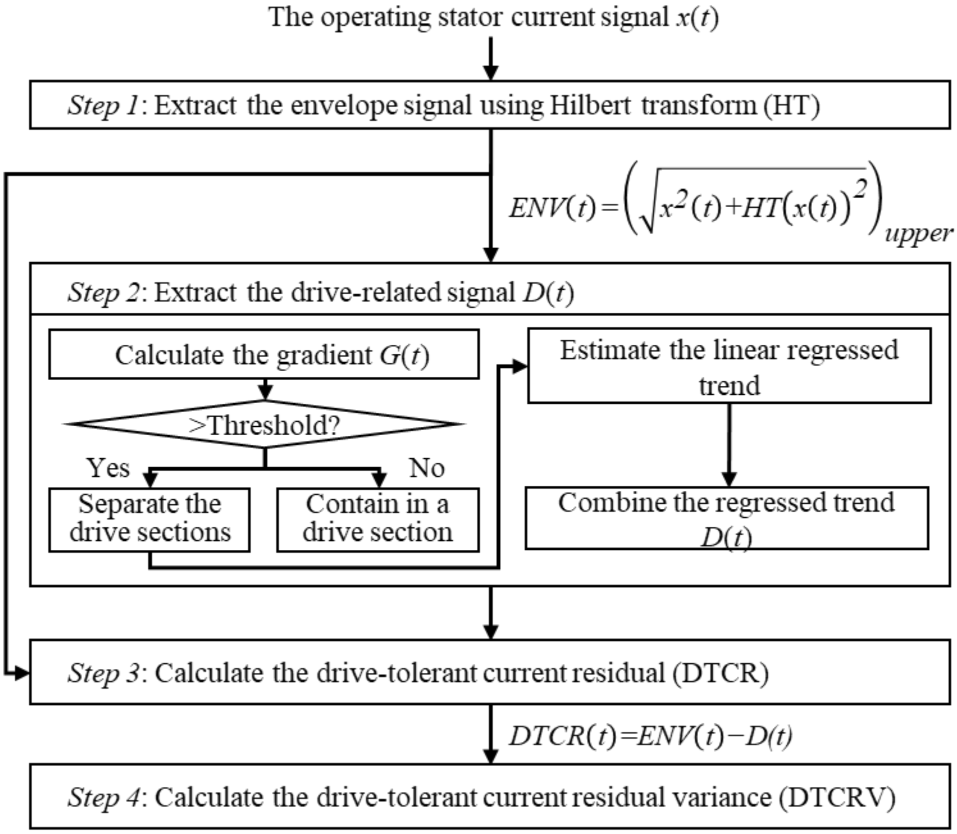

Figure 4-1 A framework of the proposed DTCRV method

4.2.1 Extraction of the Drive-related Signal

Since the raw stator current signal consists of a fundamental driving sinusoidal wave and other harmonics that can be generated by the controller, faults, or other factors, the envelope of the raw stator current signal is firstly extracted. Based on (2.7), the major component of the raw stator current signal can be expressed as:

$$x(t) = I_1(t)\cos(2\pi f_s t) + \alpha I_1(t)\cos(2\pi(f_s \pm f_c)t + \varphi_c) \tag{4.1}$$

where α is the modulation index; f_c and φ_c are the frequency and phase angle of the fault, respectively. Then, the analytic signal of $x(t)$ using HT can be related to the amplitude of the enveloped current signal as:

$$x_a(t) = x(t) + j\hat{x}(t) = x_m(t)e^{j\psi(t)} \tag{4.2}$$

where $x_a(t)$ is the analytic signal of $x(t)$, $\hat{x}(t)$ is the HT result of $x(t)$ that is $\pi/2$ phase-shifted, $x_m(t)$ is the amplitude of $x_a(t)$, and $\psi(t)$ is the instantaneous phase. Based on Section II-B, the information about the fault-related AM is expected to be carried in $x_m(t)$. $x_m(t)$ conserves the magnitudes of $x(t)$, while it reduces the effect of high-frequency noises that are usually induced from a variable frequency drive. In this study, the upper signal of $x_m(t)$, denoted as $ENV(t)$, is used.

Next, the drive-related signal is extracted from $ENV(t)$. In a balanced three-phase system, the magnitude of $x_m(t)$ is proportional to $T_e(t)$; therefore, $ENV(t)$ can be expressed from (2.2) as:

$$ENV(t) \propto i_q(t) \tag{4.3}$$

Based on the fact that $i_q(t)$ is the result of dq-transformation of the three-phase $x(t)$, $i_q(t)$ can be written from (4.1) as:

$$\begin{aligned} i_q(t) &= I_1(t)\cos(2\pi f_s t - \theta_0) + \alpha I_1(t)\cos(2\pi(f_s \pm f_k)t + \varphi_k - \theta_0) \\ &= I_1(t)\cos(\theta_p) + \alpha I_1(t)\cos(\pm 2\pi f_k t + \varphi') \end{aligned} \tag{4.4}$$

where θ_0 is set to $2\pi f_s t+\theta_p$; θ_p is the constant phase angle, and φ' is φ_k-θ_p. Also, the right-hand side of (2.2) can be rewritten to include the torque oscillations and spatial harmonics as:

$$(J\frac{d}{dt}\omega_r(t)+B\omega_r(t)+\mathrm{T}_{\mathrm{L0}})+\sum_{n=1}^{\infty}\mathrm{T}_n(t)\cos(2\pi f_n t+\varphi_n) \tag{4.5}$$

where T_{L0} is the constant load torque, *n* is the positive integers, T_n, f_n, and φ_n are the amplitude, frequency, and phase angle for torque oscillations, respectively. When (4.4) and (4.5) are incorporated into (2.2), the torque-current mechanism can be described as:

$$\begin{aligned} & kI_1(t)\cos(\theta_p)+k\alpha I_1(t)\cos(\pm 2\pi f_k t+\varphi') \\ & =(J\frac{d}{dt}\omega_r(t)+B\omega_r(t)+\mathrm{T}_c)+\sum_{n=1}^{\infty}\mathrm{T}_n(t)\cos(2\pi f_n t+\varphi_n) \end{aligned} \tag{4.6}$$

Sequentially the first term in the left-hand side corresponds to the first term in the right-hand side, which is related to the driving condition. Also, *ENV*(*t*) is proportional to (4.6) based on (4.3) as:

$$ENV(t)\propto(J\frac{d}{dt}\omega_r(t)+B\omega_r(t)+\mathrm{T}_c)+\sum_{n=1}^{\infty}\mathrm{T}_n(t)\cos(2\pi f_n t+\varphi_n) \tag{4.7}$$

The first term in the right-hand side of (4.7) can be matched to the dominant linear trend of *ENV*(*t*) in the case of constant acceleration. Although the motion of manufacturing machines is complicated, the speed profile of a servo motor usually consists of constant acceleration, short or no constant speed, and deceleration.

Figure 4-2 shows the procedure of extracting the dominant trend from *ENV*(*t*) in the driving condition, which consists of constant acceleration, constant speed, and constant deceleration. The dominant trend of *ENV*(*t*) changes linearly as the speed changes linearly in a uniform acceleration region. When the driving condition changes from acceleration to stationary, *ENV*(*t*) changes rapidly as $Jd\omega_r(t)/dt$ in (4.7) disappears and becomes proportional to the level of load torque. Based on the association of the dominant trend of *ENV*(*t*) and the driving condition, the linear trend of *ENV*(*t*) is determined to be the drive-related signal *D*(*t*). Before extracting *D*(*t*), the gradient of *ENV*(*t*), which is denoted as *G*(*t*), is computed for subdivision. When the

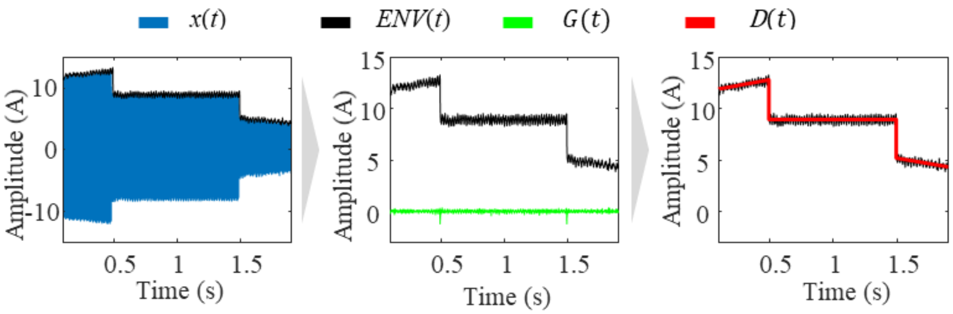

Figure 4-2 The procedure of extracting *D*(*t*) from *ENV*(*t*)

driving condition is switched, *ENV*(*t*) changes drastically; thus, the transition time can be captured at the large gradient points. After subdividing *ENV*(*t*) into several sections, linear regressions of *ENV*(*t*) in each section are calculated. Then, *D*(*t*) is defined as the union of linear estimation. In Fig., *G*(*t*) has two peak points at the transition time, and *D*(*t*) can be determined as the combination of the linear estimations in three subsections that *G*(*t*) divides.

Unlike the previous approaches that decomposed the non-stationary current signal empirically or removed the fundamental current signal using specific filters, the proposed DTCRV method readily extracts the drive-related components which are induced from the torque-current mechanism. The linear regressed *D*(*t*) is a strict equation-based extraction; however, several filters (e.g., moving average or low-pass) can be substituted for the linear regression and applied to various driving conditions.

4.2.2 Drive-tolerant Current Residual

Using *D*(*t*) which is determined in advance, the drive-tolerant current residual *DTCR*(*t*) can be calculated by the subtraction of *D*(*t*) from *ENV*(*t*) as:

$$DTCR(t) = ENV(t) - D(t) \tag{4.8}$$

After $D(t)$ is subtracted, the dependence of DTCR on the driving condition becomes small; therefore, the influences that are not related to the driving conditions are prominent in the DTCR. Also, the fluctuations caused by faults receive more attention. Then, the variance is calculated to arrive at a representation of DTCR, which is defined as:

$$\text{DTCRV} = E(|DTCR(t) - \mu|^2) \tag{4.9}$$

where μ is the average of $DTCR(t)$. DTCRV can be interpreted as the energy of the DTCR, since the energy of the time-series signal is usually defined as a summation of the squared signal and the mean of the DTCR would be zero in the ideal case. When $D(t)$ does not include all time-varying effects, the DTCR could have a bias induced by a complicated driving condition; thus, the variance can compensate for the bias error of the DTCR.

4.2.3 Contribution and Advantage of DTCRV

Through the proposed DTCRV method, the stator current signals under operational driving conditions can be readily utilized to evaluate the health condition of a motor. It is beneficial that the DTCRV method, which is developed on the basis of physical relations between the torque and current of a motor, can be applied with less expertise. To precisely describe the contribution and advantages of the DTCRV, it is compared with two conventional approaches (i.e., TFA-based and signal decomposition-based). Table 4-2 summarizes the comparisons described below. The proposed DTCRV method does not require any information about the fault. In contrast, the two conventional approaches are based on the extraction of fault-related components. Therefore, the two conventional methods are limited to situations where the fault-related information is pre-assigned, such as fault characteristic frequency over time and the decomposition level that the fault patterns reveal. The DTCRV method also does not require any information about the driving condition; instead, it adaptively decreases the effect of speed and load torque conditions by subtracting the linear components in the current envelope. For the TFA-based approach, the speed profile is essential for calculating the characteristic frequency. The load torque condition is optionally used to attempt to compensate for its influence. Furthermore, the DTCRV is less susceptible to the parameter settings and its time-cost is low because the entire process of DTCRV is automatically handled in the time-domain. In contrast, the time-cost for the TFA-based approach is high due to the computation of many convolutions. The signal decomposition-based approach is highly affected by several parameters, such as the type of wavelet function and the appropriate band using the DWT method, or the selection of proper IMFs using the EMD and HHT methods. Finally, the DTCRV method can highlight the current fluctuations through the automatic reduction of drive-related signals.

Table 4-2 Comparison of the proposed DTCRV and two conventional approaches

	Proposed (DTCRV)	TFA-based approach (e.g. PWD)	Signal-based approach (e.g. DWT, EMD, HHT)
Required information about the fault	None	Fault characteristic frequency	Fault-sensitive range that fault patterns reveal
Required information about the driving conditions	None	Speed profile Load torque (optional)	Load torque (optional)
Parameter dependency	Low	Low	High
Time-cost	Low	High	Low

4.3 Case Studies

To validate the effectiveness of the proposed DTCRV method, two experimental studies were explored: 1) a stator inter-turn short (SIS) and 2) misalignment (MSGN). Both cases also include a comparative analysis with other previously published health features, which were described in Section 4.1, to confirm the superiority of the proposed method.

4.3.1 Case Study 1: Stator Inter-turn Short

Figure 4-3 shows the procedure for calculating DTCR from the raw current signal in several driving conditions of NOR; Figure 4-4 shows calculation for SIS2. Comparing the raw current of Figure 4-3 and Figure 4-4 the modulation caused by SIS can be confirmed; the enlarged parts of Figure 4-3 (b) and Figure 4-4 (b) obviously show the severity of modulation due to SIS at the constant speed region. From all $ENV(t)$ of each driving condition in Figure 4-3 and Figure 4-4, it can be seen that $ENV(t)$ was highly influenced by the speed variation and load torque level. The amplitude trend of $ENV(t)$ was largely dominated by the speed variation and was simultaneously proportional to the load torque level. So DTCRs were obtained according to the procedure as described in Figure 4-2. $G(t)$, which was calculated to set the criteria for subdividing $ENV(t)$, had peak points when the speed profile was drastically changed, regardless of the health state of the motor. There appeared two peak points in Figure 4-3 (a-c) and Figure 4-4 (a-c), while only one appeared in Figure 4-3 (d-f) and Figure 4-4 (d-f). Next, $D(t)$ was regressed in each section that the peaks of $G(t)$ divide. Then DTCRs were obtained by subtracting $D(t)$ from $ENV(t)$. The small difference of DTCRs under variable speed and load torque levels indicated the tolerance of DTCR to driving conditions, as shown in DTCRs in Figure 4-3. While the difference of DTCRs depending on driving conditions was small in Figure 4-3, DTCRs of Figure 4-4 highly fluctuated compared to those of Figure 4-3. Therefore, we can confirm that the influence of SIS on DTCR was larger than that of the driving conditions. Furthermore, DTCRs were occasionally amplified at the transient regions in the case of SIS. Not only the instantaneous irregularities that occur right after the speed transition but the deterioration of the stator windings where the current flows could aggravate the fluctuation of DTCR, as shown in the transient sections of DTCRs. Figure 4-5 shows the results of each feature (i.e. E_{PWD}, E_{DWT}, E_{HHT}, and DTCRV), as determined using the PWD, DWT, HHT, and the proposed DTCRV methods, respectively. Each feature was normalized with an average feature value of NOR. E_{PWD}, E_{DWT}, E_{HHT} were calculated based on the conventional methods described in Section 2.2. For E_{PWD}, the magnitudes of the coefficients of PWD around $3fs$ were mean-squared over time. For E_{DWT}, the fifth detail signal, $d5$ was selected and calculated as the sum of squares based on the fact that the frequency band of $d5$ was from 1 kHz to 2 kHz, which contains the characteristic frequency in the constant-speed region, of which the fundamental frequency was 500 Hz. For E_{HHT}, the third IMF of the raw current signal was extracted, and the variance of its instantaneous amplitude was computed. As can be seen in Figure 4-5, DTCRV outperformed the other methods by detecting SIS with one criterion. E_{PWD} and E_{DWT} were proportional to the load torque level and could detect only SIS2 within the same load torque condition. Through the result, we can determine that the effect of load torque condition was difficult to be suppressed or separated using PWD or DWT. The inferior performance of E_{HHT} might be due to the instability of the empirical extraction of IMF.

Table 4-3 quantitatively shows the performance of SIS detection using two measures for class separation: 1) the Fisher discriminant ratio (FDR) [97] and 2) the probability of separation (PoS) [98]. DTCRV had an overwhelmingly better separation capacity in both measures. The outstanding performance of DTCRV was possible because its techniques, which suppress the drive-related components, enhanced its sensitivity to the fault. Further, it is noticeable that the unit computing time of DTCRV was significantly faster than that of E_{PWD} and E_{HHT}, as can be seen in Table. All the time-costs were measured under i7-6700K CPU with 32GB RAM. As DTCRV is calculated in the time-domain only, repeated convolutions to convert signals in the time-domain to the time-frequency domain are not required. Also, the procedure of determining the drive-related signal of DTCRV was much simpler than calculating local maxima and local minima. The results of DTCRV in 50% load torque conditions were sometimes low, as shown in Figure 4-5(a). These results could be explained based on the influence of the control system in deceleration. The motors were forced to stop in the commanded time in different load torque levels and the load torques were also used in deceleration. When the load torque was low, the output torque had to be replenished for the on-time stop; when the load torque was high, the output torque for hindering fast deceleration was required. This explanation was supported by checking the deceleration regions of Figure 4-3 and Figure 4-4. However, it is important to note that DTCRV showed remarkable performance when subjected to both speed profile and load torque variations, although it was affected by the control in deceleration.

Table 4-3 Performance of SIS detection and average time-cost for calculating one feature

	Features	DTCRV (Proposed)	E_{PWD} [40]	E_{DWT} [45]	E_{HHT} [48]
Performance measure	FDR	4.919	0.034	0.027	0.002
	PoS	0.959	0.091	0.082	0.019
Time-cost		0.007±0.002 sec	46.664±4.317 sec	0.004±0.004 sec	0.028±0.005 sec

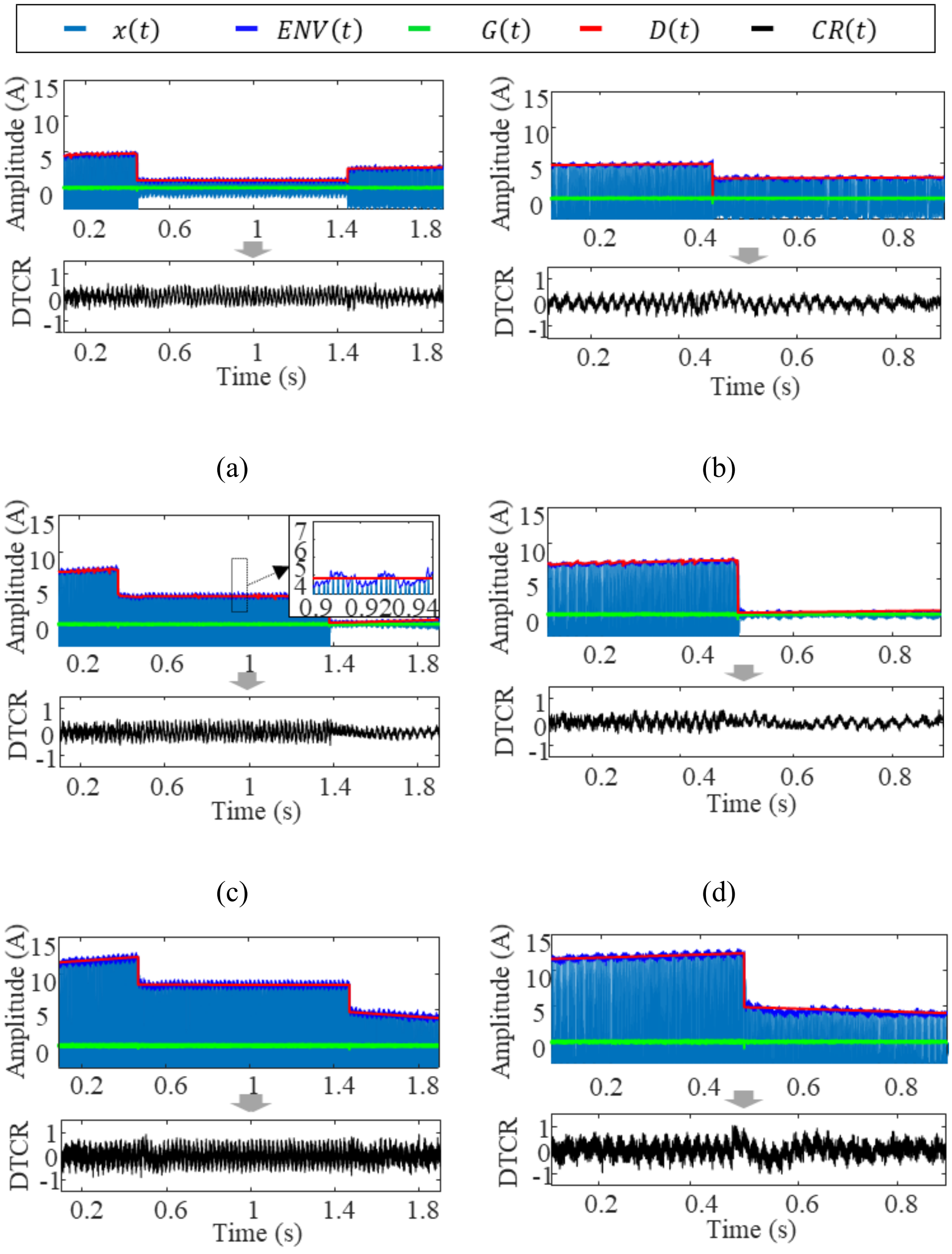

(a) (b)

(c) (d)

(e) (f)

Figure 4-3 The procedure for calculating DTCR in NOR: [speed profile, load torque level] (a) [Trapezoidal, 0%], (b) [Triangle, 0%], (c) [Trapezoidal, 50%], (d) [Triangle, 50%], (e) [Trapezoidal, 100%], and (f) [Triangle, 100%]

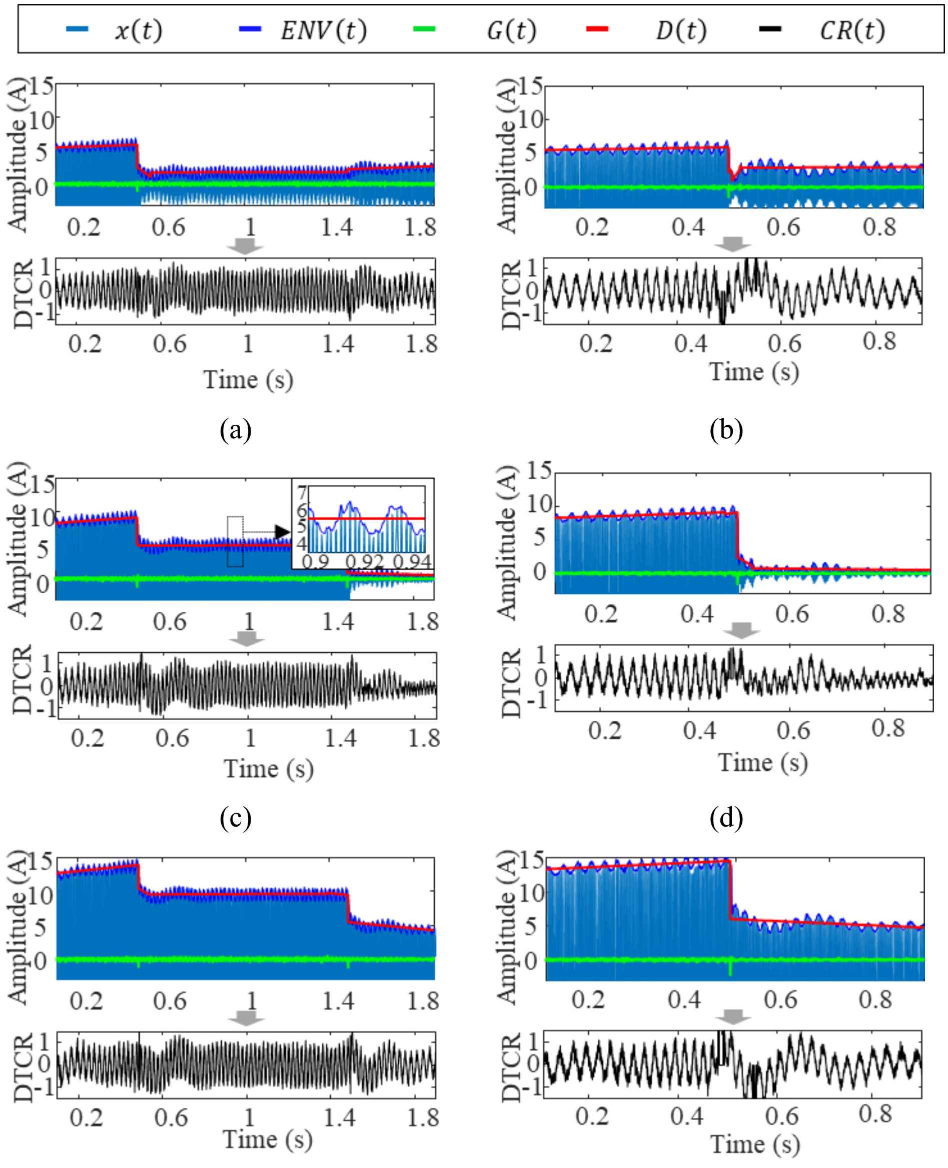

(a) (b) (c) (d) (e) (f)

Figure 4-4 The procedure for calculating DTCR in SIS2: [speed profile, load torque level] (a) [Trapezoidal, 0%], (b) [Triangle, 0%], (c) [Trapezoidal, 50%], (d) [Triangle, 50%], (e) [Trapezoidal, 100%], and (f) [Triangle, 100%]

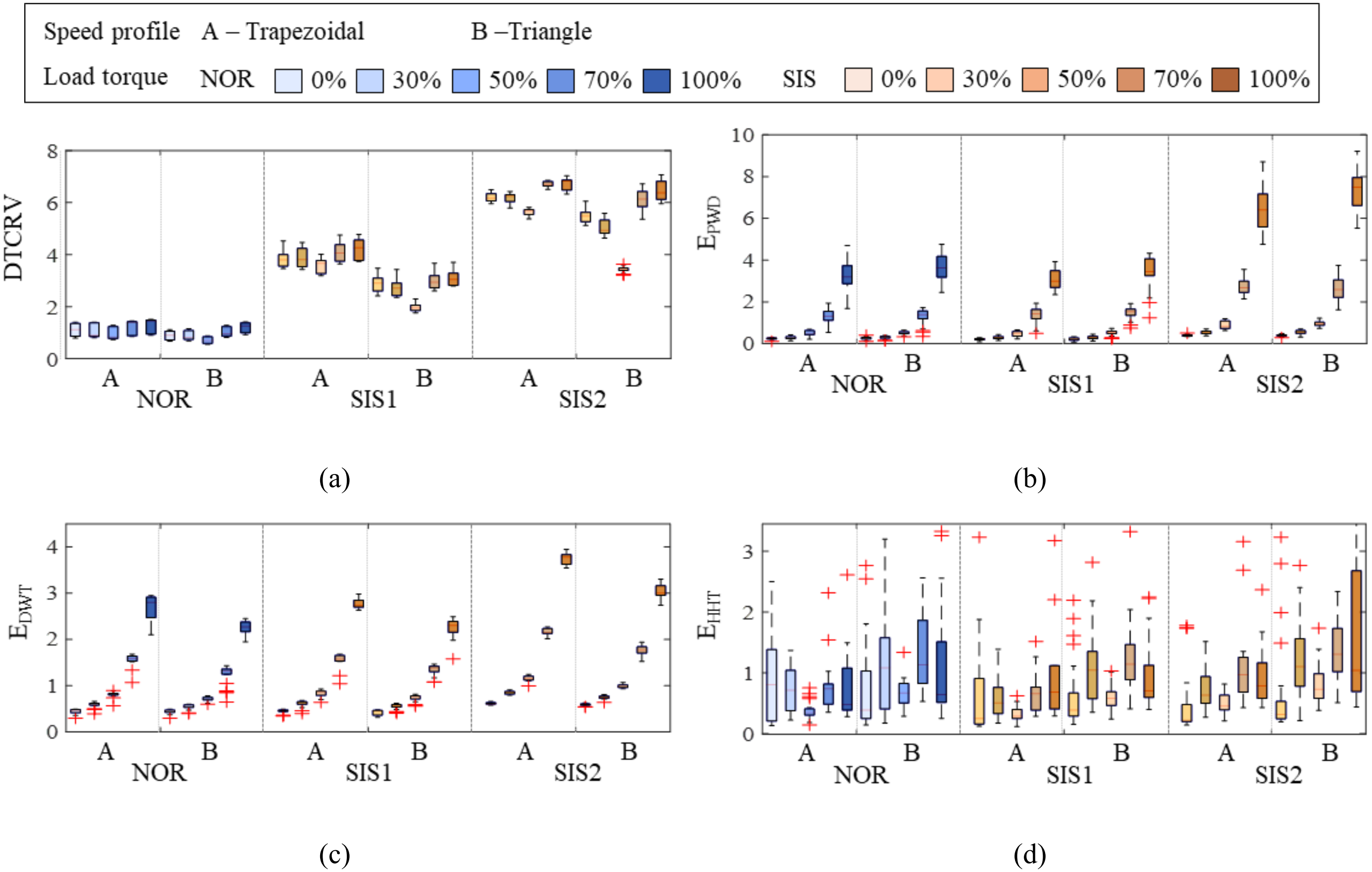

(a) (b)

(c) (d)

Figure 4-5 Results of the proposed and the conventional methods under SIS: (a) DTCRV, (b) PWD, (c) DWT, (d) HHT.

4.3.2 Case Study 2: Misalignment

Figure 4-6 shows the procedure for calculating DTCR from the raw current signal in several driving conditions of MSGN2. Comparing the raw current signals in Figure 4-6 with those of the corresponding operating conditions in NOR (shown in Figure 4-3), the amplitude became larger. This was because much output torque was required to compensate for the interference, which MSGN induced to normal output torque. Also, *ENV*(*t*)s of MSGN showed more peak shapes, while those of SIS had the form of modulation, as shown in the enlarged parts of Figure 4-3 (b) and Figure 4-6 (b), respectively. The large fluctuation of *ENV*(*t*) sometimes caused the oscillated *G*(*t*), as can be seen in Figure 4-6 (a, b). Nevertheless, it was not hard to divide sections because the peak points of *G*(*t*) were determined relatively. Comparing DTCRs in Figure 4-6 with those of Figure 4-4, DTCRs in MSGN more fluctuated than those of SIS. Through this large fluctuation, we can suggest that DTCR is more sensitive to mechanical faults.

Figure 4-7 shows the results of each feature (i.e. E_{PWD}, E_{DWT}, E_{HHT}, and DTCRV), as determined using the PWD, DWT, HHT, and the proposed DTCRV methods, respectively. The normalization of each feature and the calculation of the conventional features were conducted in the same way described in Section 2.3. For E_{PWD}, the magnitudes of the coefficients of PWD around $f_s \pm f_r/2$ were mean-squared over time. For E_{DWT}, the seventh detail signal *d7* was selected and calculated as the sum of squares because the frequency band of *d7* was from 250 Hz to 500 Hz, which was able to contain the time-varying characteristic frequency $f_s \pm f_r$. For $E_{HHT,}$ the second IMF of the raw current signal was extracted, and the variance of its instantaneous amplitude was computed. Like the results in Section 4.3.1, the behaviors of DTCRV were robust to variable speed profile and load torque conditions. From Figure 4-7 (b, c), the influence of the load torque levels on E_{PWD} and E_{DWT} seemed to be higher than that of MSGN. E_{PWD} could detect MSGN at the high-load torque levels; however, MSGNs under 50% or less load torque levels were not distinguishable from NOR at 100% load torque level. E_{DWT} had a significant variance in each operating condition due to the insufficient signal decomposition; the characteristics of MSGN were concealed in the load torque conditions. As shown in Figure 4-7 (d), E_{HHT} was able to detect MSGN2 because the drive-related components were separated in the first IMF; however, E_{HHT} could not detect MSGN1.

Table 4-4 quantitatively describes the performance and unit computing time of all the features, which were measured in the same state as in Section 4.3.1. The result of high FDR and PoS values with the small time-cost in DTCRV confirmed its outstanding performance compared to the other three features. Though both MSGNs showed the higher DTCRV values, as compared to those of NOR, the DTCRVs of MSGN1 and MSGN2 did not linearly increase, and DTCRVs of MSGN2 were spread in the trapezoidal speed profile case (see Figure 4-7 (a)). It seems possible that these results were due to the slight misalignment that resulted from the repeated experimental disturbances. However, it is noticeable that the proposed DTCRV approach can promptly detect the incipient MSGN without any information about the fault or driving conditions.

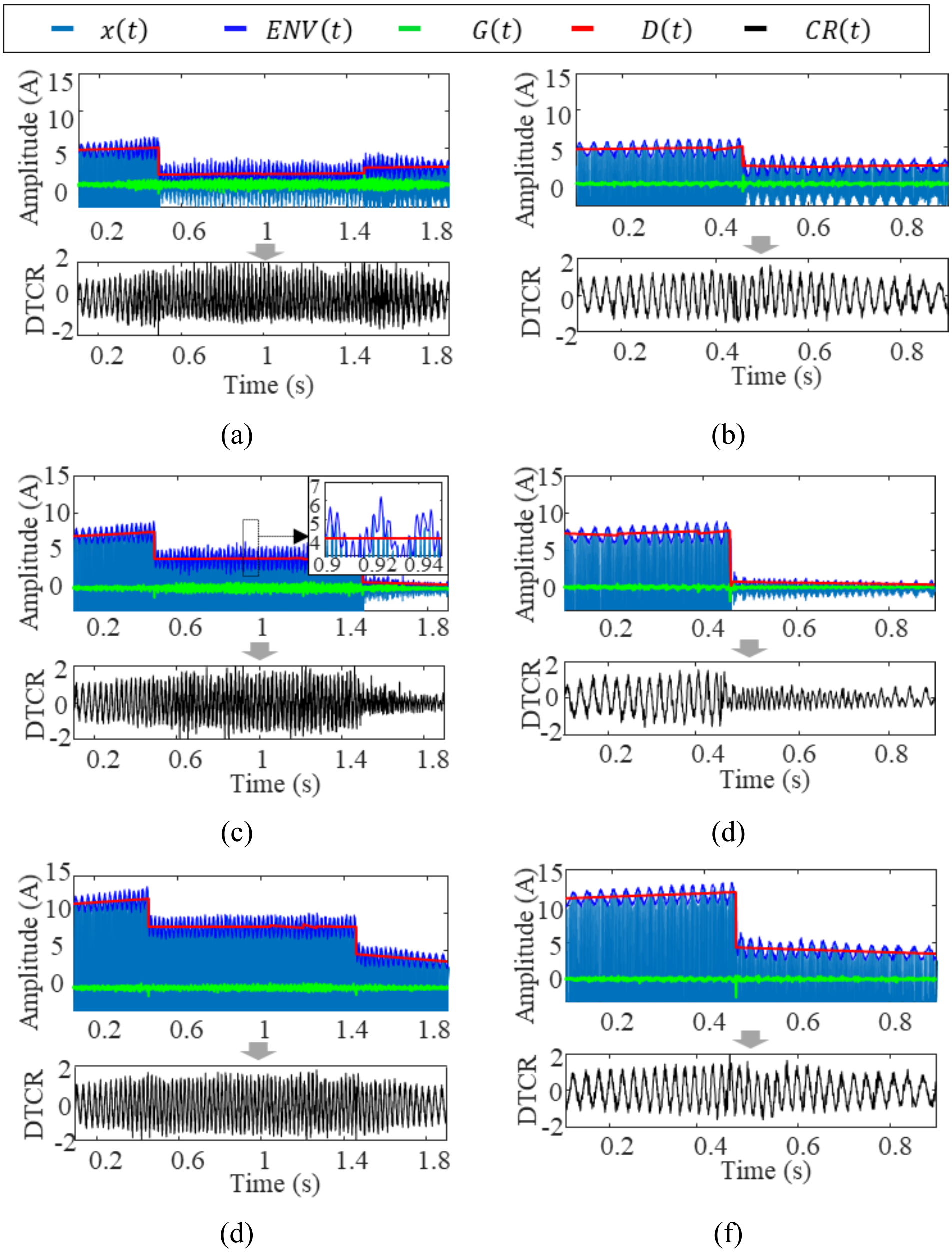

Figure 4-6 The procedure for calculating DTCR in MSGN2: [profile, load torque] (a) [Trapezoidal, 0%], (b) [Triangle, 0%], (c) [Trapezoidal, 50%], (d) [Triangle, 50%], (e) [Trapezoidal, 100%], and (f) [Triangle, 100%].

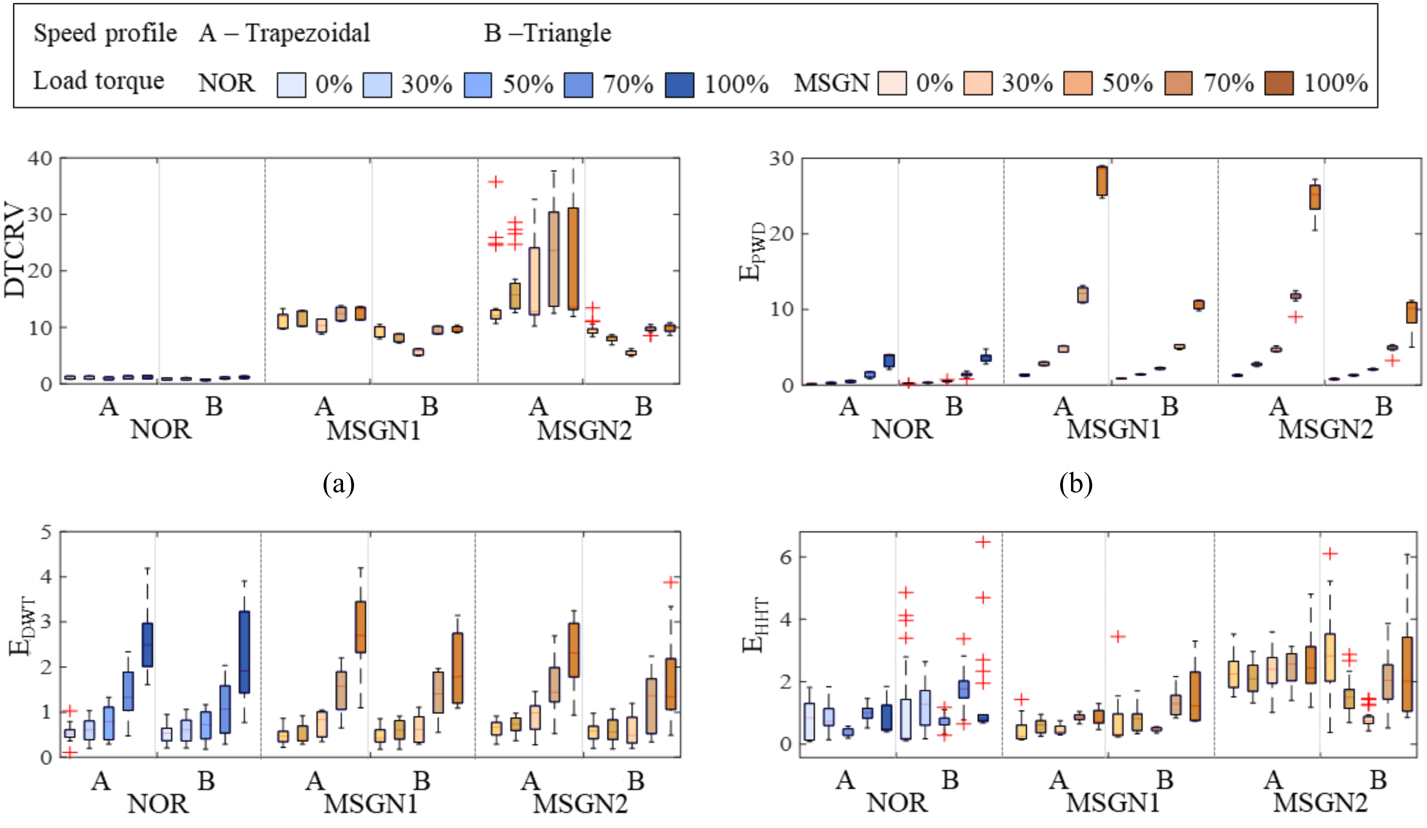

(a) (b)

(c) (d)

Figure 4-7 Results of the proposed and the conventional methods under MSGN: (a) DTCRV, (b) PWD, (c) DWT, (d) HHT.

Table 4-4 Performance of MSGN detection and average time-cost for calculating one feature

	Features	DTCRV (Proposed)	E_{PWD} [40]	E_{DWT} [45]	E_{HHT} [48]
Performance measure	FDR	2.986	0.258	0.001	0.222
	PoS	0.873	0.433	0.016	0.254
Time-cost		0.007±0.002 sec	44.113±3.396 sec	0.004±0.007 sec	0.027±0.007 sec

Through the results of simulation and two experiments, the DTCRV method have shown the three noticeable remarks: 1) DTCRV was able to detect a fault without being affected by the driving condition (i.e., speed profiles and load torque levels), while the conventional methods were dominated by the driving conditions. 2) Neither motor-specific information nor parameter settings for signal decomposition were required to calculate DTCRV. 3) The computational time of DTCRV was low.

4.4 Summary and Discussion

This chapter proposed a new, drive-tolerant current residual variance (DTCRV) method for detecting faults under operational speed and load torque conditions. The proposed method extracted the envelope of the raw current signal to emphasize its modulation, which contains both drive-related and fault properties. Then, drive-related components were estimated using gradient-based linear regression. The DTCR, which was taken by subtracting drive-related components from the envelope signal, highlighted the unexpected oscillations from the abnormal state. Finally, the variance was computed to quantify the variation of the DTCR. Two case studies that investigated the different fault modes (i.e., SIS and MSGN) were demonstrated to validate the performance of the proposed approach. These case studies showed that the DTCRV method could detect each fault under several driving conditions, while the conventional methods using PWD, DWT, and HHT suffered from the effect of driving conditions. The primary benefits of the proposed method are that it can detect an incipient abnormal state without requiring information about the fault or the driving condition. Moreover, the computational time of DTCRV is far less than that of the

TFA-based approach, motor domain knowledge is not required, and the number of parameters that DTCRV demands is also less than that of both TFA-based and signal decomposition-based approaches. Future work can be conducted to identify fault modes considering control constraints under a wider range of driving conditions. Further, DTCRV will be investigated and applied to other motors embedded in industrial robots or electric vehicles.

Sections of this chapter have been published or submitted as the following journal articles:

1) **C. H. Park,** J. Lee, H. Kim, C. Suh, M. Youn, Y. Shin, S. H. Ahn, and B. D. Youn, "Drive-Tolerant Current Residual Variance (DTCRV) for Fault Detection of a Permanent Magnet Synchronous Motor Under Operational Speed and Load Torque Conditions." IEEE Access, vol. 9, pp. 49055-49068, 2021

Chapter 5

Physics-informed Health Image for Fault Diagnosis: Instantaneous Current Residual Map (ICRM)

5.1 Stator Current Signal with Faults Under Variable-speed Conditions

Several motor current models have been proposed that focus on the phase modulation effect that arises from a fault under steady-state conditions. In [19], an induction motor current model was derived under variable-speed conditions, considering gear faults, modulation effects, and rotor eccentricity. In case of a PMSM considering the same type of faults, both amplitude and phase modulations appear in stator current signal. To offer further improvement from the conventional derivations, this section derives a motor current model of a PMSM under time-varying speed conditions considering fault-induced effects.

The acceleration of a PMSM rotor as a function of time t can be expressed as:

$$a(t) = \frac{1}{J}[T_{\mathrm{e}}(t) - T_{\mathrm{L}}(t)] \tag{5.1}$$

where J is the inertia of a rotating system; $T_{\mathrm{e}}(t)$ is the electromagnetic torque; and

$T_L(t)$ is the load torque. Considering the load torque $T_L(t)$ as a combination of the average load torque $T_{L0}(t)$ and fault-induced load torque oscillation $T_f(t)$, it can be written as [99]:

$$T_{\mathrm{L}}(t) = T_{\mathrm{L0}}(t) + T_{\mathrm{f}}(t)\sin\left[\int_0^t \omega_{\mathrm{f}}(\tau)d\tau + \varphi_{\mathrm{f}}\right]d\tau \tag{5.2}$$

where τ is the time variable; and $\omega_f(\tau)$ and φ_f are the fault-related frequency and phase, respectively. Then, the rotor speed of the PMSM $\omega_r(t)$ can be derived with the integral of (5.1) as:

$$\omega_{\mathrm{r}}(t) = \omega_{\mathrm{r0}}(t) + \frac{1}{J}\int_0^t T_{\mathrm{f}}(\tau)\sin\left[\int_0^\tau \omega_{\mathrm{f}}(\upsilon)d\upsilon + \varphi_{\mathrm{f}}\right]d\tau \tag{5.3}$$

where $\omega_{r0}(t)$ is the instantaneous average rotor speed; and υ is the time variable. The rotor angular position of the PMSM $\theta_r(t)$ can be calculated as the integral of (5.3) over time as:

$$\theta_{\mathrm{r}}(t) = \int_0^t \omega_{\mathrm{r0}}(\tau)d\tau + \frac{1}{J}\int_0^t\int_0^\tau T_{\mathrm{f}}(\upsilon)\sin\left[\int_0^\upsilon \omega_{\mathrm{f}}(\nu)d\nu + \varphi_{\mathrm{f}}\right]d\upsilon d\tau \tag{5.4}$$

where ν is the time variable. Based on (2.11), the total magnetomotive force (MMF) of the PMSM $F(\theta, t)$ can be expressed, using (2.12), as:

$$F(\theta,t) = F_{\mathrm{s}}\sin\left[p\theta_{\mathrm{s}} - \int_0^t \omega_{\mathrm{e}}(\tau)d\tau\right] + F_{\mathrm{r}}\sin\left[p\theta_{\mathrm{s}} - p\theta_{\mathrm{r}}(t) - \int_0^t \omega_{\mathrm{re}}(\tau)d\tau\right] \tag{5.5}$$

where p is the pole pair number of the PMSM; $\omega_e(\tau)$ is the power supply speed; and $\omega_{re}(\tau)$ is the excitation current of the permanent magnet rotor, unlike the rotor of an induction motor is indirectly excited from the stator [100].

Even though the airgap flux density can be calculated as the product of $F(\theta, t)$ and the airgap permeance, for simplicity, the airgap permeance is usually assumed to be constant. airgap eccentricity is inevitable due to manufacturing and assembling errors. Considering the amplitude modulation effect that the airgap eccentricity induces, the total airgap flux of PMSM $\Phi(t)$, which can be calculated by integrating the airgap flux density with respect to the winding structure, is expressed as:

$$\begin{aligned}\Phi(t) = &\left\{1-\alpha\cos\left[\int_0^t \omega_{\mathrm{r}}(\tau)d\tau+\eta\right]\right\}\times \\ &\left\{\Phi_{\mathrm{s}}\sin\left[\int_0^t \omega_{\mathrm{e}}(\tau)d\tau\right]+\Phi_{\mathrm{r}}\sin\left[\int_0^t \omega_{\mathrm{e}}(\tau)d\tau+\frac{p}{J}\int_0^t\int_0^\tau T_{\mathrm{f}}(\upsilon)\sin\left[\int_0^\upsilon \omega_{\mathrm{f}}(\nu)d\nu+\varphi_{\mathrm{f}}\right]d\upsilon d\tau+\int_0^t \omega_{\mathrm{re}}(\tau)d\tau\right]\right\}\end{aligned} \tag{5.6}$$

where Φ_{s} and Φ_{r} are the amplitudes of the airgap flux caused by the stator and rotor MMFs, respectively; α is a modulation index representing the degree of dynamic eccentricity; and η is the initial phase. To simplify the equations, the instantaneous speed term $W(t)$, the instantaneous rotor excitation speed term $W_{\mathrm{re}}(t)$, the amplitude modulation term $A_{\mathrm{M}}(t)$, and the phase modulation term $P_{\mathrm{M}}(t)$ are defined, respectively, as:

$$\begin{aligned}&W(t)=\int_0^t \omega_{\mathrm{r}}(\tau)d\tau, \\ &W_{\mathrm{re}}(t)=\int_0^t \omega_{\mathrm{re}}(\tau)d\tau, \\ &A_{\mathrm{M}}(t)=1-\alpha\cos\left[\int_0^t \omega_{\mathrm{r}}(\tau)d\tau+\eta\right], \\ &P_{\mathrm{M}}(t)=\frac{p}{J}\int_0^t\int_0^\tau T_{\mathrm{f}}(\upsilon)\sin\left[\int_0^\upsilon \omega_{\mathrm{f}}(\nu)d\nu+\varphi_{\mathrm{f}}\right]d\upsilon d\tau\end{aligned} \tag{5.7}$$

According to a motor stator voltage equation (see (2.6)), the motor stator current $x(t)$ can be described as:

$$\begin{aligned}x(t) &= \frac{1}{R_{\mathrm{s}}}\left[\mathrm{V}(t)-\frac{d\Phi(t)}{dt}\right] \\ &= I_{\mathrm{s0}}\sin W(t)-\frac{\Phi_{\mathrm{s}}}{R_{\mathrm{s}}}\frac{d}{dt}\left\{A_{\mathrm{M}}(t)\sin W(t)\right\}-\frac{\Phi_{\mathrm{r}}}{R_{\mathrm{s}}}\frac{d}{dt}\left\{A_{\mathrm{M}}(t)\sin\left[W(t)+P_{\mathrm{M}}(t)+W_{re}(t)\right]\right\}\end{aligned} \tag{5.8}$$

where $\mathrm{V}(t)$ is the power supply voltage; R_{s} is the stator resistance; and I_{s0} is the amplitude of the motor stator current flowing the stator resistance. Denoting $I_{\mathrm{s}}=\Phi_{\mathrm{s}}/R_{\mathrm{s}}$ and $I_{\mathrm{r}}=\Phi_{\mathrm{r}}/R_{\mathrm{s}}$, (5.8) can be rewritten as:

$$\begin{aligned}x(t) &= \left\{I_{\mathrm{s0}} - I_{\mathrm{s}}\dot{A}_{\mathrm{M}}(t)\right\}\sin W(t) - I_{\mathrm{s}}A_{\mathrm{M}}(t)\omega_{\mathrm{e}}(t)\cos W(t) - I_{\mathrm{r}}\dot{A}_{\mathrm{M}}(t)\sin\left[W(t) + P_{\mathrm{M}}(t) + W_{\mathrm{re}}(t)\right] \\ &\quad - I_{\mathrm{r}}A_{\mathrm{M}}(t)\left\{\omega_{\mathrm{e}}(t) + \dot{P}_{\mathrm{M}}(t) + \omega_{\mathrm{re}}(t)\right\}\cos\left[W(t) + P_{\mathrm{M}}(t) + W_{\mathrm{re}}(t)\right] \\ &= \left[\left\{I_{\mathrm{s0}} - I_{\mathrm{s}}\dot{A}_{\mathrm{M}}(t)\right\}^2 + \left\{I_{\mathrm{s}}A_{\mathrm{M}}(t)\omega_{\mathrm{e}}(t)\right\}^2\right]^{-\frac{1}{2}}\sin\left[W(t) + \arctan\left[\frac{I_{\mathrm{s}}A_{\mathrm{M}}(t)\omega_{\mathrm{e}}(t)}{I_{\mathrm{s}}\dot{A}_{\mathrm{M}}(t) - I_{\mathrm{s0}}}\right]\right] \\ &\quad - I_{\mathrm{r}}\left[\dot{A}_{\mathrm{M}}(t)^2 + \left\{A_{\mathrm{M}}(t)\left(\omega_{\mathrm{e}}(t) + \dot{P}_{\mathrm{M}}(t) + \omega_{\mathrm{re}}(t)\right)\right\}^2\right]^{-\frac{1}{2}}\sin\left[\begin{array}{l}W(t) + P_{\mathrm{M}}(t) + W_{\mathrm{re}}(t) \\ + \arctan\left[\dfrac{A_{\mathrm{M}}(t)(\omega_{\mathrm{e}}(t) + \dot{P}_{\mathrm{M}}(t) + \omega_{\mathrm{re}}(t))}{\dot{A}_{\mathrm{M}}(t)}\right]\end{array}\right]\end{aligned} \tag{5.9}$$

where the overdot appearing above $A_{\mathrm{M}}(t)$ and $P_{\mathrm{M}}(t)$ is used to indicate a derivative taken with respect to time.

It can be confirmed from (5.9) that the motor stator current exhibits both phase as well as amplitude modulations in a faulty state. In addition, operating conditions (i.e., the power supply speed $\omega_{\mathrm{e}}(t)$ and the instantaneous speed $W(t)$) significantly affect the motor stator current signal. For accurate fault diagnosis for a PMSM under variable-speed conditions, it is thus of great importance to accomplish feature engineering that highlights fault-induced amplitude and phase modulations while eliminating the effect of variable operating conditions. There has been an attempt to develop a health feature that considers a drive-related component in the instantaneous amplitude of a motor stator current signal under variable-speed and load torque conditions [69]; however, to the best of the authors' knowledge, there is no health feature that considers fault-induced phase as well as amplitude modulations in a motor stator current signal measured from a PMSM under variable operating conditions.

5.2 Proposed ICRM Method

This section explains how to construct ICRM as the input image to a CNN model for fault diagnosis of a PMSM under variable-speed profiles and load torque conditions.

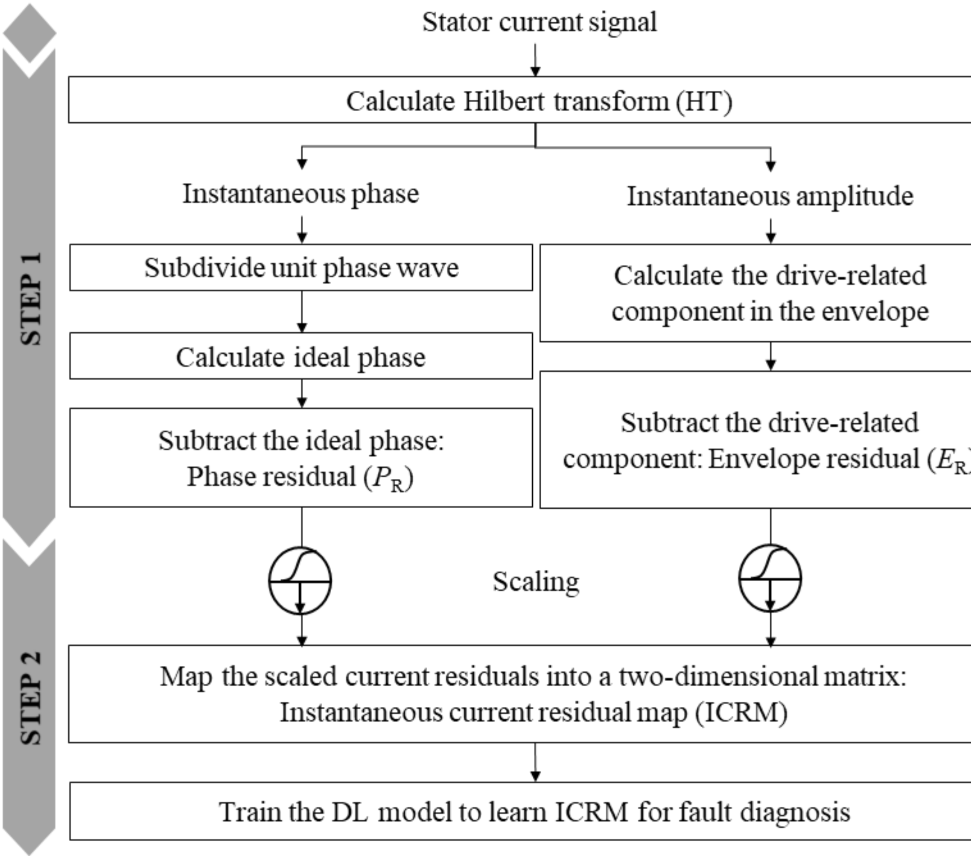

Figure 5-1 The framework of the proposed ICRM method

Figure 5-1 shows a framework of ICRM and the following subsections provide the details of each step.

5.2.1 Step 1: Calculation of Current Residuals

First, a motor stator current signal is converted to an analytic signal using Hilbert transform. Considering that the main power supply frequency is predominant in the motor stator current signal, the discrete analytic signal of the motor stator current, denoted by $x_a[n]$, can be expressed as:

$$x_a[n] = I[n]e^{j\psi[n]} \tag{5.10}$$

where $I[n]$ and $\psi[n]$ are the instantaneous amplitude (i.e., the envelope) and instantaneous phase of the motor stator current, respectively; and n is positive integers for discrete time.

Then, the phase and envelop residuals, denoted by P_R, and E_R, are calculated in the time domain, respectively. To calculate the phase residual $P_R[n]$, the unit instantaneous phase of the motor stator current signal is determined from $-\pi$ to π. Then, the ideal phase, which is a linear shape from $-\pi$ to π, is subtracted from the instantaneous phase as:

$$P_R[n] = \psi[n] - \left(\frac{2\pi}{M} n - \pi \right) \tag{5.11}$$

where the bracket term on the right-hand side is the ideal phase. Note that the data length M changes with the speed of the unit instantaneous phase. Thus, the physical meaning of the phase residual is a degree of phase irregularity without regard for the speed variation.

To calculate the envelop residual E_R, the drive-related component is subtracted from the envelop of the motor stator current signal. Since the magnitude of the envelop is proportional to that of the electromagnetic torque, which drives the rotating system, the dominant trend of the envelop can thus be assumed to contain the drive-related component [69]. Considering the electromechanical torque equation with the envelop, the drive-related component $D[n]$ can be described as:

$$D[n] \cong J\frac{d\omega_r[n]}{dt} + B\omega_r[n] + T_{L0} \tag{5.12}$$

where B is the friction coefficient; ω_r is the rotating speed; and T_{L0} is the constant load torque. Then, the envelop residual is computed as:

$$E_{\mathrm{R}}[n] = I[n] - D[n] \tag{5.13}$$

The physical meaning of the envelop residual is a degree of amplitude irregularity, which is less dependent on the variable speed and load torque conditions.

Since the phase and envelop residuals are obtained from the motor stator current, here and hereafter, they are called current residuals (CRs) in this study. The schematic procedure of calculating the CRs is described in Figure 5-2. It is worth pointing out that, by subtracting the ideal phase and the drive-related component from the instantaneous phase and the envelop of the motor stator current signal, respectively, the CRs can highlight the fault-related information while suppressing the influence of variable-speed and load torque conditions.

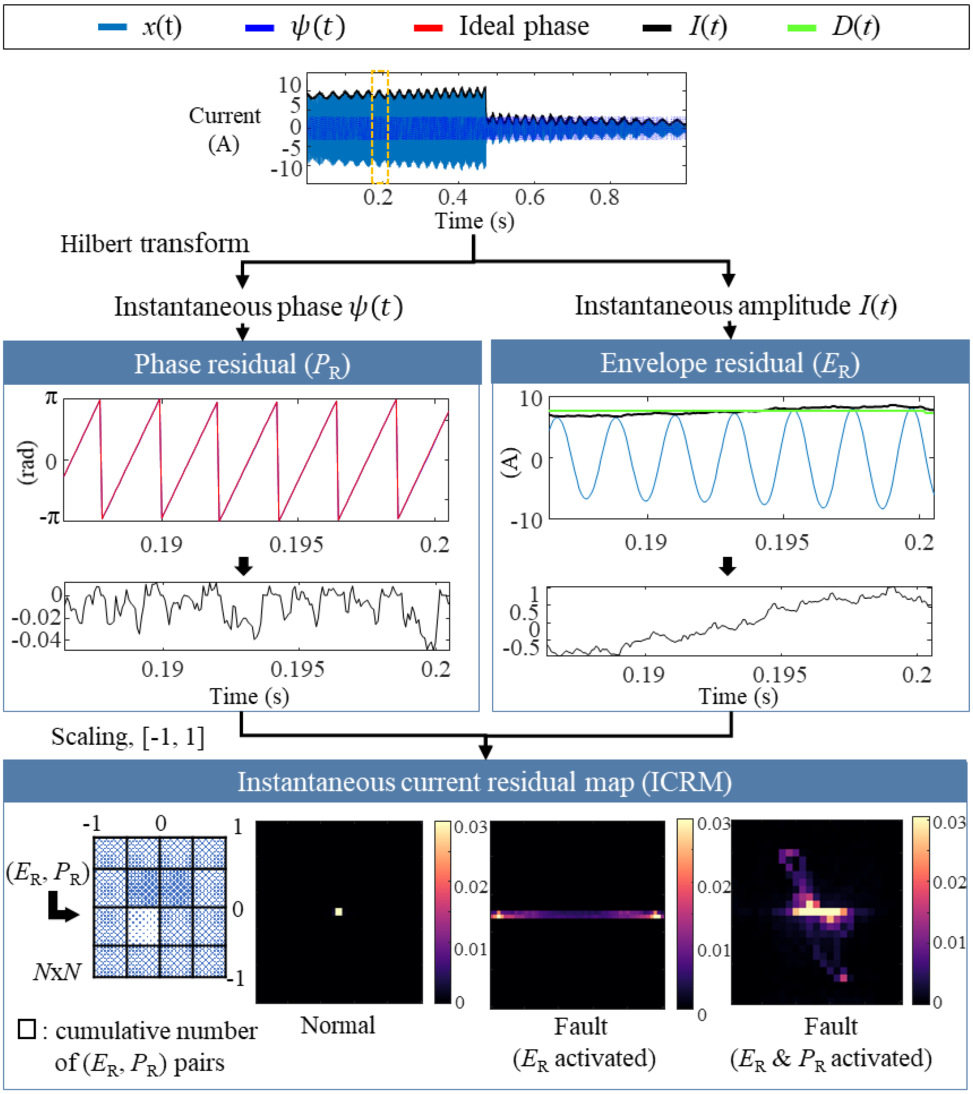

Figure 5-2 The schematic procedure of calculating ICRM using the stator current signal

5.2.2 Step 2: Transformation of the Current Residuals to a Health Image

The CRs (i.e., the envelop and phase residuals, E_R and P_R) calculated in Step 1 are scaled and spread into a 2D matrix. For scaling, a *tanh* activation function is used to scale each residual from -1 to 1 in this study; however, any activation function can be adopted, according to the distribution of the residuals. After the scaled CRs are paired up in the time domain, the size of the 2D matrix ($N\times N$) is determined, and its rows and columns are assigned with a range from -1 to 1, divided by N, respectively. Since each entity of the 2D matrix is the cumulative number of the scaled CR pairs in the assigned range, every scaled CR pair is distributed into the 2D matrix. In principle, if there are neither fault-induced amplitude nor phase modulations in a motor stator current signal, the values of the scaled CRs are nearly zero because the CRs indicate a degree of irregularity. This implies that most of the scaled CR pairs are expected to be concentrated around the center of ICRM in a normal state, while they will spread in faulty states (see the ICRM part of Figure 5-2). The scaled CR pairs are likely to spread along the center horizontal direction of ICRM in a faulty state giving rise to amplitude modulation, while they would be distributed along the vertical direction in a faulty state affecting phase modulation. For instance, amplitude modulation of the motor stator current can be induced when the amplitude of airgap flux waves is modulated by a stator inter-turn short (electrical fault) [80]; whereas, a misalignment (mechanical fault) may cause phase and amplitude modulations due to the load torque oscillation and subordinate eccentricity, respectively [99], [100]. Therefore, a type of faults can be figured out qualitatively by analyzing a degree or shape of spreading in ICRM. Then, ICRM is used as the 2D input image to train a CNN model for learning boundaries between faulty states, thereby quantitatively identifying a health state.

5.3 Experimental Validation

To validate the effectiveness of ICRM for CNN-based fault diagnosis under variable operating conditions, the experimental dataset which was explained in Chapter 3, was examined.

5.3.1 CNN Architecture for Fault Diagnosis

To fairly compare the performance of each input, the same CNN model was used. The architecture of the CNN model was comprised with three residual blocks, a global average pooling layer (GAP), and a fully connected layer (FC), as described in Figure 5-3, which was inspired by [101]. The hyper-parameters of convolutional layers (CONV) and batch normalization layers (BN) in the CNN model are summarized in Table 5-1. Also, the specific information of the CNN model including output shape and the number of parameters is described in Table 5-2, which were applied identically to all types of inputs at comparative analysis.

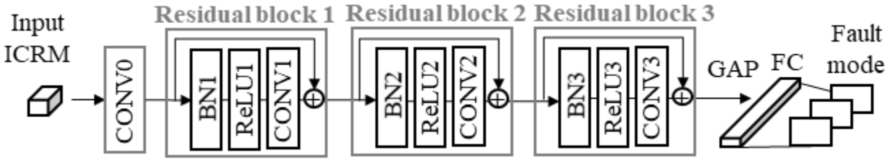

Figure 5-3 The CNN architecture used in the case study

Table 5-1 The model parameters of the CNN architecture

Layer	Abbreviation	Parameter
Convolutional layer	CONV0	kernel size: 11, number of filters: 16, stride: 2, padding: 5
	CONV1, CONV2, CONV3	kernel size: 11, number of filters: 32, stride: 2, padding: 5
Batch normalization layers	BN1, BN2, BN3	Momentum=0.1
ReLU activation	ReLU1, ReLU2, ReLU3	None

Table 5-2 The specific information of the CNN architecture

Type	Output shape	Number of parameters
Input	[1x50x50]	
CONV0	[16x25x25]	1,952
Residual block 1	[32x13x13]	62,016
Residual block 2	[32x7x7]	124,000
Residual block 3	[32x4x4]	124,000
GAP, FC	[32x3]	99
Total		312,067

5.3.2 Fault Diagnosis Results Using ICRM

Figure 5-4 shows the ICRM results for each health state in various operating conditions. While the differences of the ICRM results with different speed profiles and load torque conditions are marginal, the differences of ICRM according to health state are significant. This was confirmed by comparing the distributions of the normal state and other faults; where CRs of the normal state were concentrated on the center, without regard to the operating condition and those of faulty states were extended out horizontally. In particular, the significant vertical spread of CRs in a misalignment state indicates a large amount of P_R. According to the explanation in Section 2.3.2, electrical faults (e.g. stator inter-turn shorts) increase the AM of the currents; further, mechanical faults (e.g. misalignment) affect the PM of the current. From this point of view, the ICRM approach was confirmed to follow the previous physical inspection of the current in faulty states, and was not affected by the operating conditions.

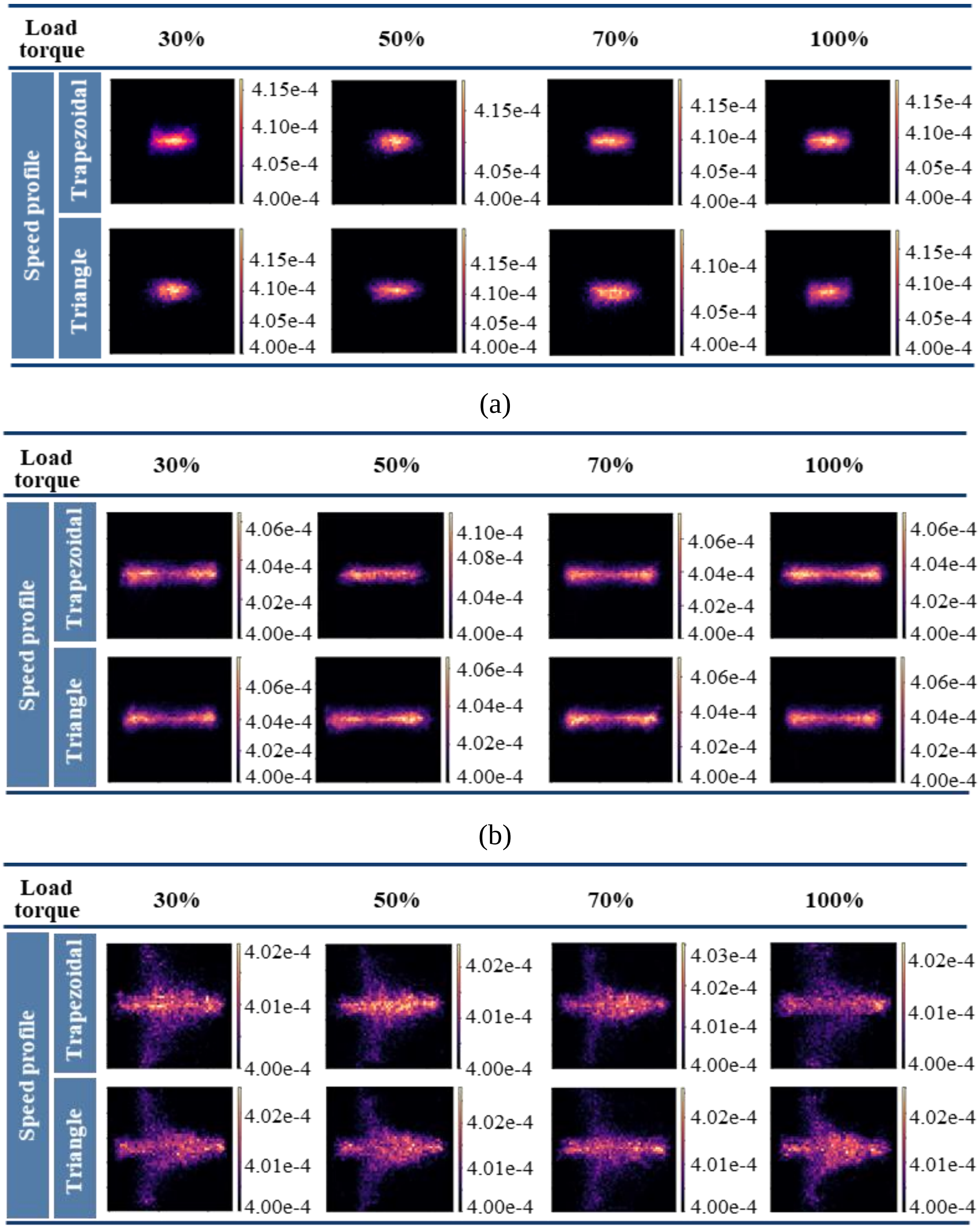

(a)

(b)

(c)

Figure 5-4 ICRM results: (a) Normal, (b) Stator inter-turn short and (c) Misalignment

Using the ICRMs as the input, the CNN model was trained with 3000 epochs with 64 mini-batch, where the learning rate was 1e-4. Figure 5-5 visualizes the input ICRM and the convolutional layers in each residual block using test data from t-stochastic neighbor embedding (t-SNE). The health state was already divided in rough form by the ICRM itself (see Figure 5-5 (a)) and then gradually clustered by fault type as the ICRMs passed through the residual blocks (see Figure 5-5 (b) to (e)). It can be inferred that the ICRM could perform as a fault indicator and the CNN model which trained ICRM could exploit more elaborate fault-related features. Furthermore, the intensely activated weights of the first convolutional layer of the trained CNN model were visualized using gradient-weighted class activation mapping (Grad-CAM), as can be seen in Figure 5-6. Since the first convolutional layer is expected to learn the broad characteristics of the input data, the majority results of Grad-CAM highlighted the most noticeable part of the ICRM. The center was strongly dominant in the normal case, while the horizontal parts were highlighted in the case of a stator inter-turn short. For misalignment, the vertical parts were also accentuated, along with the horizontal parts. These results show that the Grad-CAM spotlighted the expected part of the ICRM, in which the CRs of the faulty state are located. Thus, the CNN model was confirmed to properly train ICRM for fault diagnosis.

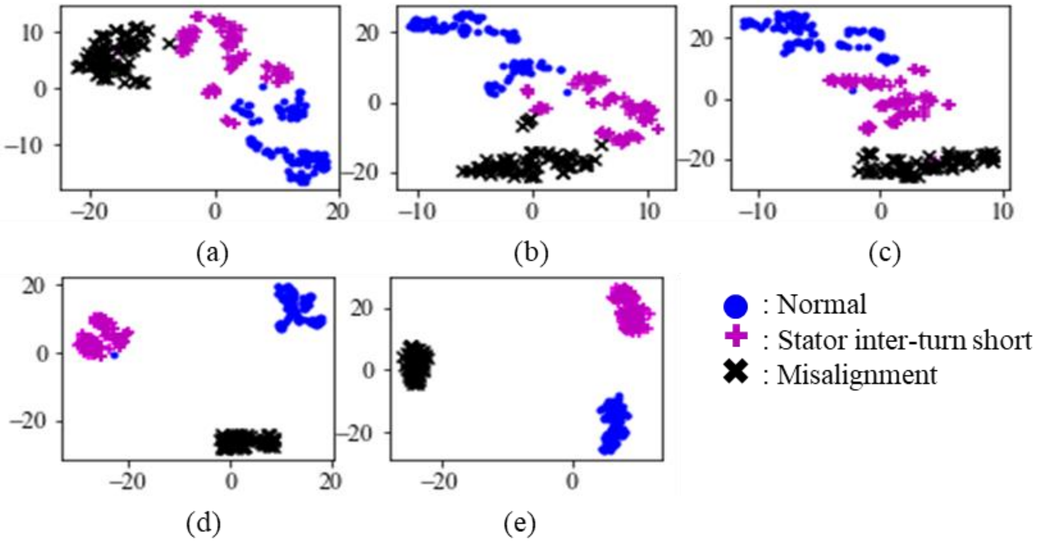

Figure 5-5 t-SNE result of input and convolutional layers using test dataset: (a) Input, (b) CONV0, (c) Residual block 1, (d) Residual block 2 and (e) Residual block 3

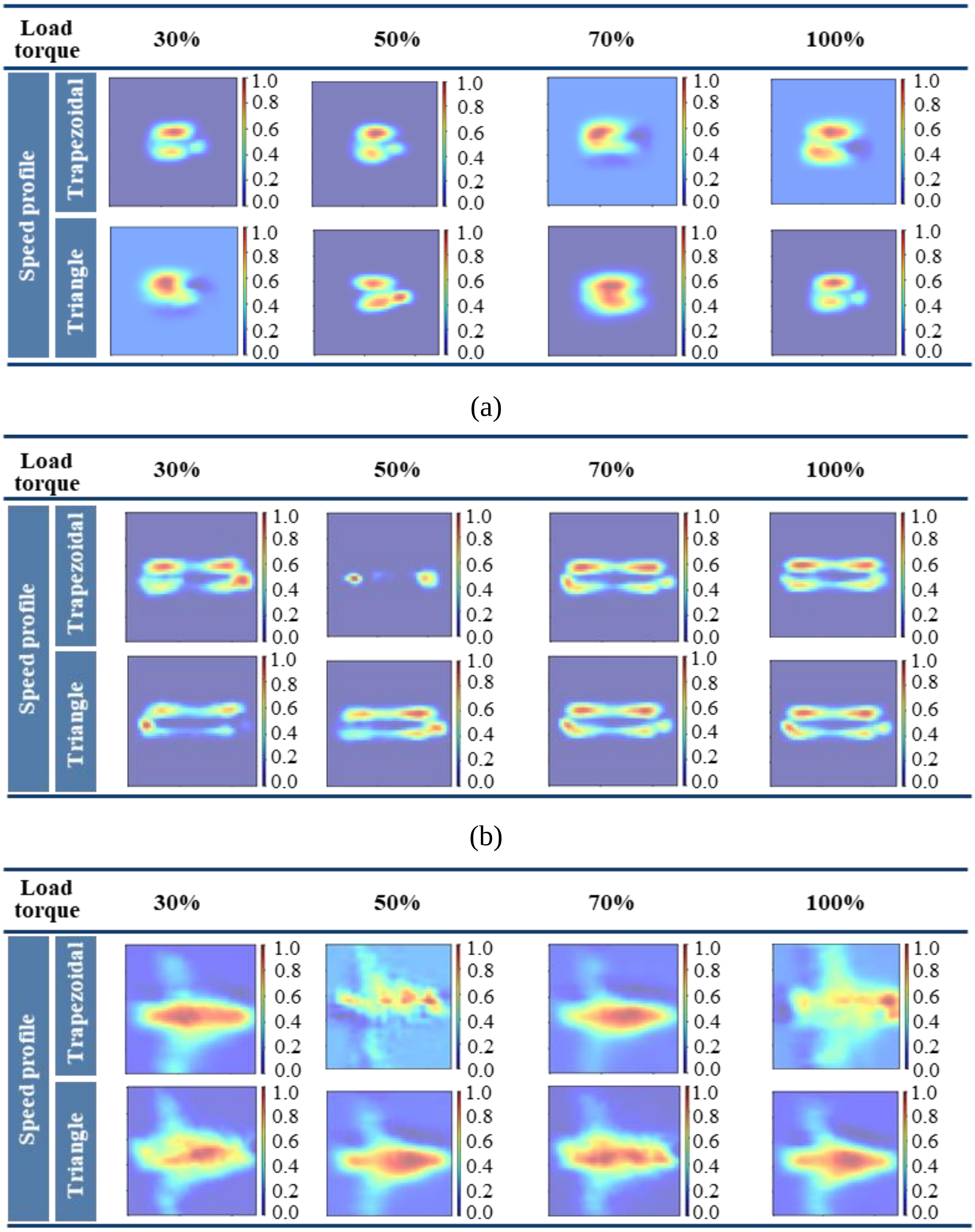

(a)

(b)

(c)

Figure 5-6 GradCAM result of CONV0 layer in the CNN model using test dataset: (a) Normal, (b) Stator inter-turn short and (c) Misalignment

5.3.3 Comparative Analysis

To demonstrate the superiority of the proposed ICRM for CNN-based fault diagnosis, it was compared by other methods that generate the input image, including a TFR-based image (i.e., spectrogram using STFT, window size 64, overlap 0.5), two image-encoding techniques (i.e., GAF and MTF) and a stacked matrix. As the first comparative analysis, GAF, MTF, and the stacked matrix were configured with the raw current signal. In Figure 5-7, the average accuracy of the fault diagnosis with standard deviation bars, where the results are displayed on top of the bar chart; each accuracy was calculated with 10 repetitions. For every case, the fault diagnosis accuracy when ICRM was provided as input in the same CNN model outperformed than any other inputs. Since the TFR-based image contains the physical information (i.e. spectral component according to time), the performance with TFR-based image was better than the other image input using image-encoding techniques. The accuracy of image-encoding inputs varied greatly depending on which techniques was adopted, as shown at the accuracy of MTF and GAF in. A possible reason for the better result with MTF input than GAF can be inferred that the Markov transition matrix calculated by discrete stator currents was appropriate to abstract the characteristics of stator currents.

As can be seen in Figure 5-8, the performance of CNN-based fault diagnosis was evaluated for every input case using the test data under the other operating conditions that were not trained. As can be seen in Figure 5-8 and Table 5-3, the accuracy at which ICRM was used as the input image to the same CNN model was higher and its overall standard deviations were smaller than any other methods. It can be inferred that the CRs in ICRM exert an influence on the performance of CNN-based fault diagnosis for the surface-mounted PMSM. This is because all the other input images were configured with the raw current signal but ICRM was composed of the CRs that can capture the physical fault-related signatures of the motor stator current. Additionally, the TFR-based image showed the better performance than GAF, MTF, and the stacked matrix, as can be seen in Figure 5-8 (b). This can be attributed to the fact that GAF and MTF mainly extracted time-domain features; instead, TFR presented the spectral information with the time. In Figure 5-8 (a), on the other hand, TFR showed the lower performance than GAF, MTF, and the stack. The reason might be due to an excessive change in the current signal according to the speed profile variation. The effect of the speed profile variation in the current signal would be more remarkable in TFR, rather than GAF, MTF, and the stack, because the main frequency of the current signal is determined dominantly by the speed. On the other hand, the difference according to the operating conditions were obviously confirmed by which representatively shows the input image of normal state using GAF, MTF, respectively. In Figure 5-9, while all the images were normal state, they varied according to the operating conditions. Therefore, these results suggested that the effects of the variable operating conditions have to be suppressed to properly capture the fault-related characteristics.

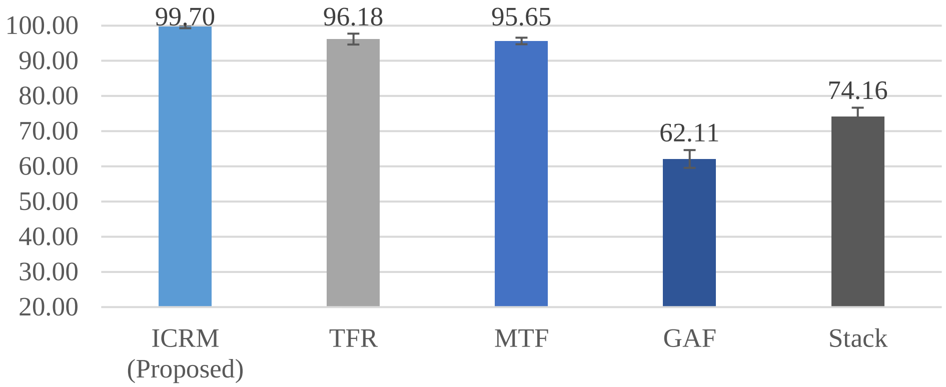

Figure 5-7 The fault diagnosis accuracy with comparative methods using raw current signal

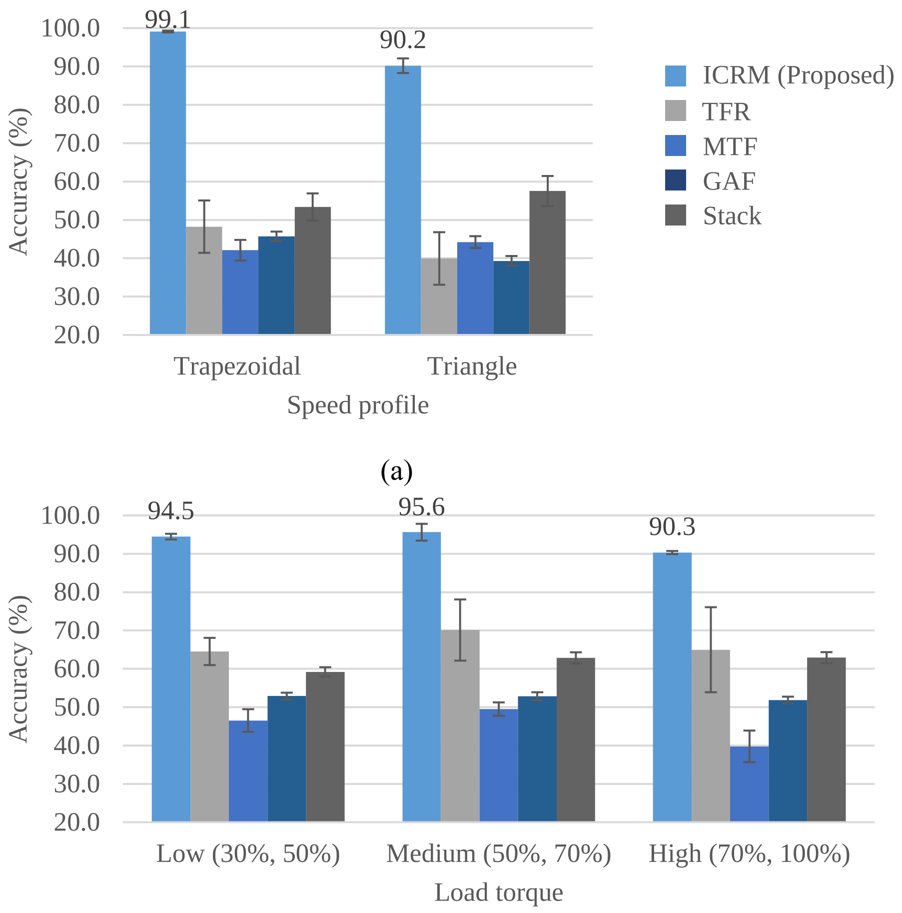

(a)

(b)

Figure 5-8 The fault diagnosis accuracy with comparative methods using raw current signals under testing different operating conditions: (a) speed profile and (b) load torque

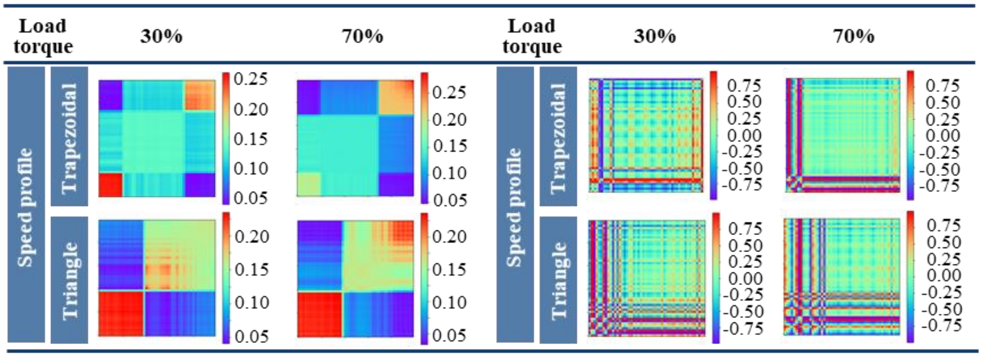

(a) (b)

Figure 5-9 Image encoding result of normal state using: (a) Markov transition field (MTF), (b) Gramian angular field (GAF)

As the second comparative study, GAF, MTF, and the stacked matrix generated the input image by converting E_R and P_R individually; for instance, GAF_E_R, GAF_P_R, MTF_E_R, MTF_P_R, Stack_E_R, and Stack_P_R. As can be seen in Figure 5-10, the performances of comparative methods which trained the inputs made by E_R and P_R were broadly better than those of comparative methods which trained the inputs made by raw data. Especially, the comparative methods that learned the input made by E_R were better than those that learned the input made with P_R. A possible reason for the superiority with E_R is that E_R is a more proactive and sensitive component to the health state than P_R. The comparative methods which trained the inputs made by E_R and P_R were also tested with the data under other operating conditions as shown in Figure 5-11. Compared to Figure 5-9, the performance was improved because the effects of operating conditions were suppressed in E_R and P_R.

The overall performance of ICRM was better than those of other image generation methods. As can be seen in Figure 5-11 (b), the accuracy of TFR_E_R was relatively high under different load torque conditions. The fault-related information in E_R tends to be included in the high-frequency region. This implies that it could be difficult to capture the fault-related signature, if one investigates E_R in only the time domain under the high load torque condition in which the amount of noise is large. In this respect, TFR_E_R seemed to perform well because the frequency part of TFR could present the high-frequency region of E_R obviously. It is worth pointing out that ICRM demonstrated superior performance under different speed profile conditions, as can be seen in Figure 5-11 (a). This implies that the combined use of E_R and P_R helps to provide the critical fault-related information under variable speed conditions. When the instantaneous phase reveals the signal characteristics under speed variations, P_R could play a role as a sensitive indicator to capture the fault-related irregularities of the current signal [102]. Therefore, it is suggested that the combined use of E_R and P_R in ICRM contributes to the better performance on fault diagnosis under different speed profile conditions.

In summary, the proposed ICRM showed outstanding performance for CNN-based fault diagnosis, even under various operating conditions that were not trained. Table 5-3 summarized the fault diagnosis accuracy with standard deviations under variable operating conditions, including the comparative methods with raw current signals, E_R and P_R, respectively. Further, the proposed method was able to determine that the CNN model learned reasonable features of CRs by visualizing the activated weights of the trained model. It is worth pointing out that ICRM is designed for giving physics-guided current characteristics to the 2D input image to the CNN model, which will serve as a benefit when the feasibility of ICRM is extended to other systems.

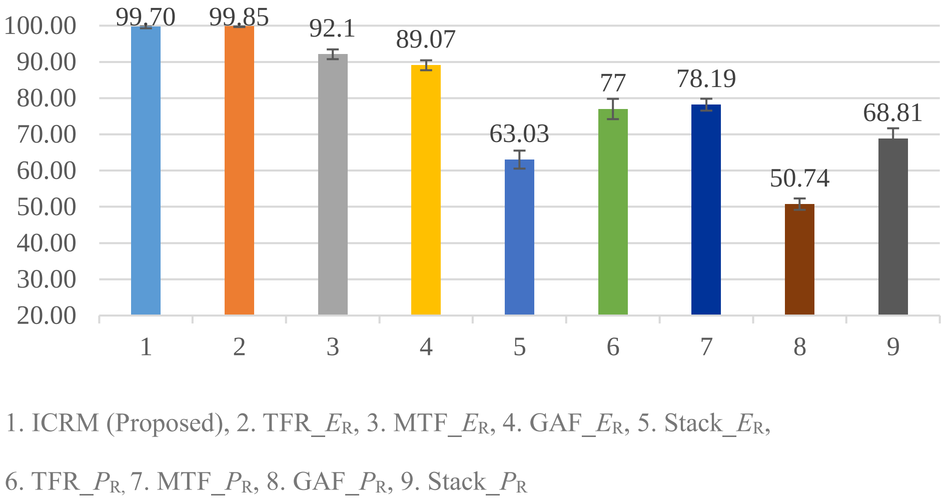

Figure 5-10 The fault diagnosis accuracy with comparative methods using E_R and P_R

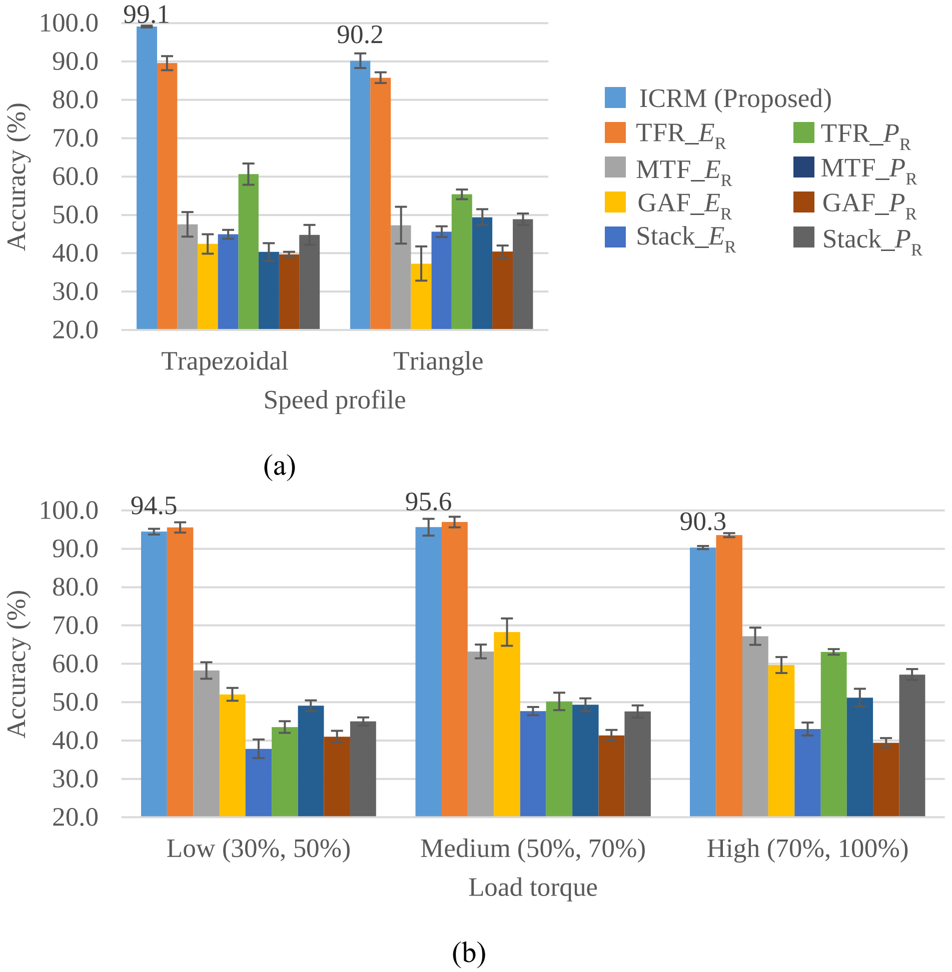

Figure 5-11 The fault diagnosis accuracy with comparative methods using E_R and P_R under testing different operating conditions: (a) speed profile and (b) load torque

Table 5-3 Fault diagnosis accuracy under variable operating conditions, including the comparative methods with raw data, E_R and P_R, respectively.

Input	Different operating conditions for test				
	Test different speed profile		Test different load torque		
	Trapezoidal	Triangle	Low (30%, 50%)	Medium (50, 70%)	High (70, 100%)
ICRM (Proposed)	99.1±0.2	90.2±1.9	94.5±0.7	95.6±2.2	90.3±0.4
TFR	48.2±6.8	40.0±6.9	64.5±3.6	70.1±8.0	65.0±11.1
MTF	42.1±2.7	44.2±1.5	46.5±3.0	49.5±1.8	39.8±4.1
GAF	45.7±1.2	39.3±1.3	52.9±0.9	52.8±1.1	51.9±0.9
Stack	53.4±3.6	57.5±3.9	59.2±1.2	62.9±1.5	62.9±1.4
TFR_E_R	89.6±1.8	85.8±1.4	95.6±1.3	96.9±1.4	93.5±0.5
MTF_E_R	47.5±3.2	47.3±4.8	58.3±2.2	63.2±1.8	67.2±2.2
GAF_E_R	42.4±2.5	37.3±4.5	52.0±1.7	68.3±3.6	59.7±2.1
Stack_E_R	44.9±1.2	45.6±1.4	37.9±2.4	47.7±1.1	43.0±1.7
TFR_P_R	60.6±2.8	55.4±1.3	43.5±1.5	50.2±2.3	63.1±0.7
MTF_P_R	40.3±2.3	49.4±2.1	49.1±1.4	49.3±1.7	51.2±2.3
GAF_P_R	39.7±0.7	40.4±1.6	41.0±1.6	41.3±1.4	39.4±1.2
Stack_P_R	44.8±2.6	48.9±1.5	45.0±1.1	47.6±1.6	57.2±1.4

5.4 Summary and Discussion

This section proposed a novel, instantaneous current residual map (ICRM) for convolutional neural network (CNN)-based fault diagnosis using motor stator current signals; this approach is applicable for variable operating conditions. The proposed ICRM approach consists of the set of the phase and envelop residuals, denoted by P_R and E_R, pairs extracted from the fault information from the instantaneous phase and amplitude, respectively, of the motor stator current. Using the proposed ICRM, a fault can be discerned by investigating the degree or shape of spreading of the scaled current residuals (CRs) in the ICRM, and precise fault diagnosis is available by making the CNN model learn the ICRM. Through the experimental study that examined the surface-mounted permanent magnet synchronous motor (PMSM), the proposed ICRM was confirmed to outperform the other image-encoding and TFR-based inputs when applied as the input to the CNN model for fault diagnosis, even under various operating conditions that were not trained. The primary benefits of the proposed method are that physics-informed CNN for fault diagnosis is available owing to putting the physical meaning of motor stator current signals to a 2D input image to a CNN model. Moreover, the ICRM is applicable under variable operating conditions, because the procedure of calculating P_R and E_R contains the repression of influences on the operating conditions. Future work can be conducted to improve the fault diagnosis method using the ICRM to be applied to a broad range of motor types and various operating conditions.

Chapter 6

Fault Severity Estimation with Feature Inherited Hierarchical Convolutional Neural Network (FI-HCNN)

6.1 Review of the Hierarchical Network for Fault Diagnosis

A hierarchical network consists of a parent and two or more child modules. In image classification, several hierarchical models have been proven effective by categorizing the superclass in the parent module and classifying the fine classes in the child modules. Figure 6-1 depicts the schematic of a hierarchical network, where the total number of classes is N_1+ N_2+…+N_k; these can be categorized into k superclasses. For example, when the superclasses are set to “animal” and “building” the possible fine classes could include “cat” and “dog” for the former, and “schools” and “hospitals” for the latter. In the field of computer vision, several studies have developed algorithms to construct appropriate superclasses and classify images. In [30], the tree-based priors encouraged transfer of the input to the related classes. The hierarchical exclusive graphs in [31] classified the large-scale objects with theoretical interpretations. In [32], the algorithm was able to pretrain the fine classes

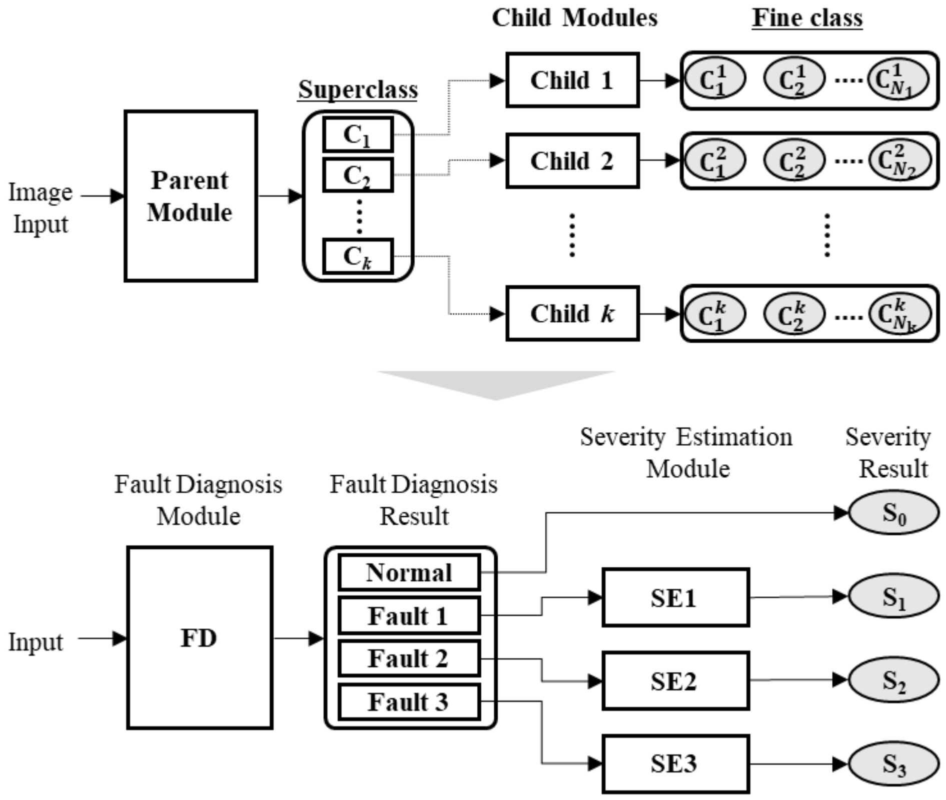

Figure 6-1 The schematic of a hierarchical neural network for fault diagnosis

independently by using a combination of shared low-level features and additional input.

6.2 The Proposed FI-HCNN Method

This section details the proposed feature inherited hierarchical CNN (FI-HCNN) method. First, the special connected architecture of the hierarchical learning model is explained and the overall hierarchical structure, which consists of an FD module and several SE modules, is described.

6.2.1 Feature Inheritance Architecture

When the hierarchical network is applied for machinery health monitoring, the parent module can be matched to FD, and the child modules matched to SE for each fault mode. When the FD module and SE modules are deployed in the hierarchy, they reflect two different objectives, respectively: first, classifying a particular fault mode and then estimating its severity. In contrast to the ordinary hierarchical architecture, the proposed FI-HCNN delivers the latent features $\hat{\mathbf{t}}$ from the FD to the SE module. This concept is called *feature inheritance*. As shown in Figure 6-2, the input data $\mathbf{x}$ evolves into learned representations that contain rich characteristics for the particular fault mode (C_k) in the FD module. These representations refer to $\hat{\mathbf{t}}$. $\hat{\mathbf{t}}$ are used as the input to the SE module of C_k; they are learned to be regressed to the severity of C_k (S_{C_k}) through C_k's SE module.

Specifically, $\hat{\mathbf{t}}$ are the values calculated from the last pooling layer in the FD module. When the filters of the FD module are trained to highlight the characteristics of the fault based on the input data, $\hat{\mathbf{t}}$ – by passing through these filters – they are expected to develop into the features that contain significant and intensive abstractions about the particular fault mode. By extending without discarding $\hat{\mathbf{t}}$, the learning of the SE modules can be more focused on capturing higher-level features; this can support the regression of fault severity. Therefore, the transmission of $\hat{\mathbf{t}}$ helps learn the degree of a specific fault and leads to enhanced SE performance.

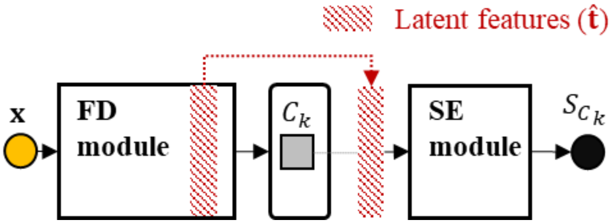

Figure 6-2 The concept of feature inheritance

6.2.2 A Hierarchical Structure for Fault Diagnosis and Severity Estimation

Using feature inheritance, which is the key idea of FI-HCNN, the overall hierarchical structure is configured as shown in Figure 6-3. The proposed FI-HCNN method consists of three parts: 1) preprocessing, 2) fault diagnosis, and 3) severity estimation. Each fault mode has its own SE module, while the normal state does not go through any additional modules. $\mathbf{x}$ denotes the pre-processed current data, $\hat{\mathbf{t}}$ signifies the latent features, $\mathbf{W}_{\mathbf{FD}}$ and $\mathbf{W}_{\mathbf{SE}}$ are the weight matrices of the FD and SE modules, respectively, C is the fault mode, and S is the severity of each fault mode. The severity ranges from 0 to 1.

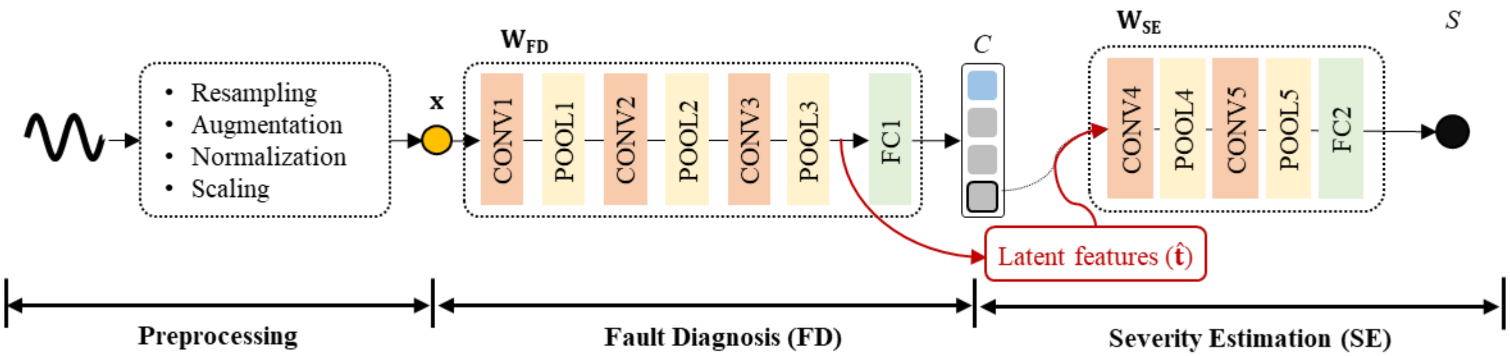

Figure 6-3 The schematic of the proposed FI-HCNN method

6.2.2.1. Part 1: Preprocessing

Before the hierarchical network starts learning, four steps of preprocessing (resampling, augmentation, normalization, and scaling) are executed on the raw current signals. First, the resampling adjusts all data by interpolation to have the same amount of information under the same operating conditions; this makes each datum unit have the same points in a revolution. Second, data augmentation is conducted by overlapping the amount of data of one revolution. This augmentation, which conserves the periodic characteristic of the current signal, not only has a positive effect on performance, it can also help the filters in the model to learn the relevant features. Third, normalization, which subtracts the self-mean and divides the total standard deviation, is used to homogenize the data of each experiment. Finally, the amplitudes of the current signals are scaled from -1 to 1. The scaling of current signals allows expandability to signals from different sized motors and a decrement in the uncertain effects of the load torque condition.

6.2.2.2. Part 2: Fault Diagnosis (FD)

After preprocessing, the refined current data enters the FD module. The FD module consists of three convolution layers, max-pooling layers, and one FC layer. Through the three convolution and max-pooling layers, the input data can be formulated as the features that reveal the fault characteristics. The FC layer is learned to classify the features to the fault mode. The task of the FD module can be explained as $p\left(\hat{C}\middle|\mathbf{x},\mathbf{W_{FD}}\right)\sim p(C|\mathbf{x})$. The optimum can be achieved by minimizing the loss of the FD module (L_{FD}), given as:

$$L_{\mathrm{FD}}(\mathbf{W_{FD}}) = \beta_1 \|\mathbf{W_{FD}}\|^2 - E_{\hat{C}\sim p_{data}} \log p\left(\hat{C} \middle| \mathbf{x}, \mathbf{W_{FD}}\right) \tag{6.1}$$

where β_1 is a coefficient of the L2-normalization and the loss is computed via cross-entropy; this is because the FD module tackles the problem of discrete classification. While the dimensions of the features decrease as they pass through the pooling layers, the number of features increases due to the increased filters as the layer becomes deeper. In addition, ELU activation is used in all convolutional layers to encourage the information under 0 to be conserved; this is defined as:

$$f(x) = \begin{cases} x \ (x \geq 0) \\ \exp(x) - 1 \ (x < 0) \end{cases} \tag{6.2}$$

Both the ELU activation function and the increase in the number of filters according to the layer depth can compensate for the possibility of information that may be lost due to the stacked layers. As the weights of the filters are updated in the direction of minimizing (1), the input data passing through the updated filters formulates the features distinguishable to the fault modes. The features just before being flattened, which are denoted as $\hat{\mathbf{t}}$ in, are then transferred to the subsequent SE module.

6.2.2.3. Part 3: Severity Estimation (SE)

An SE module for each fault mode learns the severity of each corresponding fault mode. Each SE module consists of two convolution layers, followed by max-pooling layers and one FC layer. The two convolutional layers of the SE module, which have a larger number of filters than the preceding FD module, extract the more sophisticated features associated with the fault severity. The elaborate features are flattened and computed with the FC layer and then regressed to determine the fault severity. The task of an SE module can be explained as $p\left(\hat{S} \middle| \hat{\mathbf{t}}, \mathbf{W_{SE}}\right) \sim p(S|\mathbf{x})$. The latent features $\hat{\mathbf{t}}$, provide significant information about the corresponding fault mode to the SE module when L_{FD} is sufficiently decreased. Then, $\hat{\mathbf{t}}$ are used to learn the $\mathbf{W}_{\mathbf{SE}}$ of the SE model by transferring the information to the SE module of the corresponding fault mode. The delivery of $\hat{\mathbf{t}}$ is expected to concentrate on learning the specific characteristics to assess the severity of each fault by minimizing the loss of the SE module (L_{SE}), described as:

$$L_{\mathrm{SE}}(\mathbf{C}) = \beta_2 \|\mathbf{W}_{\mathbf{SE}}\|^2 + \frac{1}{2} E_{\hat{s}\sim p_{data}} \left\|\hat{S} - f_2(\hat{\mathbf{t}}, \mathbf{W}_{\mathbf{SE}})\right\|^2 \tag{6.3}$$

where β_2 denotes a coefficient of L2 normalization and f_2 is the estimated severity, as calculated from latent feature $\hat{\mathbf{t}}$ and $\mathbf{W}_{\mathbf{SE}}$ of an SE module. Since fault severity is the continuous variable, the loss is computed by mean squared error (MSE).

The hierarchical structure of the proposed method is illustrated in detail in Fig. The FD module used to identify the fault mode and three SE modules for assessing the fault severity are hierarchically associated. The numbers in square brackets indicate the dimensions of the data passed through the layer. The numbers in parentheses refer to the number of filters, and the size of the filters is set to nine for all convolution layers. The pooling size is set to four for all pooling layers. The structure of the proposed FI-HCNN is designed based on the motor current signals described in this study, but it can be generally applied with minor adjustments depending on the amount and the type of data. In Figure 6-4, the blue arrow represents an example flow of a test data sample. When the test data is classified as *Fault* 1, the latent features of the test data transfer to the SE module of *Fault* 1 and develop into features that indicate the severity of *Fault* 1.

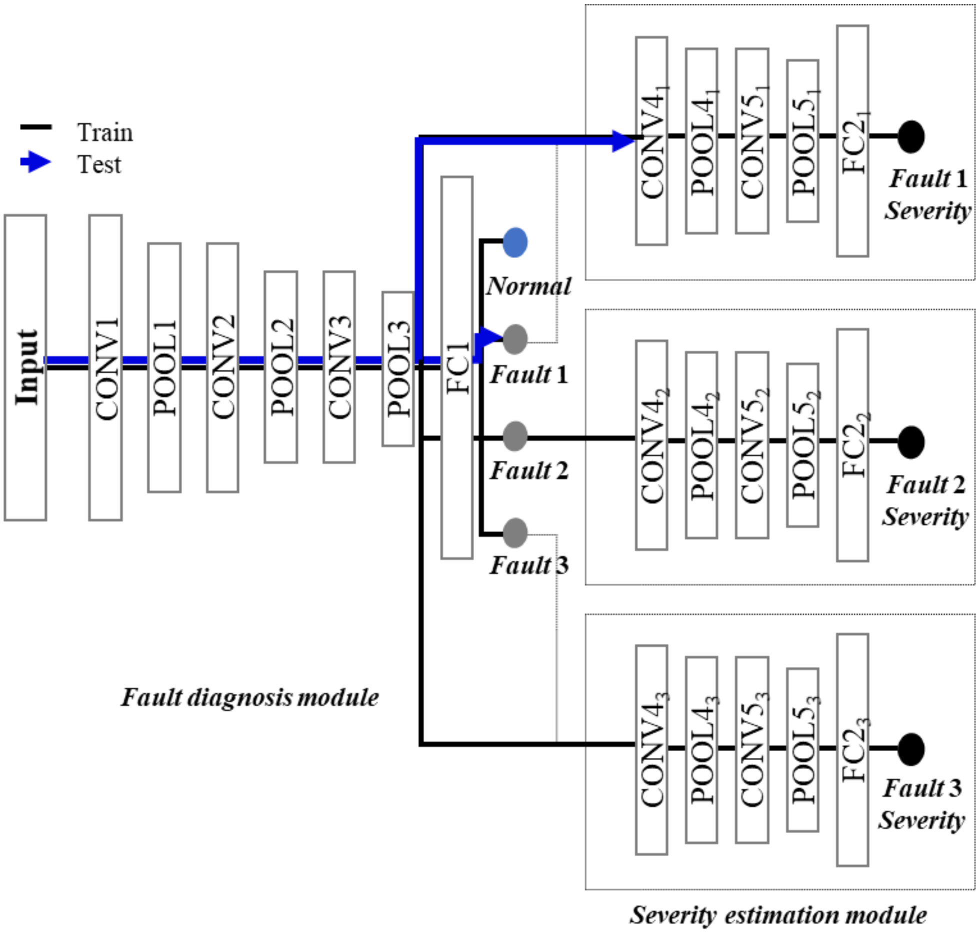

Figure 6-4 The structure of the proposed FI-HCNN method

6.3 Case Studies

In this section, the proposed FI-HCNN method is validated using experimental data. There are two case studies; first, the experimental After an explanation of the data, the results of the proposed FI-HCNN are discussed. Then, the performance of FI-HCNN is compared to that of traditional MCSA methods and other DL methods, of which the structures are related to the proposed FI-HCNN.

6.3.1 Case Study 1: Stationary Condition

6.3.1.1. Data Description

First, the dataset acquired under stationary condition is described. A dataset from a 160kW, 2-pole induction motor was used to analyze the performance of the proposed method. In the experiment, one phase of the stator current signal was acquired at 3600 revolutions per minute (RPM) with no load. There were a total of three mechanical faults with multiple severity levels, respectively: eccentricity, unbalance, and a broken rotor bar. These faults and severity levels are illustrated in Figure 6-5. The severity was defined based on the degree of experimental settings that caused the severe conditions of the motor. A higher severity level means that the health state of a motor is more deteriorated. Eccentricity, which indicates an uneven air gap between the rotor and stator, was introduced at three different levels by moving the rotor 10%, 30%, and 50% of the original air-gap length from the center. The severity of eccentricity was denoted as 10%, 30%, and 50%. For example, 30% eccentricity is described in Figure 6-5 (a). The broken rotor bar, which was emulated by drilling rotor slots to create a half and a whole break, had the severity of 50% and 100%,

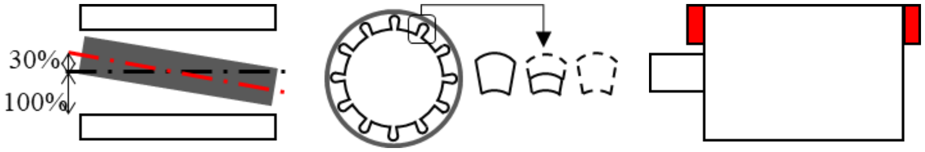

(a) (b) (c)

Figure 6-5 The illustration of mechanical motor faults: (a) eccentricity, (b) broken rotor bar, and (c) unbalance

respectively. Unbalance was created by attaching weights to the rotor. According to ISO21940-11, the health state is balanced at a vibration of 2.5 mm/s, marked as G2.5; G40 is treated as a failure. The severity of unbalance was set to the ratio of the unbalance level, 16% and 40%; these values indicate G6.3 and G16, respectively. All specific conditions, such as the severity level and abbreviations used, are shown in Table 6-1. Figure 6-6 shows an example of raw stator current signals from each health state. The magnitudes at 60Hz and its harmonics were large in the frequency domain (see Figure 6-6 (b)) because the supply frequency and the rotating frequency were the same. Although the current signals of the ROTOR stood out, as the broken rotor bar itself highly affected the motor compared to other fault modes, the current signals of each health state (except those of the broken rotor bar) were not readily distinguishable in either the time- or frequency-domain.

Table 6-1 Description of motor health states

Class	States	Abbreviation	Severity
1	Normal	NOR	0
2	Eccentricity	ECC	0.50/0.30/0.10
3	Broken rotor bar	ROTOR	1.00/0.50
4	Unbalance	UNB	0.40/0.16

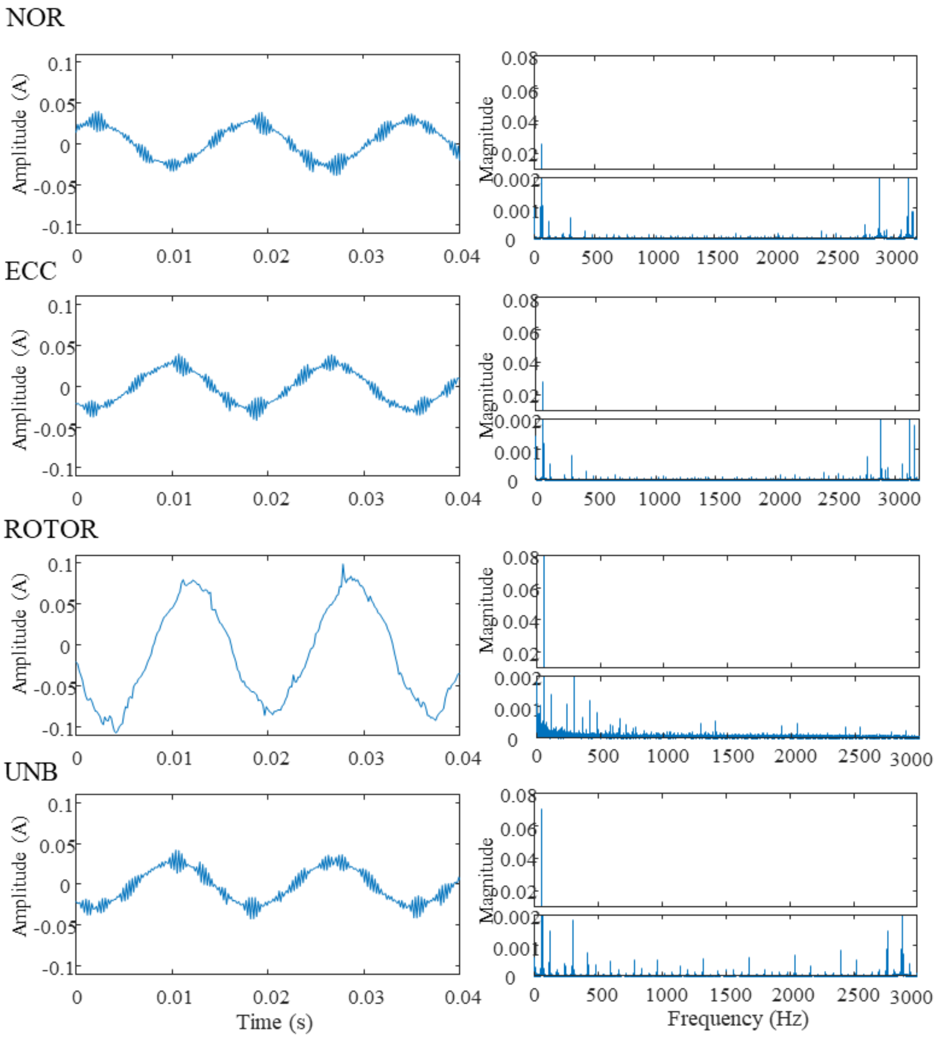

(a) (b)

Figure 6-6 Example of raw stator current signals from each health state: (a) time domain, (b) frequency domain

6.3.1.2. Result of FI-HCNN

Since FI-HCNN solves a classification problem in the FD module and a regression problem in the SE modules, the accuracy of FI-HCNN is defined separately for each module. In the case of the FD module, the error is calculated as the summation of the incorrect samples divided by the number of total samples. Then, the accuracy is calculated by subtracting the error from one. The accuracy of each SE module is evaluated by calculating the root mean squared error (RMSE) between the prediction and actual fault severity. For example, 2% of RMSE means that the fault severity deviates by an average of 2% from the true severity. All of the methods examined in Section are evaluated with this metric.

For preprocessing, all raw stator current signals were resampled at 120 points per revolution, and one sample was defined to include two revolutions and augmented with one revolution overlapped. The length of each sample was 240. Normalization and scaling were then conducted in sequence. The total number of data in the set was 3776, as each class has 472 data. The network was trained using 75% of the data set and tested with the remaining 25% of the data set. 4-fold cross-validation was conducted. The entire training and test procedure were run 10 times with randomly selected data sets to study repeatability by investigating a 95% confidence interval. The model parameters of FI-HCNN architecture, as shown in Figure 6-4, were described in Table 6-2. The specific information of the FI-HCNN architecture according to the pre-processed input data was summarized in

Table 6-3. The other hyper-parameters, which are adaptive to learn the modules using the given data sets, are detailed in Table 6-4. The variables of the SE modules were determined to be smaller because the subsequent SE modules conduct elaborate training with the down-scaled data set.

Table 6-2 The model parameters for FI-HCNN architecture

Layer	Abbreviation	Parameter
Convolutional layer	CONV1	kernel size: 9, number of filters: 6, stride: 1, padding: 4
	CONV2, CONV3	kernel size: 9, number of filters: 16, stride: 1, padding: 5
	CONV4, CONV5	kernel size: 9, number of filters: 32, stride: 1, padding: 5
Max pooling layer	POOL1 ~ POOL5	None
Fully connected layer	FC1	Node: 500
	FC2	Node: 400

Table 6-3 The specific information of FI-HCNN architecture

FD module	Output shape	Number of parameters
Input	[1x240]	
CONV1	[6x240]	60
CONV2	[16x120]	880
CONV3	[16x60]	2,320
FC1	[500x4]	242504
Total		245,764
SE module	**Output shape**	**Number of parameters**
Input	[32x30]	
CONV4	[32x15]	4,640
CONV5	[32x7]	9,248
FC2	[400x1]	90,401
Total		104,289

Table 6-4 Hyperparameters for training FI-HCNN

Module	Learning rate	Batch size	Epoch	Drop out	L2-norm coefficient
FD	0.001	500	3000	0.7	0.001
SE	0.0001	50	3000	0.7	0.0001

The test accuracy of the FD module was 99.70±0.11 % and the three faults were distinguishable, as shown in (a). The false negative error of ECC was understandable because – as compared to other fault modes, such as a broken rotor bar – the influence of an ECC-related fault in the current signal can be weak at first [103]. Thus, it is probable that an ECC might be determined to normal at the incipient stage because the effect of an incipient ECC on the current signal is small. The FD performance can be confirmed by investigating the latent feature space, as shown in Figure 6-8 The test data set was used to demonstrate the latent feature spaces of each pooling layer in the FD module. The latent space of POOL3 (Figure 6-8 (c)), which is $\hat{\mathbf{t}}$, had more condensed clusters, compared to that of POOL1 and POOL2 (Figure 6-8 (a) and Figure 6-8 (b), respectively). In Figure 6-8 (c), the NOR was formulated into one cluster, and the other health states appeared to be more distinguishable. The performance of each SE module was evaluated using RMSE; 0.61±0.05% for ECC, 0.54±0.05% for ROTOR, and 0.65±0.04% for UNB, respectively (Table 6-5). The learning feasibility of the SE module was confirmed by analyzing the change of the estimation result depending on the loss. For example, the trend of the loss and its SE results are demonstrated in the case of UNB in Figure 6-9. While the bias and variance error of the FI-HCNN method showed improvement in the final output, the errors remained in the common hierarchical model in which the input was used repetitively. Moreover, the RMSE result of FI-HCNN in the early stage of SE was smaller than that of the comparative HCNN, which reuses the raw data; this shows the effect of latent features in SE. These RMSE results are discussed more specifically in the following subsection by comparing them with the results derived from other methods.

Table 6-5 Summary of results for FD and SE using FI-HCNN, spectral feature-based, and PCA feature-based methods at stationary condition

Methods	FD Accuracy [%]	SE RMSE [%]		
		ECC	ROTOR	UNB
FI-HCNN (Proposed)	99.70±0.11	0.61±0.05	0.54±0.05	0.65±0.04
Spectral features (Physics-based)	97.22±0.20	6.63±0.14	3.11±0.06	5.64±0.09
PCA features (Data-driven)	97.39±0.22	5.39±0.07	2.97±0.06	5.43±0.11

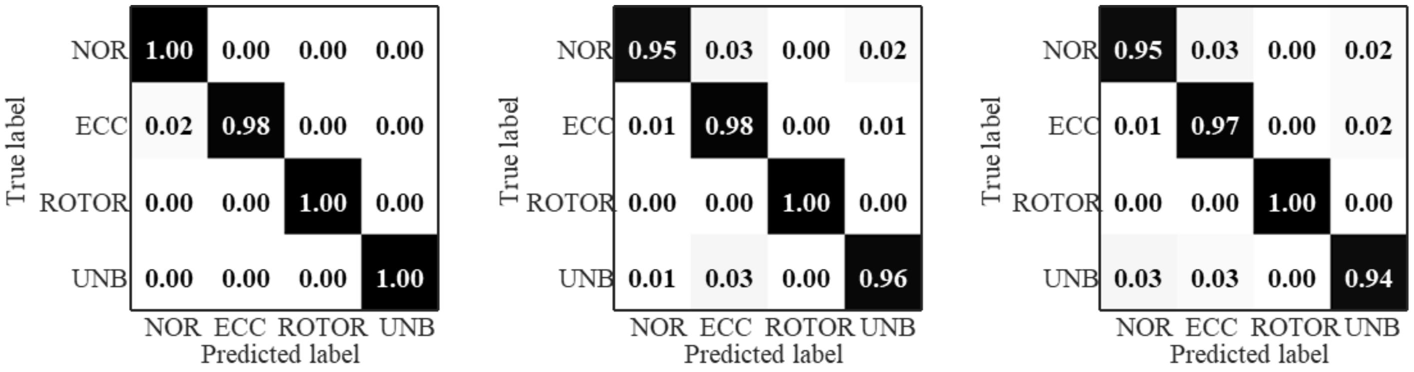

(a) (b) (c)

Figure 6-7 Comparison of a confusion matrix of FD modules: (a) FI-HCNN method (b) spectral features-based method, and (c) the principal components-based method

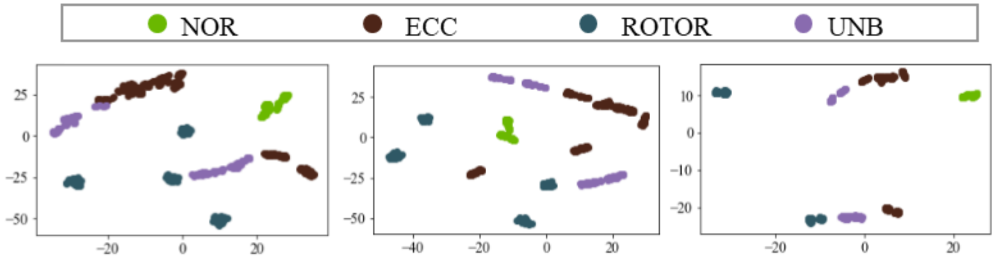

(a) (b) (c)

Figure 6-8 The latent feature spaces of each health state using t-SNE with respect to the test data: (a) after POOL1, (b) after POOL2, and (c) after POOL3

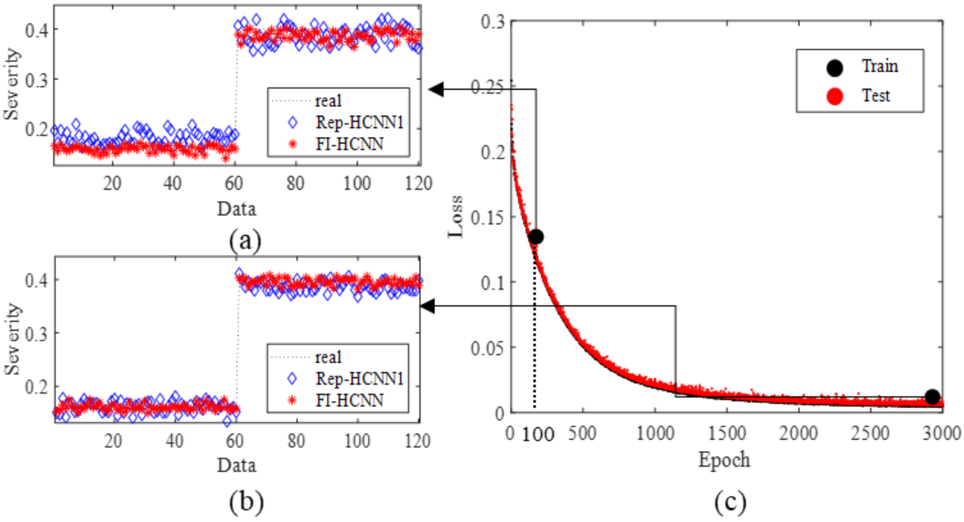

(a)

(b)

(c)

Figure 6-9 The example of UNB SE result, depending on the loss: (a) RMSE early stage test result, (b) RMSE final stage test result, (c) loss

6.3.1.3. Comparison with Conventional Methods

This section aims to investigate the performance of FI-HCNN, as compared to existing methods. Two studies were conducted to represent conventional MCSA methods; one was based on physics-based spectral features, the other was based on data-driven features computed with principal component analysis (PCA) of the magnitude of fast Fourier transform (FFT). The spectral features that were developed separately for each fault mode through theoretical analysis are summarized in Figure 6-11; these results are based on [104], [105]. n_b is the number of rotor bars, s is the slip, p is the number of pole pairs, f_s is the supplied frequency, f_r is the rotating frequency, n and λ are positive integers, and ζ is the arbitrary odd number. For the data-driven features, the principal components (PCs) of the FFT magnitudes are calculated. Instead of selecting the specific FFT magnitudes based on domain knowledge, PCA reduced the original FFT magnitude set (consisting of 120 data points), to a 22 PC set with 99% explained variance. After extracting the features using both physics and data-driven methods, the features were fed into SVM for FD and into support vector regression (SVR) for SE in common. The SVM and SVR methods both use quadratic polynomial kernels. The results of these two methods are summarized in Table 6-5. FI-HCNN shows about 2% better FD accuracy than other methods. As shown in Figure 6-7, both conventional methods had more false alarms that indicate normal to faulty. In addition, the RMSEs of SE using the conventional methods were about 10 times worse than those of FI-HCNN, as shown in Figure 6-10.

Table 6-6 The spectral features of induction motors based on MCSA

Fault mode	Spectral feature	Details
Eccentricity	$f_{\mathrm{ecc,SE(DE)}} = \left(\frac{\lambda n_b \pm n_d}{p}(1-s) \pm \zeta\right) f_s$	Static / Dynamic (n_d=0 / n_d=1,2)
	$f_{\mathrm{mix}} = f_s \pm n f_r$	Static+ Dynamic
Broken rotor bar	$f_{\mathrm{rbb}} = (1 \pm 2s) f_s$	Low-frequency range
	$f_{\mathrm{rbb}} = \left(\frac{n}{p}(1-s) \pm s\right) f_s$	High-frequency range
Unbalance	$f_{unb} = f_s \pm f_r$	

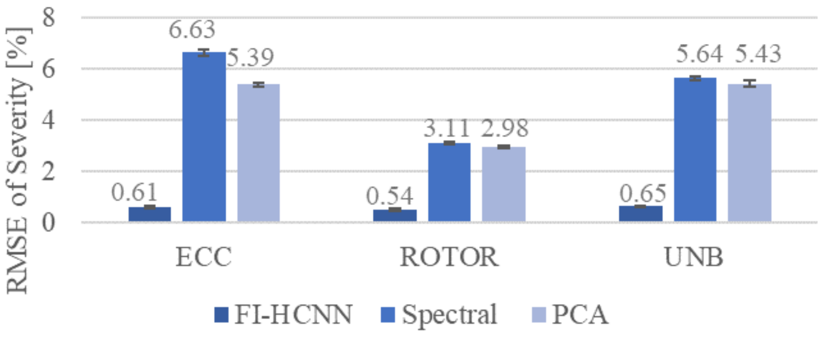

Figure 6-10 Bar chart comparing SE results using FI-HCNN and the conventional methods at stationary conditions

Specifically, the reason for the low performance of both conventional methods can be described in terms of the extracted features; these features do not demonstrate the apparent trends of fault deterioration. In fact, the spectral features were overlapped, depending on the parameters, even though they are defined separately. For example, the similarity between eccentricity and other mechanical faults, such as a bearing inner race fault and a broken rotor bar [8], [9] are revealed. Therefore, it is hard to declare that one spectral feature reflects only the effect of a particular fault mode. This is because the three fault modes (ECC, ROTOR, and UNB) share the relative characteristics that belong to mechanical failure and affect each other. Figure 6-11 shows the fault characteristic frequencies under a 3600RPM constant-speed condition. Most frequencies were overlapped because the supply frequency was the same as the rotating frequency and there was no slip at the constant-speed condition. Figure 6-12 shows some spectral features labeled by the fault modes; the number next to each fault mode refers to the fault severity. It is difficult to readily discriminate the fault modes and their severity because a significant amount of the feature values were overlapped. Also, the two main PCs of the FFT magnitudes are plotted in Figure 6-13. The PCs of faults (except UNB) are hard to distinguish from NOR, and the overlap of PCs between severities interrupts the distinction in each of the fault cases. The weak performance of the conventional features thus yields inadequate results. Compared to conventional features, FI-HCNN is capable of learning the enhanced features to adapt and estimate the fault severity, thereby arriving at improved results, as shown in Figure 6-14.

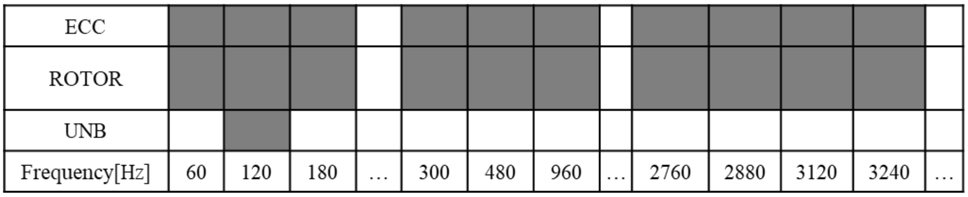

ECC	■	■	■		■	■	■		■	■	■	■	
ROTOR	■	■	■		■	■	■		■	■	■	■	
UNB		■											
Frequency[Hz]	60	120	180	…	300	480	960	…	2760	2880	3120	3240	…

Figure 6-11 Fault characteristic frequency under 60Hz constant speed condition

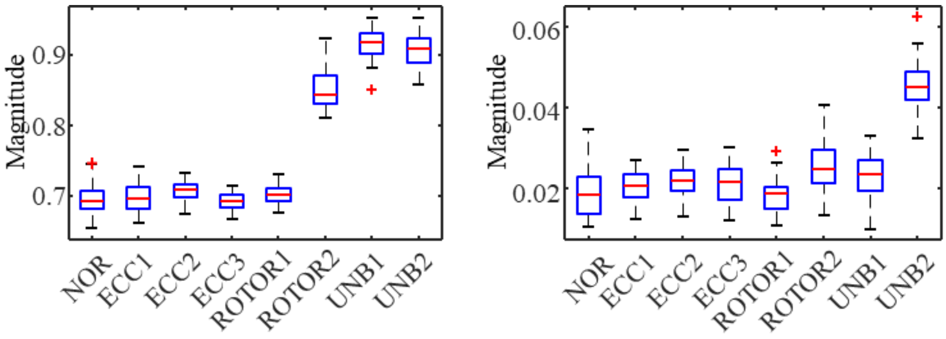

(a) (b)

Figure 6-12 Comparison of spectral features according to the fault modes: (a) is the FFT magnitude at 60 Hz, indicating ECC and ROTOR faults, and (b) is the FFT magnitude at 300Hz, indicating all of the fault modes

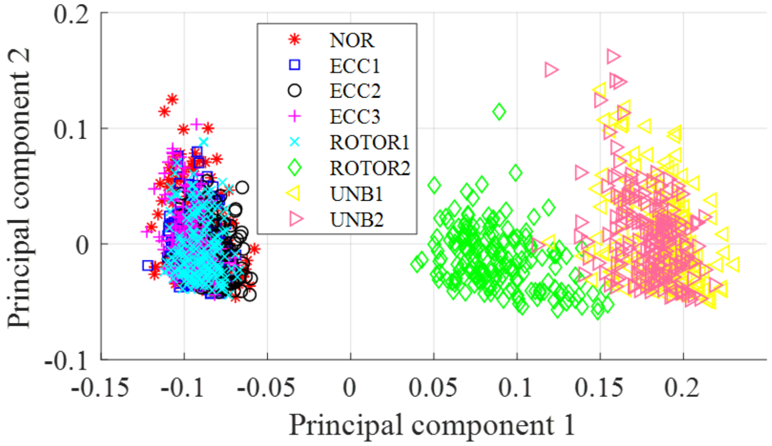

Figure 6-13 The results of principal component analysis using the FFT magnitude of the stator current signals

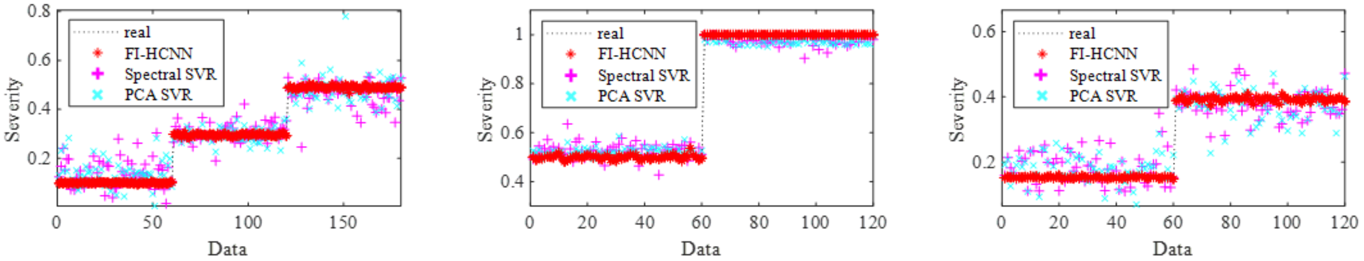

(a) (b) (c)

Figure 6-14 Comparison of SE results using FI-HCNN and the conventional methods at stationary condition: (a) ECC, (b) ROTOR, and (c) UNB

Then, the performance of the FI-HCNN was confirmed by comparing it with other HCNN architectures. Two concept models were constructed with HCNN with a repetitive hierarchical structure in which the input data is re-used in the child modules based on previous research [106]–[108]. The structures of all of the comparative HCNN models are described in Figure 6-15. Figure 6-15 (a) is the proposed FI-HCNN. Figure 6-15 (b) is one of the repetitive HCNN (Rep-HCNN1) models. where the child modules are modified from the parent module. The child modules of Rep-HCNN1 have the same structure as that of FI-HCNN. Figure 6-15 (c) is the other repetitive HCNN (Rep-HCNN2), where the structure of the parent module and the child module are identical; as outlined in [107], [108]. The notations in Figure 6-15 are the same as those in Figure 6-3. The hyper-parameters (e.g., learning rate, batch size, drop-out rate, and L2-norm coefficient) were set equal to the values used in FI-HCNN; however, the epoch was adjusted to a value at which the model could be trained sufficiently.

The SE results of all of the comparative methods using the above models are summarized in Table 6-7; FI-HCNN showed the best performance among all results. The RMSEs of all of the fault conditions using FI-HCNN were about half of those observed for the other HCNN methods, as shown in Figure 6-16. We can also confirm that FI-HCNN has a lower variance error compared to both Rep-HCNN1 and 2, as shown in Figure 6-17.

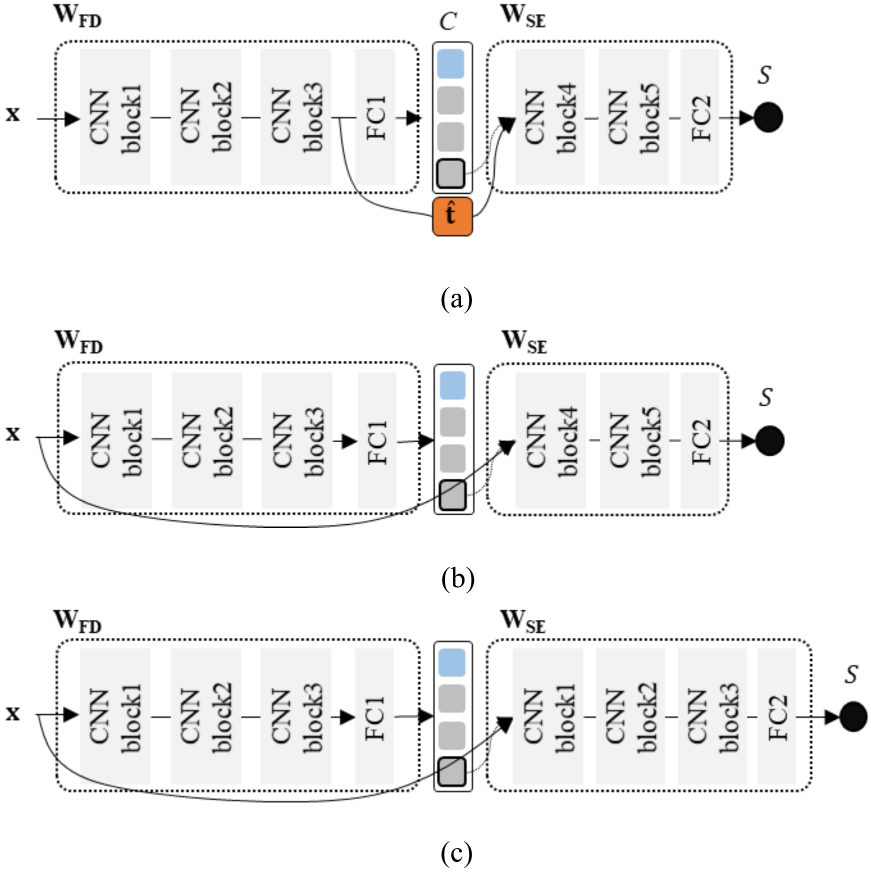

Figure 6-15 The structures of comparison in the HCNN models: (a) FI-HCNN, (b) Rep-HCNN1, and (c) Rep-HCNN2

Table 6-7 Summary results of SE using FI-HCNN and other HCNN methods at stationary condition

Methods	SE RMSE [%]		
	ECC	ROTOR	UNB
FI-HCNN (Proposed)	0.61±0.05	0.54±0.05	0.65±0.04
Rep-HCNN1	1.41±0.10	1.08±0.07	1.13±0.09
Rep-HCNN2	1.17±0.08	0.71±0.05	1.05±0.05

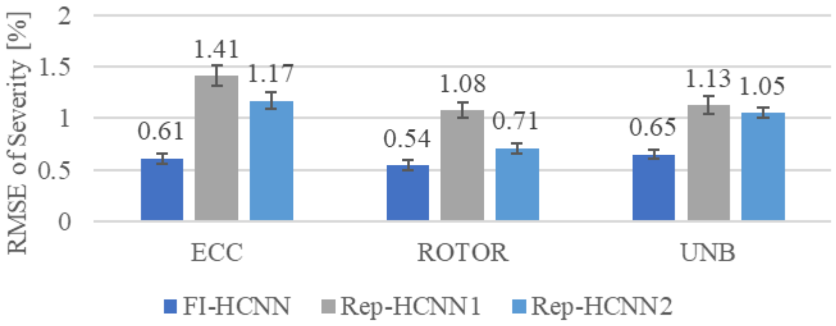

Figure 6-16 Bar chart comparing SE results using FI-HCNN and the other hierarchical CNN methods in stationary condition

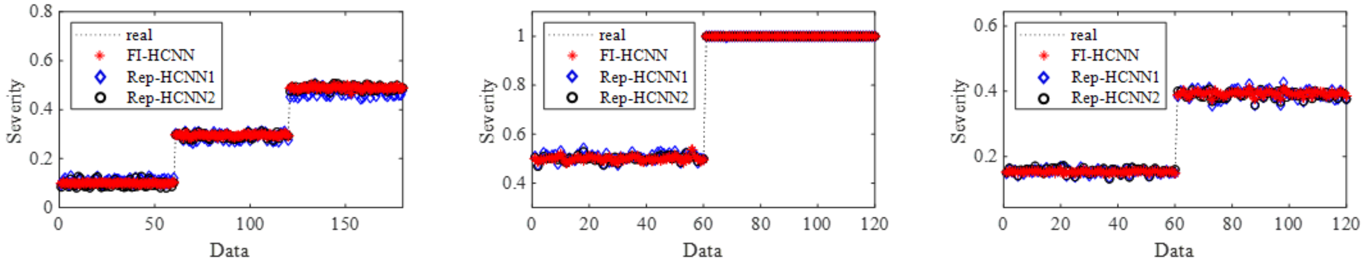

(a) (b) (c)

Figure 6-17 Comparison of SE results using FI-HCNN and the repetitive HCNN methods in stationary condition: (a) ECC, (b) ROTOR, and (c) UNB

To be specific, the superior results of FI-HCNN, as compared to Rep-HCNN1, support the idea that the propagation of the latent features is effective to enhance SE. The structures of Rep-HCNN1 and Rep-HCNN2, which receive the raw input data in common, have different filter designs; Rep-HCNN1 extracts lots of features at the beginning, while Rep-HCNN2 extracts an increasing number of features through stacked layers. A possible reason for the slight improvement in Rep-HCNN2, as compared to Rep-HCNN1, is that the gradual learning by the stacked layers is more effective for training the raw input data. Through these comparative studies, we can confirm that the pre-trained latent features that learn the characteristics of the fault mode result in positive effects in the SE modules. There is also abundant room for further progress, by examining additional data in various fault conditions.

6.3.2 Case Study 2: Variable Operating Condition

To investigate the effectiveness of the proposed FI-HCNN under variable operating conditions, the dataset which was described in Chapter 3 was used. Figure 6-18 shows the architecture of FI-HCNN using ICRM as input. The model parameters of the FI-HCNN with ICRM input architecture were described in Table 6-8 and the specific information according to the ICRM input was summarized in Table 6-9. For comparative methods, two repetitive HCNN models were adopted, similarly to Figure 6-15, which were illustrated in Figure 6-19. Since the physics-based or data-driven feature extraction is difficult without proper pre-processing of reducing the effect of variable operating conditions, the repetitive HCNN models were only compared in this case study. The accuracy of fault diagnosis was 98.93±0.82 % in

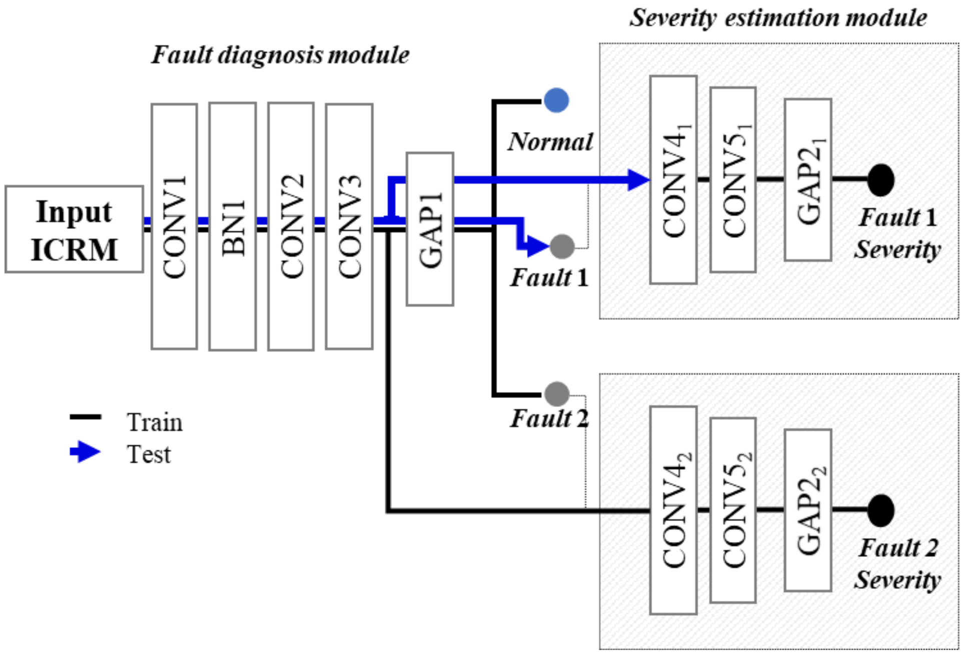

Figure 6-18 The structure of the FI-HCNN using ICRM as input

common, because the fault diagnosis module was the same for FI-HCNN and the two Rep-HCNN models. However, the RMSE of severity estimation showed a significant difference as described in Figure 6-20. The specific RMSE results of SE modules are summarized in Table 6-10. The RMSE of the proposed FI-HCNN was 4 times (SE module of stator inter turn short) and 3 times (SE module of misalignment) better than that of the other two Rep-HCNN models, respectively.

Table 6-8 Hyperparameters for the FI-HCNN using ICRM as input

Layer	Abbreviation	Parameter
Convolutional layer	CONV1, CONV2, CONV3	kernel size: 15, number of filters: 16, stride: 2, padding: 7
	CONV4, CONV5	kernel size: 5, number of filters: 16, stride: 2, padding: 2
Batch normalization layers	BN1	Momentum=0.1
Global average pooling	GAP1, GAP2	None

Table 6-9 The specific information of FI-HCNN using ICRM as input

FD Module	Output shape	Number of parameters
Input	[1x50x50]	
CONV1	[16x25x25]	3,616
BN1	[16x25x25]	32
CONV2	[16x13x13]	57,616
CONV3	[16x7x7]	57,616
GAP1, FC1	[16x4]	51
Total		118,931

SE Module	Output shape	Number of parameters
Input	[16x7x7]	
CONV4	[16x4x4]	6,416
CONV5	[16x2x2]	6,416
GAP2, FC2	[16x1]	17
Total		12,849

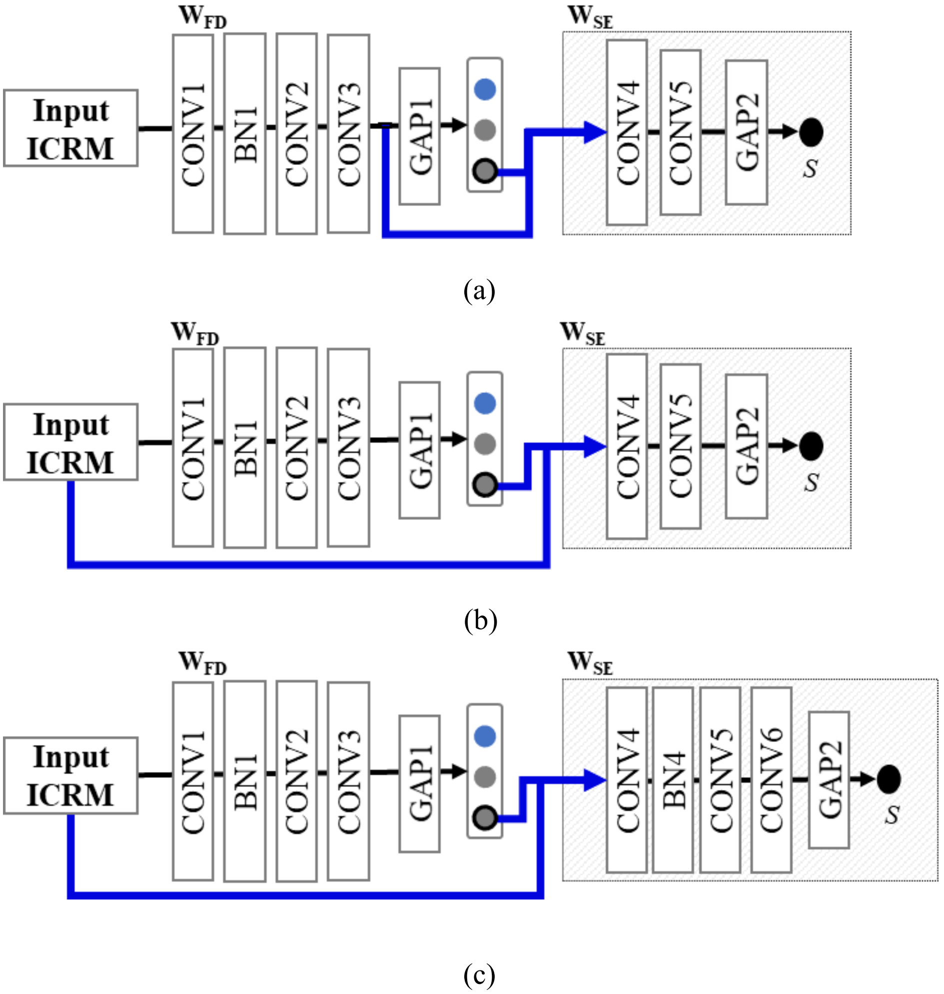

Figure 6-19 The structures of comparison in the HCNN models using ICRM as input under variable operating conditions: (a) FI-HCNN, (b) Rep-HCNN1, and (c) Rep-HCNN2

Table 6-10 Summary results of SE using FI-HCNN and other HCNN methods in variable operating condition

Methods	SE RMSE [%]	
	Stator inter-turn short	Misalignment
FI-HCNN (Proposed)	0.06±0.01	0.06±0.01
Rep-HCNN1	0.25±0.02	0.17±0.01
Rep-HCNN2	0.24±0.01	0.18±0.01

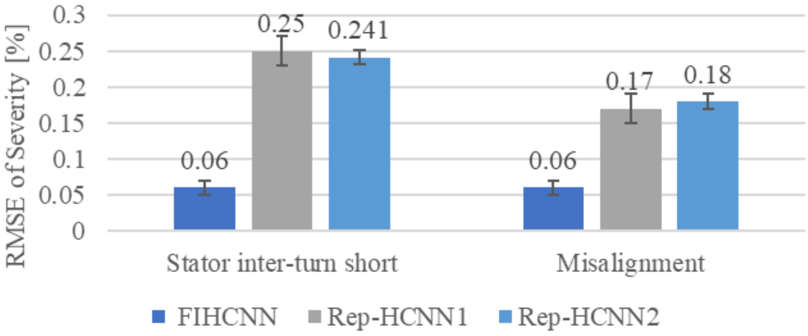

Figure 6-20 Bar chart comparing SE results using FI-HCNN and the conventional methods in variable operating conditions

To sum up, the proposed FI-HCNN was confirmed to enhance the estimation of fault severity by utilizing the latent features generated in the fault diagnosis module into the corresponding severity estimation module. Also, the proposed FI-HCNN method was validated under both stationary and variable operating conditions. In addition, multi-task learning that utilizes shared features to solve various tasks has been aroused recently, however, the setting of hyper-parameters for learning each task is a critical issue[109]–[112]. FI-HCNN has the merit of avoiding this parameter setting issue in that it can learn the FD and SE modules step by step in hierarchical order.

6.4 Summary and Discussion

In this study, a new method – FI-HCNN – was proposed to identify the faults of induction motors and to calculate the fault severity. The structure of FI-HCNN was hierarchically composed to lead to an FD module that can learn the types of faults and an SE module that is able to estimate their severity. Fault severity was more accurately estimated in the proposed method, as compared to conventional methods, because the latent features, which contain the representations of the fault modes, are propagated from the FD module to the SE module to support the learning of severity. First, the performance of HCNN was confirmed by comparison with conventional MCSA methods. Specifically, spectral features and PCs of FFT magnitude from stator current signals were used with SVM for FD and with SVR for SE. In addition, two conventional HCNN models whose structures are similar to that of FI-HCNN were examined to confirm the superiority of the feature inherited structure of the proposed method. Through the experimental studies, FI-HCNN was proven to provide enhanced features that are more suitable for accurate estimation of fault severity, without the need for significant domain knowledge. FI-HCNN has the potential to learn more robust features through extended training that is available from the pretrained weights when additional fault mode data is included. Then, the latent features that are generated from the more sophisticated FD module can be applied to improve the SE performance. FI-HCNN was confirmed to be applied with stator current signals under both stationary and various operating conditions; further, it showed better SE performance compared to other HCNN models. In future work, the training step can be enhanced by improving the loss function of FI-HCNN. Moreover, further study of FI-HCNN can be conducted in the presence of unknown faults.

Sections of this chapter have been published or submitted as the following journal articles:

1) **C. H. Park,** J. Lee, H. Kim, G. Ahn, M. Youn, and B. D. Youn, " Feature Inherited Hierarchical Convolutional Neural Network (FI-HCNN) for Motor Fault Severity Estimation Using Stator Current Signal," *International Journal of Precision Engineering and Manufacturing-Green Technology,* vol. 8, no. 4, pp. 1253-1266, 2021

Chapter 7

Conclusion

7.1 Contributions and Significance

In this dissertation, I proposed fault diagnosis methods for industrial motors under variable operating conditions using stator current signals. This research is composed of three parts: 1) Drive-tolerant current residual variance (DTCRV) which reduces the effect of operating conditions with minimal parameter settings for fault detection, 2) Instantaneous current residual map (ICRM) for physics-informed health image feature to identify the fault modes, 3) Feature-inherited hierarchical convolutional neural network (FI-HCNN) for deep learning-based fault severity estimation. The contribution and significance of the proposed research can be highlighted as follows.

First, the proposed method, called a drive-tolerant current residual variance (DTCRV), could detect a motor fault by reducing the effects of operating conditions embedded in stator current signals with minimal parameter settings. In the proposed method, the drive-related components are subtracted from the envelope of the stator current signal; thereby, the fault-induced oscillations are highlighted. Then, the variance of the current residual is determined as a representative. Although the conventional methods could detect a fault by investigating the particular parts of the stator current, the motor specific or diagnostic knowledge for determining the meaningful part is essential. However, the proposed DTCRV could be readily calculated with minimal parameter settings.

Second, the physics-informed health image feature, namely an instantaneous current residual map (ICRM), could identify the fault modes. Although the phase and amplitude modulations of stator current signals were revealed to have a physical relationship with the fault modes, there are few attempts to reflect the findings on the feature. Therefore, the current residuals which contain the fault-induced components of instantaneous amplitude and phase are calculated and construct the proposed ICRM by spread into a two-dimensional matrix. A type of fault can be determined by investigating the shape of spreading of the scaled current residual pairs in ICRM. A convolutional neural network (CNN) can be applied to learn the proposed ICRM for fault diagnosis, the investigation of the trained CNN model is also available with several visualization techniques including t-sne and CAM methods.

Third, the deep learning based fault severity estimation methods, called as a feature-inherited hierarchical CNN (FI-HCNN), was proposed. Through the special inherited structure between the hierarchy in FI-HCNN, the latent features which exploit the fault-related information in the fault diagnosis task could be re-utilized in the severity estimation tasks. Since the level-specific abstraction is supported by the latent features, FI-HCNN could improve the accuracy of the fault severity estimation.

In this dissertation, I proposed three different methods for monitoring the states of industrial motors under variable operating conditions. The DTCRV could detect a fault with minimal parameter settings. The ICRM could visualize the degree of deformation in instantaneous amplitude and phase that the effects of variable operating conditions are suppressed; thereby, the intuitive inspection of ICRM can infer the state of a motor. Moreover, the advanced fault diagnosis is available when a CNN model learns the shape of distribution in ICRM. Finally, the FI-HCNN could estimate the fault severity by utilizing the latent features in the upper fault diagnosis module. To sum up, the overall framework which cover from fault detection to severity estimation was developed for industrial motors under variable operating conditions using only stator current signals.

7.2 Suggestions for Future Research

This dissertation proposed three fault diagnosis methods for industrial motors under variable operating conditions. However, there are several remaining points which can be improved in future research.

- The proposed methods were validated with confined speed profiles and load torque levels. Although most of speed profiles in the industrial field consist of uniformly acceleration motion that controlled by a servo driver, we cannot certain that the highly non-linear speed profiles never occur in real-field. Also, the load torque can be time-varying in real-world situations. Therefore, the proposed methods are necessary to be improved to handle highly non-stationary conditions.

- The features which were proposed in the first and second research have a basis on the modulation behaviors of stator currents. However, the proposed methods are difficult to catch the genuine fault-induced modulations when the raw stator current signals are contaminated by the environmental noise in real-field. Therefore, the effective noise cancellation techniques for standing out the fault-induced modulations should be developed.

- In the third research, the proposed FI-HCNN method was validated with test-bed data sets of which all fault severity were manually determined. The severity was calculated in accordance with the official regulation if it exists; otherwise, the severity was determined proportional to the fault injection level for experiment. Since the real fault severity has a gap with the experimental value, the proposed method need to be validated under more various fault severity conditions.

- The proposed methods were mainly derived by the fault-related characteristics of stator current signals. In fact, the analysis of stator currents in the case of mechanical motor fault can be similarly extended to that in the mechanical faults of a rotating system. Therefore, the proposed methods in this dissertation could be applied to other fault modes including bearings and the fault of load components such as a gearbox, wheel, and belt.

- The proposed methods were mainly validated using the stator current signals acquired from the surface-mounted permanent magnet synchronous motor controlled by a servo drive. In this regard, the stator current signals can show different behaviors depending on the specification of servo drive, such as types of filters, control logic, and the setting value of parameters. Therefore, the proposed methods should be investigated its robustness with a variety of stator current signals acquired from different servo drives; and should be enhanced to take the variations into account if necessary.

- The proposed methods were mainly validated with the stator current signals acquired from a surface permanent mounted synchronous motor test-bed. However, there are numerous types of motors and operating conditions in practical applications. Moreover, the type of faults could be different. In fact, it is a significant challenge to make a method to cover lots of general environments. Recently, domain adaptation techniques in transfer learning have been arisen for applying a deep learning model to other new datasets. Therefore, the proposed methods that utilize a deep learning model could be improved by combining the methods with domain adaptation techniques.

Reference

[1] E. L. Bonaldi, L. E. de L. de Oliveira, J. G. B. da Silva, G. Lambert-Torresm, and L. E. B. da Silva, *Predictive maintenance by electrical signature analysis to induction motors*. IntechOpen, 2012.

[2] M. Ghaffari, J. Lee, L. Liao, F. Wu, D. Siegel, and W. Zhao, "Prognostics and health management design for rotary machinery systems—Reviews, methodology and applications," *Mechanical Systems and Signal Processing*, vol. 42, no. 1–2, pp. 314–334, 2013, doi: 10.1016/j.ymssp.2013.06.004.

[3] L. Wang, A. Y. C. Nee, A. Y. C. Nee, and L. Wang, *Collaborative design and planning for digital manufacturing*. Springer, 2009.

[4] Y. Liu and A. M. Bazzi, "A review and comparison of fault detection and diagnosis methods for squirrel-cage induction motors: State of the art," *ISA Transactions*, vol. 70, pp. 400–409, 2017, doi: 10.1016/j.isatra.2017.06.001.

[5] A. Bellini, F. Filippetti, C. Tassoni, and G. A. Capolino, "Advances in diagnostic techniques for induction machines," *IEEE Transactions on Industrial Electronics*, vol. 55, no. 12, pp. 4109–4126, 2008, doi: 10.1109/TIE.2008.2007527.

[6] M. Riera-Guasp, J. A. Antonino-Daviu, and G. A. Capolino, "Advances in electrical machine, power electronic, and drive condition monitoring and fault detection: State of the art," *IEEE Transactions on Industrial Electronics*, vol. 62, no. 3, pp. 1746–1759, 2015, doi: 10.1109/TIE.2014.2375853.

[7] S. bin Lee *et al.*, "Condition Monitoring of Industrial Electric Machines: State of the Art and Future Challenges," *IEEE Industrial Electronics Magazine*, vol. 14, no. 4, pp. 158–167, 2020, doi: 10.1109/MIE.2020.3016138.

[8] M. Y. Kaikaa, M. Hadjami, and A. Khezzar, “Effects of the Simultaneous Presence of Static Eccentricity and Broken Rotor Bars on the Stator Current of Induction Machine,” *IEEE Transactions on Industrial Electronics*, vol. 61, no. 6, pp. 2942–2942, 2014, doi: 10.1109/tie.2013.2288899.

[9] T. Goktas, M. Zafarani, and B. Akin, “Discernment of Broken Magnet and Static Eccentricity Faults in Permanent Magnet Synchronous Motors,” *IEEE Transactions on Energy Conversion*, vol. 31, no. 2, pp. 578–587, 2016, doi: 10.1109/TEC.2015.2512602.

[10] M. Ojaghi, M. Sabouri, and J. Faiz, “Analytic Model for Induction Motors Under Localized Bearing Faults,” *IEEE Transactions on Energy Conversion*, vol. 33, no. 2, pp. 617–626, 2018, doi: 10.1109/TEC.2017.2758382.

[11] B. Corne, B. Vervisch, S. Derammelaere, J. Knockaert, and J. Desmet, “The reflection of evolving bearing faults in the stator current’s extended park vector approach for induction machines,” *Mechanical Systems and Signal Processing*, vol. 107, no. 2018, pp. 168–182, 2018, doi: 10.1016/j.ymssp.2017.12.010.

[12] A. Picot, E. Fournier, J. Régnier, M. TientcheuYamdeu, J. M. Andréjak, and P. Maussion, “Statistic-Based Method to Monitor Belt Transmission Looseness Through Motor Phase Currents,” *IEEE Transactions on Industrial Informatics*, vol. 13, no. 3, pp. 1332–1340, 2017, doi: 10.1109/TII.2017.2661317.

[13] R. Sharifi and M. Ebrahimi, “Detection of stator winding faults in induction motors using three-phase current monitoring,” *ISA Transactions*, vol. 50, no. 1, pp. 14–20, 2011, doi: 10.1016/j.isatra.2010.10.008.

[14] B. M. Ebrahimi and J. Faiz, “Feature extraction for short-circuit fault detection in permanent-magnet synchronous motors using stator-current monitoring,” *IEEE Transactions on Power Electronics*, vol. 25, no. 10, pp. 2673–2682, 2010, doi:

10.1109/TPEL.2010.2050496.

[15] A. Bellini, F. Immovilli, R. Rubini, and C. Tassoni, “Diagnosis of Bearing Faults of Induction Machines by Vibration or Current Signals: A Critical Comparison,” *Industry Applications Society Annual Meeting, 2008. IAS ’08. IEEE*, vol. 46, no. 4, pp. 1–8, 2008.

[16] Y. Qi, E. Bostanci, M. Zafarani, and B. Akin, “Severity Estimation of Interturn Short Circuit Fault for PMSM,” *IEEE Transactions on Industrial Electronics*, vol. 66, no. 9, pp. 7260–7269, 2019, doi: 10.1109/TIE.2018.2879281.

[17] S. Moon, H. Jeong, H. Lee, and S. W. Kim, “Interturn short fault diagnosis in a PMSM by voltage and current residual analysis with the faulty winding model,” *IEEE Transactions on Energy Conversion*, vol. 33, no. 1, pp. 190–198, 2018, doi: 10.1109/TEC.2017.2726142.

[18] S. H. Kia, H. Henao, and G. A. Capolino, “Gear tooth surface damage fault detection using induction machine stator current space vector analysis,” *IEEE Transactions on Industrial Electronics*, vol. 62, no. 3, pp. 1866–1878, 2015, doi: 10.1109/TIE.2014.2360068.

[19] X. Chen and Z. Feng, “Induction motor stator current analysis for planetary gearbox fault diagnosis under time-varying speed conditions,” *Mechanical Systems and Signal Processing*, vol. 140, p. 106691, 2020, doi: 10.1016/j.ymssp.2020.106691.

[20] A. Gao, Z. Feng, and M. Liang, “Permanent magnet synchronous generator stator current AM-FM model and joint signature analysis for planetary gearbox fault diagnosis,” *Mechanical Systems and Signal Processing*, vol. 149, Feb. 2021, doi: 10.1016/j.ymssp.2020.107331.

[21] M. Blodt, P. Granjon, B. Raison, and G. Rostaing, “Models for bearing damage detection in induction motors using stator current monitoring,” *IEEE Transactions*

on Industrial Electronics, vol. 55, no. 4, pp. 1813–1822, 2008, doi: 10.1109/TIE.2008.917108.

[22] M. Blödt, M. Chabert, J. Regnier, and J. Faucher, “Mechanical load fault detection in induction motors by stator current time-frequency analysis,” *IEEE Transactions on Industry Applications*, vol. 42, no. 6, pp. 1454–1463, 2006, doi: 10.1109/TIA.2006.882631.

[23] B. M. Ebrahimi, M. Javan Roshtkhari, J. Faiz, and S. V. Khatami, “Advanced eccentricity fault recognition in permanent magnet synchronous motors using stator current signature analysis,” *IEEE Transactions on Industrial Electronics*, vol. 61, no. 4, pp. 2041–2052, 2014, doi: 10.1109/TIE.2013.2263777.

[24] T. Ameid, A. Menacer, H. Talhaoui, and Y. Azzoug, “Discrete wavelet transform and energy eigen value for rotor bars fault detection in variable speed field-oriented control of induction motor drive,” *ISA Transactions*, vol. 79, pp. 217–231, 2018, doi: 10.1016/j.isatra.2018.04.019.

[25] J. Faiz, V. Ghorbanian, and B. M. Ebrahimi, “EMD-Based analysis of industrial induction motors with broken rotor bars for identification of operating point at different supply modes,” *IEEE Transactions on Industrial Informatics*, vol. 10, no. 2, pp. 957–966, 2014, doi: 10.1109/TII.2013.2289941.

[26] Z. Li, T. Wang, Y. Wang, Y. Amirat, M. Benbouzid, and D. Diallo, “A Wavelet Threshold Denoising-Based Imbalance Fault Detection Method for Marine Current Turbines,” *IEEE Access*, vol. 8, pp. 29815–29825, 2020, doi: 10.1109/ACCESS.2020.2972935.

[27] A. Stief, J. R. Ottewill, J. Baranowski, and M. Orkisz, “A PCA and Two-Stage Bayesian Sensor Fusion Approach for Diagnosing Electrical and Mechanical Faults in Induction Motors,” *IEEE Transactions on Industrial Electronics*, vol. 66, no. 12,

pp. 9510–9520, 2019, doi: 10.1109/tie.2019.2891453.

[28] V. Choqueuse, M. E. H. Benbouzid, Y. Amirat, and S. Turri, “Diagnosis of three-phase electrical machines using multidimensional demodulation techniques,” *IEEE Transactions on Industrial Electronics*, vol. 59, no. 4, pp. 2014–2023, 2012, doi: 10.1109/TIE.2011.2160138.

[29] H. Razik, M. B. de Rossiter Corrêa, and E. R. C. da Silva, “A novel monitoring of load level and broken bar fault severity applied to squirrel-cage induction motors using a genetic algorithm,” *IEEE Transactions on Industrial Electronics*, vol. 56, no. 11, pp. 4615–4626, 2009, doi: 10.1109/TIE.2009.2029580.

[30] S. Das, P. Purkait, C. Koley, and S. Chakravorti, “Performance of a load-immune classifier for robust identification of minor faults in induction motor stator winding,” *IEEE Transactions on Dielectrics and Electrical Insulation*, vol. 21, no. 1, pp. 33–44, 2014, doi: 10.1109/TDEI.2013.003549.

[31] V. Climente-Alarcon, J. A. Antonino-Daviu, A. Haavisto, and A. Arkkio, “Diagnosis of Induction Motors Under Varying Speed Operation by Principal Slot Harmonic Tracking,” *IEEE Transactions on Industry Applications*, vol. 51, no. 5, pp. 3591–3599, 2015, doi: 10.1109/TIA.2015.2413963.

[32] J. C. Urresty, J. R. Riba, and L. Romeral, “Diagnosis of interturn faults in pmsms operating under nonstationary conditions by applying order tracking filtering,” *IEEE Transactions on Power Electronics*, vol. 28, no. 1, pp. 507–515, 2013, doi: 10.1109/TPEL.2012.2198077.

[33] J. Niu, S. Lu, Y. Liu, J. Zhao, and Q. Wang, “Intelligent Bearing Fault Diagnosis based on Tacholess Order Tracking for a Variable-Speed AC Electric Machine,” *IEEE Sensors Journal*, vol. 19, no. 5, pp. 1850–1861, 2018, doi: 10.1109/JSEN.2018.2883955.

[34] V. Climente-Alarcon *et al.*, "Transient tracking of low and high-order eccentricity-related components in induction motors via TFD tools," *Mechanical Systems and Signal Processing*, vol. 25, no. 2, pp. 667–679, 2011, doi: 10.1016/j.ymssp.2010.08.008.

[35] D. H. Kim *et al.*, "Smart Machining Process Using Machine Learning: A Review and Perspective on Machining Industry," *International Journal of Precision Engineering and Manufacturing - Green Technology*, vol. 5, no. 4, pp. 555–568, 2018, doi: 10.1007/s40684-018-0057-y.

[36] O. Abdeljaber, S. Sassi, O. Avci, S. Kiranyaz, A. A. Ibrahim, and M. Gabbouj, "Fault detection and severity identification of ball bearings by online condition monitoring," *IEEE Transactions on Industrial Electronics*, vol. 66, no. 10, pp. 8136–8147, 2019, doi: 10.1109/TIE.2018.2886789.

[37] B. Yang, Y. Lei, F. Jia, and S. Xing, "An intelligent fault diagnosis approach based on transfer learning from laboratory bearings to locomotive bearings," *Mechanical Systems and Signal Processing*, vol. 122, pp. 692–706, 2019, doi: 10.1016/j.ymssp.2018.12.051.

[38] G. Jiang, H. He, J. Yan, and P. Xie, "Multiscale Convolutional Neural Networks for Fault Diagnosis of Wind Turbine Gearbox," *IEEE Transactions on Industrial Electronics*, vol. 66, no. 4, pp. 3196–3207, 2019, doi: 10.1109/TIE.2018.2844805.

[39] V. Fernandez-Cavero, D. Morinigo-Sotelo, O. Duque-Perez, and J. Pons-Llinares, "A Comparison of Techniques for Fault Detection in Inverter-Fed Induction Motors in Transient Regime," *IEEE Access*, vol. 5, pp. 8048–8063, 2017, doi: 10.1109/ACCESS.2017.2702643.

[40] M. Blödt, D. Bonacci, J. Regnier, M. Chabert, and J. Faucher, "On-line monitoring of mechanical faults in variable-speed induction motor drives using the Wigner

distribution," *IEEE Transactions on Industrial Electronics*, vol. 55, no. 2, pp. 522–533, 2008, doi: 10.1109/TIE.2007.911941.

[41] M. Blödt, J. Regnier, and J. Faucher, "Distinguishing load torque oscillations and eccentricity faults in induction motors using stator current wigner distributions," *IEEE Transactions on Industry Applications*, vol. 45, no. 6, pp. 1991–2000, 2009, doi: 10.1109/TIA.2009.2031888.

[42] M. Riera-Guasp, J. A. Antonino-Daviu, M. Pineda-Sanchez, R. Puche-Panadero, and J. Perez-Cruz, "A general approach for the transient detection of slip-dependent fault components based on the discrete wavelet transform," *IEEE Transactions on Industrial Electronics*, vol. 55, no. 12, pp. 4167–4180, 2008, doi: 10.1109/TIE.2008.2004378.

[43] X. Y. Wang, V. Makis, and M. Yang, "A wavelet approach to fault diagnosis of a gearbox under varying load conditions," *Journal of Sound and Vibration*, vol. 329, no. 9, pp. 1570–1585, Apr. 2010, doi: 10.1016/j.jsv.2009.11.010.

[44] M. Heydarzadeh, M. Zafarani, M. Nourani, and B. Akin, "A Wavelet-Based Fault Diagnosis Approach for Permanent Magnet Synchronous Motors," *IEEE Transactions on Energy Conversion*, vol. 34, no. 2, pp. 761–772, 2019.

[45] M. M. Rahman and M. N. Uddin, "Online Unbalanced Rotor Fault Detection of an IM Drive Based on Both Time and Frequency Domain Analyses," *IEEE Transactions on Industry Applications*, vol. 53, no. 4, pp. 4087–4096, 2017, doi: 10.1109/TIA.2017.2691736.

[46] J. A. Rosero, L. Romeral, J. A. Ortega, and E. Rosero, "Short-circuit detection by means of empirical mode decomposition and Wigner-Ville distribution for PMSM running under dynamic condition," *IEEE Transactions on Industrial Electronics*, vol. 56, no. 11, pp. 4534–4547, 2009, doi: 10.1109/TIE.2008.2011580.

[47] A. Mejia-Barron, M. Valtierra-Rodriguez, D. Granados-Lieberman, J. C. Olivares-Galvan, and R. Escarela-Perez, “The application of EMD-based methods for diagnosis of winding faults in a transformer using transient and steady state currents,” *Measurement: Journal of the International Measurement Confederation*, vol. 117, no. August 2017, pp. 371–379, 2018, doi: 10.1016/j.measurement.2017.12.003.

[48] E. Elbouchikhi, V. Choqueuse, Y. Amirat, M. E. H. Benbouzid, and S. Turri, “An Efficient Hilbert-Huang Transform-Based Bearing Faults Detection in Induction Machines,” *IEEE Transactions on Energy Conversion*, vol. 32, no. 2, pp. 401–413, 2017, doi: 10.1109/TEC.2017.2661541.

[49] Z. Li, Q. Li, Z. Wu, J. Yu, and R. Zheng, “A Fault Diagnosis Method for on Load Tap Changer of Aerospace Power Grid Based on the Current Detection,” *IEEE Access*, vol. 6, pp. 24148–24156, 2018, doi: 10.1109/ACCESS.2018.2825219.

[50] Y. Lecun, Y. Bengio, and G. Hinton, “Deep learning,” *Nature*, vol. 521, no. 7553. Nature Publishing Group, pp. 436–444, May 27, 2015. doi: 10.1038/nature14539.

[51] O. Fink, Q. Wang, M. Svensén, P. Dersin, W. J. Lee, and M. Ducoffe, “Potential, challenges and future directions for deep learning in prognostics and health management applications,” *Engineering Applications of Artificial Intelligence*, vol. 92, Jun. 2020, doi: 10.1016/j.engappai.2020.103678.

[52] I. Goodfellow, Y. Bengio, and A. Courville, *Deep learning*. MIT press, 2016.

[53] J. Jiao, M. Zhao, J. Lin, and K. Liang, “A comprehensive review on convolutional neural network in machine fault diagnosis,” *Neurocomputing*, vol. 417, pp. 36–63, Dec. 2020, doi: 10.1016/j.neucom.2020.07.088.

[54] S. Tang, S. Yuan, and Y. Zhu, “Data Preprocessing Techniques in Convolutional Neural Network Based on Fault Diagnosis towards Rotating Machinery,” *IEEE Access*, vol. 8, pp. 149487–149496, 2020, doi: 10.1109/ACCESS.2020.3012182.

[55] G. Liu, L. Zhu, W. Yu, and W. Yu, “Image Formation, Deep Learning, and Physical Implication of Multiple Time-Series One-Dimensional Signals: Method and Application,” *IEEE Transactions on Industrial Informatics*, vol. 17, no. 7, pp. 4566–4574, Jul. 2021, doi: 10.1109/TII.2020.3018496.

[56] Z. Wang and T. Oates, “Imaging Time-Series to Improve Classification and Imputation.”

[57] Z. Wang and T. Oates, “Encoding Time Series as Images for Visual Inspection and Classification Using Tiled Convolutional Neural Networks,” 2015. [Online]. Available: www.aaai.org

[58] K. S. Kiangala and Z. Wang, “An Effective Predictive Maintenance Framework for Conveyor Motors Using Dual Time-Series Imaging and Convolutional Neural Network in an Industry 4.0 Environment,” *IEEE Access*, vol. 8, pp. 121033–121049, 2020, doi: 10.1109/ACCESS.2020.3006788.

[59] H. Tang, Z. Liao, P. Chen, D. Zuo, and S. Yi, “A Novel Convolutional Neural Network for Low-Speed Structural Fault Diagnosis under Different Operating Condition and Its Understanding via Visualization,” *IEEE Transactions on Instrumentation and Measurement*, vol. 70, 2021, doi: 10.1109/TIM.2020.3016752.

[60] R. Xiao, Z. Zhang, Y. Wu, P. Jiang, and J. Deng, “Multi-scale information fusion model for feature extraction of converter transformer vibration signal,” *Measurement: Journal of the International Measurement Confederation*, vol. 180, Aug. 2021, doi: 10.1016/j.measurement.2021.109555.

[61] Y. Bai, J. Yang, J. Wang, Y. Zhao, and Q. Li, “Image representation of vibration signals and its application in intelligent compound fault diagnosis in railway vehicle wheelset-axlebox assemblies,” *Mechanical Systems and Signal Processing*, vol. 152, May 2021, doi: 10.1016/j.ymssp.2020.107421.

[62] D. T. Hoang and H. J. Kang, “A Motor Current Signal-Based Bearing Fault Diagnosis Using Deep Learning and Information Fusion,” *IEEE Transactions on Instrumentation and Measurement*, vol. 69, no. 6, pp. 3325–3333, 2020, doi: 10.1109/TIM.2019.2933119.

[63] L. Wen, X. Li, L. Gao, and Y. Zhang, “A New Convolutional Neural Network-Based Data-Driven Fault Diagnosis Method,” *IEEE Transactions on Industrial Electronics*, vol. 65, no. 7, pp. 5990–5998, Jul. 2018, doi: 10.1109/TIE.2017.2774777.

[64] Z. X. Hu, Y. Wang, M. F. Ge, and J. Liu, “Data-Driven Fault Diagnosis Method Based on Compressed Sensing and Improved Multiscale Network,” *IEEE Transactions on Industrial Electronics*, vol. 67, no. 4, pp. 3216–3225, Apr. 2020, doi: 10.1109/TIE.2019.2912763.

[65] Z. Cui, W. Chen, and Y. Chen, “Multi-Scale Convolutional Neural Networks for Time Series Classification General Terms.”

[66] M. F. Guo, X. D. Zeng, D. Y. Chen, and N. C. Yang, “Deep-Learning-Based Earth Fault Detection Using Continuous Wavelet Transform and Convolutional Neural Network in Resonant Grounding Distribution Systems,” *IEEE Sensors Journal*, vol. 18, no. 3, pp. 1291–1300, Feb. 2018, doi: 10.1109/JSEN.2017.2776238.

[67] R. Chen, X. Huang, L. Yang, X. Xu, X. Zhang, and Y. Zhang, “Intelligent fault diagnosis method of planetary gearboxes based on convolution neural network and discrete wavelet transform,” *Computers in Industry*, vol. 106, pp. 48–59, Apr. 2019, doi: 10.1016/j.compind.2018.11.003.

[68] P. Liang, C. Deng, J. Wu, Z. Yang, J. Zhu, and Z. Zhang, “Compound Fault Diagnosis of Gearboxes via Multi-label Convolutional Neural Network and Wavelet Transform,” *Computers in Industry*, vol. 113, Dec. 2019, doi: 10.1016/j.compind.2019.103132.

[69] C. H. Park *et al.*, “Drive-tolerant Current Residual Variance (DTCRV) for Fault

Detection of a Permanent Magnet Synchronous Motor Under Operational Speed and Load Torque Conditions," *IEEE Access*, vol. Early Acce, pp. 1–15, 2021, doi: 10.1109/ACCESS.2021.3068425.

[70] C. H. Park, J. Lee, G. Ahn, M. Youn, and B. D. Youn, "Fault detection of PMSM under Non-stationary conditions based on wavelet transformation combined with distance approach," in *Proceedings of the 2019 IEEE 12th International Symposium on Diagnostics for Electrical Machines, Power Electronics and Drives, SDEMPED 2019*, 2019, pp. 88–93.

[71] J. H. Jung, B. C. Jeon, B. D. Youn, M. Kim, D. Kim, and Y. Kim, "Omnidirectional regeneration (ODR) of proximity sensor signals for robust diagnosis of journal bearing systems," *Mechanical Systems and Signal Processing*, vol. 90, pp. 189–207, 2017, doi: 10.1016/j.ymssp.2016.12.030.

[72] X. Zhu *et al.*, "Rotor fault diagnosis using a convolutional neural network with symmetrized dot pattern images," *Measurement: Journal of the International Measurement Confederation*, vol. 138, pp. 526–535, May 2019, doi: 10.1016/j.measurement.2019.02.022.

[73] S. K. Sul, *Control of electric machine drive systems*. [Piscataway, N.J.] : Hoboken, N.J. : John Wiley & Sons, 2011.

[74] Y. Yao, Y. Li, and Q. Yin, "A novel method based on self-sensing motor drive system for misalignment detection," *Mechanical Systems and Signal Processing*, vol. 116, pp. 217–229, 2019, doi: 10.1016/j.ymssp.2018.06.030.

[75] D. G. Dorrell, W. T. Thomson, and S. Roach, "Analysis of Airgap Flux, Current, and Vibration Signals as a Function of the Combination of Static and Dynamic Airgap Eccentricity in 3-Phase Induction Motors," *IEEE Transactions on Industry Applications*, vol. 33, no. 1, pp. 24–34, 1997, doi: 10.1109/28.567073.

[76] Y. Park, H. Choi, J. Shin, J. Park, S. bin Lee, and H. Jo, "Airgap flux based detection and classification of induction motor rotor and load defects during the starting transient," *IEEE Transactions on Industrial Electronics*, vol. 67, no. 12, pp. 10075–10084, 2020, doi: 10.1109/TIE.2019.2962470.

[77] T. A. Shifat and J. W. Hur, "An Effective Stator Fault Diagnosis Framework of BLDC Motor Based on Vibration and Current Signals," *IEEE Access*, vol. 8, pp. 106968–106981, 2020, doi: 10.1109/ACCESS.2020.3000856.

[78] L. Romeral, J. C. Urresty, J. R. Riba Ruiz, and A. Garcia Espinosa, "Modeling of surface-mounted permanent magnet synchronous motors with stator winding interturn faults," *IEEE Transactions on Industrial Electronics*, vol. 58, no. 5, pp. 1576–1585, 2011, doi: 10.1109/TIE.2010.2062480.

[79] S. T. Lee and J. Hur, "Detection technique for stator inter-turn faults in BLDC motors based on third-harmonic components of line currents," *IEEE Transactions on Industry Applications*, vol. 53, no. 1, pp. 143–150, 2017, doi: 10.1109/TIA.2016.2614633.

[80] W. T. Thomson and M. Fenger, "Current signature analysis to detect induction motor faults," *IEEE Industry Applications Magazine*, vol. 7, no. 4, pp. 26–34, 2001.

[81] "Condition monitoring and diagnostics of machine systems — Electrical signature analysis of three-phase induction motors, ISO 20958:2013," 2014

[82] T. Ince, S. Kiranyaz, L. Eren, M. Askar, and M. Gabbouj, "Real-Time Motor Fault Detection by 1-D Convolutional Neural Networks," *IEEE Transactions on Industrial Electronics*, vol. 63, no. 11, pp. 7067–7075, 2016, doi: 10.1109/TIE.2016.2582729.

[83] L. Eren, T. Ince, and S. Kiranyaz, "A Generic Intelligent Bearing Fault Diagnosis System Using Compact Adaptive 1D CNN Classifier," *Journal of Signal Processing Systems*, vol. 91, no. 2, pp. 179–189, 2019, doi: 10.1007/s11265-018-1378-3.

[84] F. ben Abid, M. Sallem, and A. Braham, “Robust Interpretable Deep Learning for Intelligent Fault Diagnosis of Induction Motors,” *IEEE Transactions on Instrumentation and Measurement*, vol. 9456, no. c, pp. 1–1, 2019, doi: 10.1109/tim.2019.2932162.

[85] J. Antonino-Daviu and P. Popaleny, “Detection of induction motor coupling unbalanced and misalignment via advanced transient current signature analysis,” *Proceedings - 2018 23rd International Conference on Electrical Machines, ICEM 2018*, pp. 2359–2364, 2018, doi: 10.1109/ICELMACH.2018.8506949.

[86] A. K. Verma, S. Sarangi, and M. H. Kolekar, “Experimental investigation of misalignment effects on rotor shaft vibration and on stator current signature,” *Journal of Failure Analysis and Prevention*, vol. 14, no. 2, pp. 125–138, 2014, doi: 10.1007/s11668-014-9785-7.

[87] J. L. Lin, J. Y. C. Liu, C. W. Li, L. F. Tsai, and H. Y. Chung, “Motor shaft misalignment detection using multiscale entropy with wavelet denoising,” *Expert Systems with Applications*, vol. 37, no. 10, pp. 7200–7204, 2010, doi: 10.1016/j.eswa.2010.04.009.

[88] M. E. H. Benbouzid, M. Vieira, and C. Theys, “Induction motors’ faults detection and localization using stator current advanced signal processing techniques,” *IEEE Transactions on Power Electronics*, vol. 14, no. 1, pp. 14–22, 1999, doi: 10.1109/63.737588.

[89] S. T. Lee and J. Hur, “Detection technique for stator inter-turn faults in BLDC motors based on third-harmonic components of line currents,” *IEEE Transactions on Industry Applications*, vol. 53, no. 1, pp. 143–150, 2017, doi: 10.1109/TIA.2016.2614633.

[90] S. Nandi, “Detection of stator faults in induction machines using residual saturation

harmonics," *IEEE Transactions on Industry Applications*, vol. 42, no. 5, pp. 1201–1208, 2006, doi: 10.1109/TIA.2006.880838.

[91] M. Azamfar, J. Singh, I. Bravo-Imaz, and J. Lee, "Multisensor data fusion for gearbox fault diagnosis using 2-D convolutional neural network and motor current signature analysis," *Mechanical Systems and Signal Processing*, vol. 144, p. 106861, 2020, doi: 10.1016/j.ymssp.2020.106861.

[92] M. Blödt, D. Bonacci, J. Regnier, M. Chabert, and J. Faucher, "On-line monitoring of mechanical faults in variable-speed induction motor drives using the Wigner distribution," *IEEE Transactions on Industrial Electronics*, vol. 55, no. 2, pp. 522–533, 2008, doi: 10.1109/TIE.2007.911941.

[93] B. Trajin, M. Chabert, J. Regnier, and J. Faucher, "Hilbert versus Concordia transform for three-phase machine stator current time-frequency monitoring," *Mechanical Systems and Signal Processing*, vol. 23, no. 8, pp. 2648–2657, 2009, doi: 10.1016/j.ymssp.2009.05.015.

[94] A. Sapena-Bano, J. Burriel-Valencia, M. Pineda-Sanchez, R. Puche-Panadero, and M. Riera-Guasp, "The Harmonic Order Tracking Analysis Method for the Fault Diagnosis in Induction Motors under Time-Varying Conditions," *IEEE Transactions on Energy Conversion*, vol. 32, no. 1, pp. 244–256, 2017, doi: 10.1109/TEC.2016.2626008.

[95] X. Chen and Z. Feng, "Time-frequency space vector modulus analysis of motor current for planetary gearbox fault diagnosis under variable speed conditions," *Mechanical Systems and Signal Processing*, vol. 121, pp. 636–654, 2019, doi: 10.1016/j.ymssp.2018.11.049.

[96] J. A. Rosero, L. Romeral, J. A. Ortega, and E. Rosero, "Short-circuit detection by means of empirical mode decomposition and Wigner-Ville distribution for PMSM

running under dynamic condition," *IEEE Transactions on Industrial Electronics*, vol. 56, no. 11, pp. 4534–4547, 2009, doi: 10.1109/TIE.2008.2011580.

[97] C. M. Bishop, *Pattern recognition and machine learning*. springer, 2006.

[98] B. C. Jeon, J. H. Jung, B. D. Youn, Y. W. Kim, and Y. C. Bae, "Datum unit optimization for robustness of a journal bearing diagnosis system," *International Journal of Precision Engineering and Manufacturing*, vol. 16, no. 11, pp. 2411–2425, 2015, doi: 10.1007/s12541-015-0311-y.

[99] X. Chen and Z. Feng, "Time-frequency space vector modulus analysis of motor current for planetary gearbox fault diagnosis under variable speed conditions," *Mechanical Systems and Signal Processing*, vol. 121, pp. 636–654, 2019, doi: 10.1016/j.ymssp.2018.11.049.

[100] Z. Feng, X. Chen, and M. J. Zuo, "Induction Motor Stator Current AM-FM Model and Demodulation Analysis for Planetary Gearbox Fault Diagnosis," *IEEE Transactions on Industrial Informatics*, vol. 15, no. 4, pp. 2386–2394, Apr. 2019, doi: 10.1109/TII.2018.2875447.

[101] K. He, X. Zhang, S. Ren, and J. Sun, "Identity Mappings in Deep Residual Networks," *European conference on computer vision*, pp. 630–645, Mar. 2016, [Online]. Available: http://arxiv.org/abs/1603.05027

[102] B. Akin, U. Orguner, H. A. Toliyat, and M. Rayner, "Phase-sensitive detection of motor fault signatures in the presence of noise," *IEEE Transactions on Industrial Electronics*, vol. 55, no. 6, pp. 2539–2550, 2008, doi: 10.1109/TIE.2008.921681.

[103] D. G. Dorrell, W. T. Thomson, and S. Roach, "Analysis of airgap flux, current, and vibration signals as a function of the combination of static and dynamic airgap eccentricity in 3-phase induction motors," *IEEE Transactions on Industry Applications*, vol. 33, no. 1, pp. 24–34, 1997, doi: 10.1109/28.567073.

[104] S. Nandi, H. A. Toliyat, and A. G. Parlos, “Performance analysis of a single phase induction motor under eccentric conditions,” *IEEE Transactions on Energy Conversion*, vol. 17, no. 3, pp. 174–181, 2002, doi: 10.1109/ias.1997.643024.

[105] N. M. Elkasabgy, A. R. Eastham, and G. E. Dawson, “Detection of broken bars in the cage rotor on an induction machine,” *IEEE Transactions on Industry Applications*, vol. 28, no. 1, pp. 165–171, 1992, doi: 10.1109/28.120226.

[106] M. Gan, C. Wang, and C. Zhu, “Construction of hierarchical diagnosis network based on deep learning and its application in the fault pattern recognition of rolling element bearings,” *Mechanical Systems and Signal Processing*, vol. 72–73, pp. 92–104, 2016, doi: 10.1016/j.ymssp.2015.11.014.

[107] X. Guo, L. Chen, and C. Shen, “Hierarchical adaptive deep convolution neural network and its application to bearing fault diagnosis,” *Measurement: Journal of the International Measurement Confederation*, vol. 93, pp. 490–502, 2016, doi: 10.1016/j.measurement.2016.07.054.

[108] D. Roy, P. Panda, and K. Roy, “Tree-CNN: A Hierarchical Deep Convolutional Neural Network for Incremental Learning,” *Neural Networks*, vol. 121, pp. 148–160, 2020, doi: 10.1016/j.neunet.2019.09.010.

[109] S. Guo, B. Zhang, T. Yang, D. Lyu, and W. Gao, “Multitask Convolutional Neural Network with Information Fusion for Bearing Fault Diagnosis and Localization,” *IEEE Transactions on Industrial Electronics*, vol. 67, no. 9, pp. 8005–8015, 2020, doi: 10.1109/TIE.2019.2942548.

[110] H. Li, W. Zhao, Y. Zhang, and E. Zio, “Remaining useful life prediction using multi-scale deep convolutional neural network,” *Applied Soft Computing Journal*, vol. 89, no. 1, pp. 87–96, 2020, doi: 10.1016/j.asoc.2020.106113.

[111] Z. Liu, H. Wang, J. Liu, Y. Qin, and D. Peng, “Multitask Learning Based on

Lightweight 1DCNN for Fault Diagnosis of Wheelset Bearings," *IEEE Transactions on Instrumentation and Measurement*, vol. 70, 2021, doi: 10.1109/TIM.2020.3017900.

[112] L. Wen, X. Li, and L. Gao, "A New Two-Level Hierarchical Diagnosis Network Based on Convolutional Neural Network," *IEEE Transactions on Instrumentation and Measurement*, vol. 69, no. 2, pp. 330–338, 2020, doi: 10.1109/TIM.2019.2896370.

국문 초록

가변운행조건 산업용 모터의 고장 진단을 위한 상전류 물리지식착안 딥러닝 연구

서울대학교 대학원
기계항공공학부
박 찬 희

모터는 산업용 로봇, 전기자동차, 펌프, 공기순환장치 등 산업 전반에 널리 사용된다. 사용 범위가 방대한 만큼 모터는 높은 신뢰도를 갖도록 생산되지만, 현장의 가혹한 환경과 사용 중 예기치 못한 요인들로부터 고장이 발생하면 짧은 작동 중지 시간 대비 막대한 경제적·사회적 손실을 유발한다. 따라서 모터의 고장 진단을 위한 연구들이 수행되어 왔고, 취득이 용이한 상전류 신호 분석을 바탕으로 한 연구가 보편적이다. 최근에는 모터의 운행 조건이 복잡해지면서, 다양한 운행 환경에서도 적용 가능한 고장 진단 방법 개발이 필수적이다. 하지만, 기존의 연구들은 1) 상당한 양의 파라미터 설정, 2) 고장 분류의 어려움, 3) 불균일한 심각도 추정이라는 난제가 있다. 본 논문에서는 위의 난제들을 극복하기 위한 세 가지 연구를 제안한다.

첫 번째 연구에서는 상전류신호에서 다양한 운행 속도와 부하의 영향을 줄임으로써 고장 민감도를 향상시킨 고장 감지 인자를 제안한다. 이때, 모터나 고장 관련 파라미터 및 진단학적 파라미터 설정을

최소화하였다. 또한, 전 과정이 시간도메인에서 계산되기 때문에 기존 기술 대비 빠른 속도로 낮은 신호취득 수준에서도 이상 감지가 가능함을 확인하였다. 두 번째 연구에서는 상전류 신호의 순시 진폭과 위상으로부터 고장연관 성분을 추출하여 2차원 행렬에 분포한 건전성 이미지를 제안한다. 가변 운행 환경 상전류신호의 순시 진폭과 위상에서는 각각 운행연관 성분과 고장연관 성분이 발현된다. 제안 방법은 순시진폭과 위상의 물리적 성질을 바탕으로 운행 연관 성분을 억제한 잔여 포락선과 잔여 위상을 켤레 형태로 추출한 다음, 2차원 행렬에 조정 배치함으로써 이미지형태의 건전성 인자를 도출한다. 제안 방법은 상전류 순시 진폭과 위상에서 고장 관련 정보를 함께 고려한 이미지 형태의 건전성 인자를 개발했다는 점에서 선구적 기여와 독창성을 가진다. 제안한 건전성 이미지는 정성적 분석을 통한 고장진단 뿐만 아니라, 딥러닝 모델의 입력으로 학습시켜 가변운행환경에서 정량적인 고장 분류 방법을 제시하는 데 활용된다. 세 번째 연구에서는 상전류 신호를 사용한 딥러닝기반 고장 심각도 추정 모델을 제안한다. 제안 방법은 위계형 딥러닝 모델에서 상위모듈에 고장 진단, 하위모듈에 심각도 추정 역할을 부여한 다음, 상위 모듈의 잠재특징 활용도를 하위모듈로 전이시켜 학습을 이어감으로써 잠재특징의 활용도를 높였다. 이는 심각도 추정 모듈이 특정 고장의 세부 특성을 학습하는데 집중하도록 유도한 것이다. 이를 통해 제안 방법의 심각도 추정 성능은 기존 기술 및 유사 위계형 딥러닝 모델 대비 향상될 수 있었다.

세 가지 연구를 종합하면 다양한 운행조건의 상전류 신호를 활용한 모터의 고장 진단 프레임워크 개발이라고 할 수 있으며, 각 연구들은 긴밀히 연결되어 있다. 첫 번째, 두 번째 연구의 제안방법은 고장 발현 시 변조되는 상전류의 물리적 특성에 근거하였는데, 첫번째 연구 산출물인 고장감지 인자가 주목하는 상전류의 진폭 변조는 두 번째 연구 산출물인 건전성 이미지의 잔여 포락선과 연결된다. 그리고, 두번째 연구 산출물인 건전성 이미지를 세번째 딥러닝 기반 심각도 추정 모델의 입력으로 활용하여 가변운행환경의 상전류신호에 대해서 심각도 추정을 수행할 수 있다. 또한, 본 논문에서 제안한 고장감지, 고장진단, 심각도 추정으로 연결되는 고장 진단 프레임워크는 상전류의 물리적 특성을 근거로 한 특질 인자와 딥러닝기반 고장진단 기술이 융합적으로 활용되기 때문에 물리지식에 착안한 딥러닝 연구라고 할 수 있다.

주요어: 고장 진단
산업용 모터
상전류 신호
다양한 운행 조건
신호 분석
딥러닝
건전성 예측진단 및 관리

학 번: 2016-20688